



**UNIVERSIDAD NACIONAL AUTÓNOMA DE MÉXICO**  
**FACULTAD DE INGENIERÍA**

**A geomechanical model for  
predicting the collapse of a  
carbonate formation**

**TESIS**

Que para obtener el título de  
**Ingeniero Petrolero**

**P R E S E N T A**

Ulises Sholl Avilés Hilario

**DIRECTOR DE TESIS**

Dr. Fernando Samaniego  
Verduzco



Ciudad Universitaria, Cd. Mx., 2025



**PROTESTA UNIVERSITARIA DE INTEGRIDAD Y  
HONESTIDAD ACADÉMICA Y PROFESIONAL  
(Titulación con trabajo escrito)**



De conformidad con lo dispuesto en los artículos 87, fracción V, del Estatuto General, 68, primer párrafo, del Reglamento General de Estudios Universitarios y 26, fracción I, y 35 del Reglamento General de Exámenes, me comprometo en todo tiempo a honrar a la institución y a cumplir con los principios establecidos en el Código de Ética de la Universidad Nacional Autónoma de México, especialmente con los de integridad y honestidad académica.

De acuerdo con lo anterior, manifiesto que el trabajo escrito titulado A GEOMECHANICAL MODEL FOR PREDICTING THE COLLAPSE OF A CARBONATE FORMATION que presenté para obtener el título de INGENIERO PETROLERO es original, de mi autoría y lo realicé con el rigor metodológico exigido por mi Entidad Académica, citando las fuentes de ideas, textos, imágenes, gráficos u otro tipo de obras empleadas para su desarrollo.

En consecuencia, acepto que la falta de cumplimiento de las disposiciones reglamentarias y normativas de la Universidad, en particular las ya referidas en el Código de Ética, llevará a la nulidad de los actos de carácter académico administrativo del proceso de titulación.

---

ULISES SHOLL AVILES HILARIO  
Número de cuenta: 316266053

## ***Dedicatoria***

*Esta tesis está dedicada a todas aquellas personas que confiaron plenamente en mí y me dieron su apoyo incondicional.*

*Con amor y gratitud para mis familiares y amigos.*

## **Agradecimientos**

A mis padres, **Guadalupe y Ulises**: por ser las primeras personas que creyeron y confiaron en mí, por darme amor y apoyo incondicional en cada etapa de mi vida. Gracias por enseñarme a soñar en grande y ser el pilar sobre el cual he construido mis aspiraciones. Su sacrificio, dedicación y confianza en mí son la esencia de este logro.

A **Einar y Miroslava**: por ser mis compañeros de vida y mis queridos hermanos. Gracias por todas las alegrías y momentos invaluable que hemos compartido juntos. Su constante apoyo y complicidad han sido un faro de luz en mi camino. Sin duda alguna, no podría haber deseado unos mejores hermanos que ustedes.

A **Rogelio y Victoria**: mis adorados abuelos, por siempre consentirme y creer en mí. Gracias por enseñarme el verdadero significado del amor entre un abuelo y su nieto. Su fortaleza y capacidad de superación han sido un ejemplo constante para mí. Su cariño y enseñanzas permanecerán conmigo para siempre.

A la familia **Hilario Ramírez**: por estar siempre conmigo en las buenas y en las malas, por desearme lo mejor y guiarme en cada etapa de mi vida. En especial, a **Elsa**, por ser como mi segunda madre. Gracias por enseñarme el valor del amor incondicional, por siempre escucharme, apoyarme y exigirme. Sin duda alguna, este logro lleva gran parte de ti y tu influencia.

A **Anahi**: por tu amor infinito y paciencia que me han acompañado durante este proceso. Gracias por tu apoyo constante y motivación que siempre me diste para seguir adelante con este trabajo.

A mis mejores amigos, **Jorge Mier y Jorge Torres**: por su amistad sincera, escucharme y apoyarme en los momentos de duda.

Al **Dr. Fernando Samaniego Verduzco**: por su tiempo y dedicación en este trabajo, así como por ser mi mentor, consejero y un gran ejemplo de dedicación y compromiso. Sus enseñanzas y orientación han sido cruciales para la realización de esta tesis.

A todos mis amigos y compañeros que conocí en la mejor etapa de mi carrera universitaria, el **Petrobowl**: con ustedes viví uno de los momentos más memorables de mi vida. Aprendí mucho de cada uno durante los últimos años y sus enseñanzas han dejado una huella imborrable en mi formación.

Por último, pero no menos importante, a mi alma mater, la **Universidad Nacional Autónoma de México**: por la educación y formación académica que me brindó. Gracias por ser el espacio donde pude crecer tanto personal como profesionalmente. La UNAM ha sido el cimiento sobre el cual he construido mi futuro.

# Abstract

Carbonate formations are a type of sedimentary rock primarily composed of carbonate minerals, such as calcite and dolomite. These formations are highly significant in the hydrocarbon industry as they frequently host substantial reservoirs of oil and gas. Beyond their economic importance, carbonate formations also play a crucial role in geology and ecology, forming structures like coral reefs and underground caves.

However, carbonate formations are prone to collapses and fractures due to their porous nature and overburden. The porosity and permeability of these rocks, along with factors such as chemical dissolution and recrystallization, can significantly influence their structural integrity. These collapses not only affect hydrocarbon production but also compromise well stability and operational safety.

Wellbore instability is one of the significant challenges in the drilling engineering and during the development of carbonate reservoirs, especially with open-hole completions during depletion can cause a reduction in permeability, damage to the equipment, solids production, and wellbore failure, interrupting production and affecting the reservoir's ultimate recovery.

Solids production from poorly consolidated carbonate reservoir rocks is a common factor in wells during production stages, especially in the reservoir's later life under depletion conditions. While there are several well-established techniques to predict sand production in sandstone reservoirs, there are not many field-proven case studies on the applicability of these techniques for solids production assessment in carbonate rocks (Asadi, 2017).

For this reason, advanced predictive methods are essential to describe the flow of fluids and solids from a friable formation into a producing well and anticipate the collapse of the rock near the well. A geomechanical model that combines geological and mechanical knowledge will be developed. This model will be based on a deep understanding of the geological history of carbonate formations, their internal structure, porosity, permeability, and the stresses acting upon them. The integration of field data, numerical simulations, and laboratory analyses will optimize hydrocarbon production and minimize the risks associated with the exploitation of carbonate formations. In this study, we present a case study on applying a sand evaluation model in a carbonate oil reservoir in Indiana, USA.

# Table of contents

<b>Abstract</b> .....	<b>4</b>
<b>1. Introduction</b> .....	<b>10</b>
1.1 Objectives.....	11
<b>2. Literature Review</b> .....	<b>12</b>
<b>2.1 Introduction to carbonate rocks</b> .....	<b>12</b>
<b>2.2 Fundamental Properties of Rock and Classification of Carbonate Rocks</b> .....	<b>12</b>
2.2.1 Texture .....	12
2.2.2 Fabric.....	13
2.2.3 Composition and Sedimentary Structures .....	13
2.2.4 Classification of Carbonate Rocks .....	13
<b>2.3 Petrophysical Properties of the Rock</b> .....	<b>14</b>
<b>2.3.1 Porosity</b> .....	<b>14</b>
2.3.1.1 Porosity Classifications.....	15
2.3.1.2 The Archie Classification .....	15
2.3.1.3 The Choquette-Pray Classification .....	16
2.3.1.4 The Lucia Classification.....	16
<b>2.3.2 Permeability</b> .....	<b>17</b>
<b>2.3.3 Pore Size</b> .....	<b>17</b>
<b>2.4 Introduction to Geomechanics</b> .....	<b>18</b>
<b>2.4.1 Stress</b> .....	<b>18</b>
<b>2.4.2 The stress tensor</b> .....	<b>19</b>
<b>2.4.3 Equations of Equilibrium</b> .....	<b>20</b>
<b>2.4.4 Strain</b> .....	<b>20</b>
2.4.4.1 Strain in one dimension .....	20
2.4.4.2 Strain in two dimensions.....	23
<b>2.4.5 Strain Tensor</b> .....	<b>24</b>
<b>2.4.6 Elastic Moduli</b> .....	<b>25</b>
<b>2.4.7 Constitutive Equation: Stress-Strain Relationship</b> .....	<b>27</b>
<b>2.4.8 Poroelasticity</b> .....	<b>29</b>
2.4.8.1 Suspension of Solid Particles in a Fluid .....	30
2.4.8.2 Effective stress .....	31

2.4.9 Mohr's Circles .....	32
2.4.10 The Mohr-Coulomb criterion .....	35
2.4.11 Cohesion .....	36
2.4.12 Local stresses .....	37
2.5 Solids Production.....	38
2.5.1 Well Completion and Solids Control .....	39
2.5.2 Solids Production in Limestone Reservoirs .....	39
2.5.3 Sand Control Method Applied in Carbonate Reservoirs .....	40
3. Hydromechanical Model.....	41
3.1 Mathematical Model .....	41
3.2 Law of Conservation of Mass .....	44
3.2.1 Relation of Mass with a Control Volume .....	44
3.2.2 Mass flow.....	45
3.2.3 Source and/or Sink Term.....	47
3.2.4 Integral Form of Mass Conservation .....	48
3.2.5 Differential Form of Mass Conservation.....	49
3.2.6 Material Balance Equation of the Phases.....	51
3.3 Constitutive Law of Mass Generation .....	54
3.4 Darcy's Law .....	56
3.5 Kozeny-Carman Equation .....	57
3.6 Continuity Equation .....	57
3.7 Borehole stresses, deformation and failure .....	58
4. Simulator Model.....	60
4.1 Introduction .....	60
4.2 Simulator Equations.....	61
4.2.1 Initial and Boundary Conditions.....	62
4.3 Finite Differences .....	63
4.3.1 Spatial Discretization .....	64
4.3.2 Temporal Discretization .....	65
4.4 Coupling of Boundary Conditions .....	66
4.5 Newton-Raphson Method .....	69
4.6 Coupling of Mechanical Deformation.....	72
4.7 Solution Algorithm .....	75

<b>4.8 Simulator Validation</b> .....	<b>75</b>
<b>4.9 Case Study Analysis</b> .....	<b>83</b>
4.9.1 Physical Analysis .....	84
4.9.2 Physical Effect of Permeability .....	85
4.9.3 Physical Effect of Cohesion .....	85
4.9.3 Physical Effect of Poisson's Ratio .....	86
4.9.4 Physical Effect of Internal Friction Angle .....	87
<b>5. Conclusions</b> .....	<b>88</b>
<b>Nomenclature</b> .....	<b>89</b>
<b>Appendix A</b> .....	<b>93</b>
<b>Formulation of Spatial Discretization</b> .....	<b>93</b>
<b>Appendix B</b> .....	<b>95</b>
<b>Formulation of Temporal Discretization</b> .....	<b>95</b>
B.1. Explicit Euler .....	95
B.2. Implicit Euler .....	96
<b>Appendix C</b> .....	<b>98</b>
<b>Jacobian Matrix</b> .....	<b>98</b>
<b>Appendix D</b> .....	<b>107</b>
<b>Geomechanical Boundary Conditions</b> .....	<b>107</b>
<b>Appendix E</b> .....	<b>108</b>
<b>Effective Well Stress Criterion Discretization</b> .....	<b>108</b>
<b>References</b> .....	<b>109</b>

# Table of figures

<b>Figure 2. 1</b> Dunham’s classification (Wayne, 2008).....	14
<b>Figure 2. 2</b> Choquette-Pray Porosity Classification (Wayne, 2008) .....	16
<b>Figure 2. 3</b> Decomposition of forces (Fjaer, 2008) .....	19
<b>Figure 2. 4</b> Plot of the relationship between displacement and distance (Téllez, 2021) ....	22
<b>Figure 2. 5</b> Shear deformation (Fjaer, 2008).....	22
<b>Figure 2. 6</b> Parameterization of shear deformation (Fjaer, 2008).....	24
<b>Figure 2. 7</b> Deformation induced by uniaxial stress (Fjaer, 2008) .....	26
<b>Figure 2.8</b> Stress Diagram of a Triaxial Tests (Zoback, 2007).....	32
<b>Figure 2. 9</b> Object Subject to Normal and Shear Stresses (Téllez, 2021).....	34
<b>Figure 2.10</b> Mohr's Circle in Two Dimensions.....	34
<b>Figure 2.11</b> Mohr-Coulomb Failure Criterion with fault curve with AL line. Failure will occur on this specific plane at an angle $\beta$ , marked by the CP line (Jaeger, 2007) .....	36
<b>Figure 2. 12</b> Local Stress System Around a Well (Pasic, 2007) .....	38
<b>Figure 3. 1</b> Phase Diagram of a Porous Medium Saturated with a Fluid and Movable Particles. (Vardoulakis, Stavropoulou, & Papanastasiou, 1996).....	42
<b>Figure 3. 2</b> Pore Channel with Movable Particles (Vardoulakis, Stavropoulou, & Papanastasiou, 1996).....	43
<b>Figure 3. 3</b> Vector Flow through a YZ Plane. (Téllez, 2021).....	47
<b>Figure 4. 1</b> Cylindrical Model of the Simulator .....	61
<b>Figure 4. 2</b> Spatially Discretized Mesh with Centered and Uniform Nodes.....	64
<b>Figure 4. 3</b> Simulator Configuration with Boundary Conditions.....	68
<b>Figure 4. 4:</b> a) Spatial Profile of Porosity at Various Times. b) Spatial Profile of Pressure at Various Times. (Stavropoulou, Papanastasiou, & Vardoulakis, 1998) .....	77
<b>Figure 4. 5 At Various Simulation Times:</b> a) Spatial Profile of Porosity b) Spatial Profile of Pressure. ....	77
<b>Figure 4. 6</b> a) Porosity Variation with Respect to Time at the Initial Node. b) Variation of Transport Concentration with Respect to Time at the First Node. (Stavropoulou, Papanastasiou, & Vardoulakis, 1998) .....	78
<b>Figure 4. 7</b> a) Variation of Porosity with Respect to Time at the First Node of the Simulator. b) Variation of Transport Concentration with Respect to Time at the First Node of the Simulator.....	78
<b>Figure 4. 8</b> a) Distribution of Radial Displacement Simulated at Various Times. b) Variation of Radial Displacement and Strain with Respect to Time, Evaluated at the Well Radius. (Stavropoulou, Papanastasiou, & Vardoulakis, 1998) .....	79
<b>Figure 4. 9</b> Distribution of Radial Displacement Simulated at Various Times.....	79
<b>Figure 4. 10</b> a) Temporal Variation of Radial Displacement at the Wellbore Wall Obtained by the Simulator. b) Temporal Variation of the Strain Derivative at the Wellbore Wall Obtained by the Simulator.....	80

<b>Figure 4. 11</b> Various Times Distribution of a) Radial Effective Stress. b) Tangential Effective Stress. (Stavropoulou, Papanastasiou, & Vardoulakis, 1998) .....	80
<b>Figure 4. 12</b> Various Time Distribution of a) Radial Effective Stress from the Simulator. b) Tangential Effective Stress obtained by the Simulator.....	81
<b>Figure 4. 13</b> Failure Envelopes and Critical Stresses Corresponding to the Inner Boundary $r = r_w$ , at Different Times ( $\theta = 37^\circ, C = 7.5 [Mpa]$ ) (Stavropoulou, Papanastasiou, & Vardoulakis, 1998) .....	81
<b>Figure 4. 14</b> a) Failure Envelopes and Critical Stresses Corresponding to the Inner Boundary $r = r_w$ , at Different Times ( $\theta = 37^\circ, C = 7.5 [Mpa]$ ) Obtained by the Simulator. b) Variation of the Failure Envelope and Stress Field at the Inner Boundary $r = r_w$ , at Different Times ( $\theta = 37^\circ, C = 7.5 [Mpa]$ ) Obtained by the Simulator. ....	82
<b>Figure 4. 15</b> Variation of Porosity with Respect to Time at the Initial Node. b) Variation of Transport Concentration at the Initial Node. c) Variation of the Failure Envelope and Stress Field at the Inner Boundary $r = r_w$ , at Different Times. ....	84
<b>Figure 4. 16</b> a) Variation of Porosity, Figure a), transport concentration, Figure b) and Failure Envelope and Stress Field at the Inner Boundary $r = r_w$ , Concerning Time at the Initial Node at Two Different Permeabilities. ....	85
<b>Figure 4. 17</b> Variation of the Failure Envelope and Stress Field at the Inner Boundary $r = r_w$ , at Different Times Obtained by the Simulator, at Two Different Cohesion Values. ....	86
<b>Figure 4. 18</b> Variation of the Failure Envelope and Stress Field at the Inner Boundary $r = r_w$ , at Different Times Obtained by the Simulator, at Two Different Poisson's Ratios. ....	86
<b>Figure 4. 19</b> Variation of the failure envelope and the stress field at the inner boundary $r = r_w$ , at different times obtained through the simulator at two different internal friction angles. ....	87
<b>Table 2. 1</b> Porosity in carbonate reservoirs (Wayne, 2008) .....	15
<b>Table 2. 2</b> Permeability in carbonate reservoirs (Wayne, 2008).....	17
<b>Table 4. 1</b> Input Data for the Simulator (Stavropoulou, Papanastasiou, & Vardoulakis, 1998).....	76
<b>Table 4. 2</b> Input Data for the Case Simulator .....	84

# 1. Introduction

Carbonates are naturally found as sediments and reefs in tropical and temperate oceans, as well as in ancient rock formations and economically significant mineral deposits. These deposits contain over 60% of conventional oil fields and 40% of global gas reserves. More than 90% of the oil in Mexico is extracted from these fields. (Francisco Garaicochea P., 1988)

In recent decades, geomechanics has gained significant importance in the oil industry, especially during well drilling operations, development, and exploitation stages. This discipline plays a fundamental role in petroleum engineering, of comprehensively understanding how rocks respond to forces and pressures in hydrocarbon reservoirs. This discipline is crucial in processes such as wellbore stability, completion designs, hydraulic fracturing, production optimization, pressure control, reserve estimation, and prevention of formation damage. Due to the complexity of the lithology, reservoir configuration, and genesis, wellbore instability is frequently encountered during drilling and extraction in carbonate reservoirs.

If the rock fails, the well will not produce it unless there is sufficient drag force to transport it to the surface through the production tubing. The pressure difference between the reservoir and the well is the main factor controlling solids production, as it determines the drag force necessary for the disintegrated rock to be transported to the well. Therefore, it is essential to understand the stresses, rock strength, and well and reservoir pressures to predict formation failure.

Wellbore instability is one of the significant challenges in drilling engineering and during the development of carbonate reservoirs, especially with open-hole completions during depletion; it can cause a reduction in permeability, damage to the equipment, solids production, and wellbore failure, interrupting production and affecting the reservoir's ultimate recovery. Therefore, it is essential to have a numerical tool to predict the conditions that may cause major solids production problems to prevent collapse.

Solids production from poorly consolidated carbonate reservoir rocks is a common factor in many wells during production stages, especially in the reservoir's later life under depletion conditions. While there are several well-established techniques to predict sand production in sandstone reservoirs, there are not many field-proven case studies on the applicability of these techniques for solids production assessment in carbonate rocks (Asadi, 2017). In this study, we present a case study on applying a sand evaluation model in a carbonate reservoir.

There are case studies in the literature where sand control and prediction methods are applied to carbonate formations due to the limited information available for the latter. In this work, the prediction method using a hydromechanical model for sands (Stavropoulou, Papanastasiou, & Vardoulakis, 1998) evaluating its reliability in carbonates formations.

## **1.1 Objectives**

- To integrate this tool into a carbonate formation and evaluate its reliability.
- To use this tool to explain solids production problems in various production scenarios.
- To develop a Time-Implicit numerical tool that allows predicting, according to different production schemes, the flow of solids in oil-producing formations and the collapse of the formation.
- To facilitate decision-making and reservoir management more efficiently and safely.
- To use porosity as a coupling parameter between erosion and rock mechanics.

## **2. Literature Review**

### **2.1 Introduction to carbonate rocks**

Carbonate reservoirs gained importance for the oil industry after World War I, when exploratory drilling led to one of the most significant discoveries of oil reserves in carbonates in the Middle East. As the demand for oil and gas increases, exploration and production efforts of these resources have been extended to ever greater depths. Carbonate reservoirs hold a crucial place in worldwide hydrocarbon resources with their highly developed fractures and microfractures, which enhance the storage capacity and percolation performance, while also posing exponentially more potential risks to extraction safety. (Bo Zhou, 2024)

Carbonates comprise at least 50% carbonate minerals, primarily calcite and dolomite. They form in depositional environments through biological, chemical, and detrital processes. Unlike other types of rocks, their mineralogical composition does not originate from erosion, and their textures are not the result of transport by streams and rivers. Carbonate minerals are susceptible to rapid processes of dissolution, cementation, and recrystallization.

### **2.2 Fundamental Properties of Rock and Classification of Carbonate Rocks**

Rocks, essential elements of the Earth's crust, possess fundamental properties that allow us to understand their formation, evolution, and behavior in different geological environments. Among these properties are fabric, texture, composition, and sedimentary structures, each providing crucial information about the history and conditions under which they formed.

#### **2.2.1 Texture**

Texture is defined as the size, shape, and arrangement of grains in a sedimentary rock; in the case of carbonates, is often considered in the context as of depositional texture, which forms the basis for various carbonate classification systems. The most common scale for classifying grain size is the Wentworth scale, measured in millimeters. According to this scale, a grain with a diameter greater than 2 mm is considered gravel; between 2 mm and 1/16 mm (62  $\mu\text{m}$ ), sand; and with a diameter less than 62  $\mu\text{m}$ , mud.

Grain sorting and size are important textural attributes for the study of carbonates, as they influence the rock's porosity and permeability. When the grains are ideal spheres, porosity is independent of grain size; however, permeability varies with particle size, as smaller grains have smaller intergranular pores and, consequently, narrower pore throats.

## **2.2.2 Fabric**

Fabric or structural characteristics refer to the spatial arrangement and orientation of grains in a sedimentary rock, which can be depositional, diagenetic, or biogenic. Carbonates are primarily formed by chemical precipitation, which occurs when calcium, magnesium, bicarbonate, and carbonate ions are present in an aqueous solution and combine to form solid carbonate minerals. This precipitation can result from the evaporation of water, changes in the water's temperature or pH, or biological activity.

Once formed, carbonate deposits can undergo diagenetic processes, including compaction and cementation of sediments to form sedimentary rocks. This process can occur in marine environments, such as coral reefs, lagoons, or continental shelves, where carbonates accumulate slowly over time.

Under certain conditions, carbonate rocks may experience metamorphism, which involves changes in their texture, composition, and structure due to elevated pressure and temperature. This process can lead to the formation of metamorphic rocks such as marbles, which are derived from preexisting these rocks.

## **2.2.3 Composition and Sedimentary Structures**

The composition of a carbonate generally refers to the types of grains that constitute it, rather than its mineral content. These grains are classified into skeletal and non-skeletal components. Skeletal components include whole and fragmented remains of calcareous plants and animals, such as mollusks, corals, calcified algae, brachiopods, arthropods, and echinoderms. On the other hand, non-skeletal grains comprise ooids, pisoids, peloids, and clasts.

Sedimentary structures are essential for interpreting depositional environments. Their internal fabric, which is often oriented and exhibits regular patterns of change in grain type, influences reservoir characteristics. These structures, visible in sedimentary rocks, reflect depositional and sedimentation processes such as stratification, grading, lamination, and deformation. Sedimentary structures provide valuable clues about depositional environments and variations in environmental conditions over geological time.

## **2.2.4 Classification of Carbonate Rocks**

The literature contains various classifications of limestones and dolomites based on different criteria. Limestones can be classified according to their mineral composition, textural components, and genetic origin. On the other hand, Dolomites can be classified according to their marine origin, types of textures present, depositional environments, geochemical characteristics, and the timing of dolomitization.

However, the most popular and commonly used classification is that of Dunham (1962), Fig 2.1. This classification includes detrital carbonates ranging from mudstone to grainstone, biogenic carbonates such as boundstone, and diagenetically altered carbonates, known as crystalline carbonates. There are also classifications based on porosity, but these do not consider the origin of the rock, making it difficult to distinguish between pore types formed by depositional processes and those modified or created by post-depositional diagenesis or fracturing.

Depositional Texture Recognizable					Original components were bound together during deposition, as shown by intergrown skeletal matter, lamination contrary to gravity, or sediment-floored cavities that are roofed over by organic or questionably organic matter and are too large to be interslices.	Depositional Texture Not Recognizable (Subdivide according to classifications designed to bear on physical texture or diagenesis.)
Original Components Not Bound Together During Deposition				Grain-supported		
Contains mud (particles of clay and fine silt size, less than 20 microns)		Grain-supported			Less than * 10 percent mud	
Mud-supported		Grain-supported				
Less than 10 percent grains	More than 10 percent grains	More than * 10 percent mud	Less than * 10 percent mud			
<b>Mudstone</b>	<b>Wackestone</b>	<b>Packstone</b>	<b>Grainstone</b>	<b>Boundstone</b>	<b>Crystalline Carbonate</b>	

Figure 2. 1 Dunham's classification (Wayne, 2008)

## 2.3 Petrophysical Properties of the Rock

Essential properties such as texture, mineralogy, composition, and structure determine porosity, permeability, and grain density. Porosity and permeability are crucial variables for evaluating the quality of a reservoir. Comprehensive reservoir descriptions are based on the identification and analysis of the relationship between the matrix and pore characteristics.

### 2.3.1 Porosity

Porosity is defined as the ratio between the pore volume ( $V_p$ ) and the total volume of the rock ( $V_b$ ). This property varies according to the texture, structure, and geometry of the fractures in the reservoir rock. In detrital rocks, grain shape, sorting, and packing influence porosity. In biogenic rocks, skeletal structure and microstructure affect both inter- and intra-particle porosity. In the case of fractured rocks, porosity depends on the width and spacing of the fractures, as well as the presence or absence of minerals. Additionally, diagenetic processes can modify porosity: they can fill pores with cement, close pores through compaction, open them through dissolution, or create new pores through recrystallization or replacement.

Carbonates are characterized by having multiple porosity, unlike sands. This porosity ranges from primary, which forms at the time of deposition, to secondary, which results from diagenetic processes. This diversity is due to the variety of sizes, shapes, and origins of pores in carbonates.

Porosity in carbonate reservoirs ranges from 5% to 15%, while in sands it ranges from 15% to 30%. Table 2.1 presents a qualitative description of the reservoir based on its porosity percentage.

Porosity range	Qualitative Description
5% or less	Poor
10%	Fair
15%	Good
20% or more	Excellent

**Table 2. 1** Porosity in carbonate reservoirs (*Wayne, 2008*)

Porosity measurements should be conducted under in situ stress conditions, as carbonates are compressible, and their porosity decreases with increased effective stress. The most common laboratory method involves increasing the confining pressure while maintaining a constant pore pressure.

### 2.3.1.1 Porosity Classifications

Classifications are useful tools for organizing materials effectively. A simple classification of porosity can designate three categories of pores: inter-particle, vuggy, and fracture porosity. On the other hand, a tiered classification group pores according to their average size, shape, petrophysical characteristics, and origin.

The comparison of data on pores and rock with petrophysical characteristics allows for the identification and mapping of reservoir flow units. Although traditional classifications of carbonate porosity were not designed for this purpose, the schemes proposed by Archie (1952), Choquette and Pray (1970), and Lucia (1983) are valuable for illustrating the evolution of pore systems in carbonate reservoirs.

### 2.3.1.2 The Archie Classification

Archie's classification (1952) is based on textural descriptions of reservoir rocks and consists of three textural categories: Type I, II, and III.

- Type I: Described carbonates as crystalline, hard, dense, with sharp edges and smooth faces on breaking.
- Type II: These are described as “earthy” or “chalky” with grains not more significant than about 50 μm in diameter, and they are composed of fine granules or sea organisms.
- Type III: Includes granular carbonates as grainstones and packstones.

Archie's goal in developing this classification was to highlight pore structure, fluid flow characteristics, fluid distribution, and the flow's electrical conductivity. He avoided using terms related to rock composition or the geological origin of the porosity.

### **2.3.1.3 The Choquette-Pray Classification**

Choquette and Pray (1970) recognized the need to incorporate the factor of time and mode of origin in their classification. Their system, represented in Fig 2.2, is practical and the authors identify 15 basic types of pores, organizing them into three classes according to their relationship with the rock fabric:

1. Fabric-selective pores: These pores can have a depositional, diagenetic, or a combination of both origins.
2. Non-fabric-selective pores include fractures or dissolution cavities of diverse sizes that cut across the entire rock.
3. Pores that may or may not be fabric-selective: This category encompasses pores with intermediate characteristics between the two previous types.

Choquette and Pray's classification is valuable for its focus on the origin and temporal development of pores, which allows for a more detailed understanding of reservoirs' petrophysical and structural characteristics.

The abundance of pores in the Choquette-Pray classification is given as a percentage, expressed as a ratio of pore categories, or as a ratio of pore types plus a percentage. The pore size categories are termed 'megapore, mesopore, and micropore,' with size limits like those of the Wentworth grain size scale (1922).

**Figure 2. 2** Choquette-Pray Porosity Classification (*Wayne, 2008*)

### **2.3.1.4 The Lucia Classification**

Lucia divides the types of carbonate pores into vuggy and interparticle. The author emphasizes a relationship between porosity, permeability, displacement capillary pressure, as particle size and the petrophysical importance of separating or touching vugs. Vugs are pores larger than the grains of the structure; they can have moldic, interparticle, intraparticle, or intercrystalline origins but were enlarged by dissolution to become vugs. The flow between separate vugs must pass through the matrix porosity and permeability to drain the vugs. For this reason, the contribution of separate vugs to the total porosity and permeability of the reservoir can only be estimated if the matrix characteristics and total porosity are known. Additionally, there is a possibility that they communicate through fractures that connect the vugs, thereby increasing their porosity and permeability.

### 2.3.2 Permeability

Permeability is essential because it is a property of the rock that relates to the rate at which hydrocarbons can be recovered. In carbonates, permeability varies, with values ranging from 0.1 md in tight and mudstone-type reservoirs to as high as 20 Darcies in reservoirs with connected fracture or vug systems. **Table 2.2** provides a way to qualitatively categorize permeability values.

Permeability (md)	Qualitative Description
<1.0-15	Poor to fair
15-50	Moderate
50-250	Good
250-1,000	Very Good
>1,000	Excellent

**Table 2. 2** Permeability in carbonate reservoirs (*Wayne, 2008*)

Geoscientific studies indicate that 80% of common sedimentary rocks have permeabilities in the range of  $1.0-10^{-3}$  md, 13% are in the range of  $10^{-3}-1.0$  md, 5% in the range of 1.0-1,000 md, and only 2% have permeabilities greater than 1,000 md. Permeability can be divided into absolute, effective, and relative, depending on the amount of fluids present in the porous medium. Permeability, like porosity, is sensitive to variations in the texture and fabric of reservoir rocks. Unlike porosity, permeability varies with grain size, packing, sorting, and fabric.

### 2.3.3 Pore Size

Pore size is the common factor between permeability and hydrocarbon saturation. Different permeability models have described the pore space of the radii of a series of capillary tubes. The number of capillary tubes is equal to the porosity, so permeability is a function of porosity and the square of the pore radius. Kozeny (1927) replaced the surface area of the pore space with the pore radius and developed the well-known Kozeny equation, which relates permeability to porosity, surface area, and the Kozeny constant.

However, these equations demonstrate that pore size and pore size distribution are important. In carbonates. There is no relationship between porosity and permeability unless pore size is included.

## 2.4 Introduction to Geomechanics

Geomechanics role in petroleum engineering, providing a comprehensive understanding of how rocks respond to forces and pressures in hydrocarbon reservoirs. This discipline is crucial in processes such as wellbore stability, completion designs, hydraulic fracturing, production optimization, pressure control, reserve estimation, and formation damage prevention.

Most materials possess the ability to resist and recover from deformations induced by various external forces, a property known as elasticity. When the changes in external forces are small, the deformation response is usually linear, which gives rise to the theory of elasticity. This theory is based on two main concepts: stress and strain. The key components in a Geomechanical model include the stress system and the deformations caused by this system.

Since the decline in production causes changes in formation stresses, it is necessary to determine the magnitude of this alteration throughout the reservoir's life and manage it optimally. In the initial stages, solids production can be managed without significantly affecting production, but in the long term, well collapse could occur. This chapter will address the terms necessary to develop a Geomechanical model in a well and derive the equations that will model the behavior when solids production occurs.

### 2.4.1 Stress

A stress is defined as the force acting perpendicularly on a certain area. In the International System of Units, the units for stress are  $Pa$  (Pascals =  $N/m^2$ ), but in the oil industry, the  $psi$  units are used. Compared to the concept of pressure, stress is a tensor that describes the density of forces acting on all surfaces of a body through a given point. The mathematical form to represent it is as follows:

$$\sigma_{ij} = \frac{F_i}{A_j}, \quad (2.4.1)$$

where  $\sigma_{ij}$  will be the force acting in the  $i$  direction on an area oriented perpendicularly to the  $j$  direction. It is important to note that although the forces applied to an object are equal, the stresses will vary depending on the cross-sectional area; where the area ( $A$ ) is smaller, the stress ( $\sigma$ ) will be greater.

It is also important to mention that when the force is not applied in the direction of the normal to the surface, the force must be decomposed ( $F$ ) into a normal force ( $F_n$ ) and a parallel force ( $F_p$ ) to the surface, as shown in Fig 2.3, and thus two new equations are obtained:

$$\sigma = \frac{F_n}{A}, \quad (2.4.2)$$

$$\tau = \frac{F_p}{A}. \quad (2.4.3)$$

where  $\sigma$  will be called normal stress and  $\tau$  the shear stress.

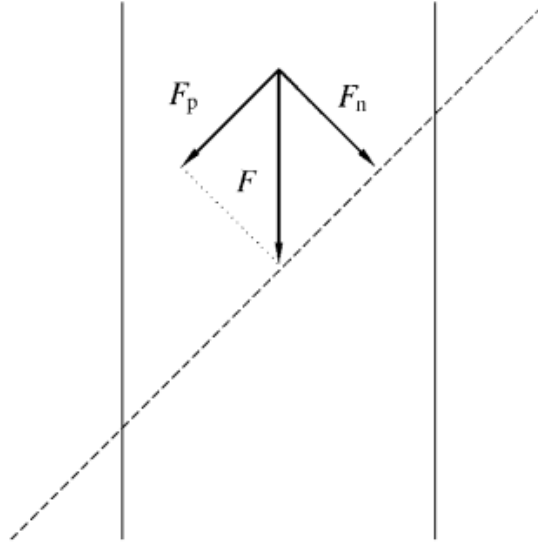


**Figure 2. 3** Decomposition of forces (Fjaer, 2008)

## 2.4.2 The stress tensor

Stresses related to a normal surface in the  $x$ -axis are denoted as  $\sigma_x$ ,  $\tau_{xy}$  y  $\tau_{xz}$ , which represent the normal stress, the shear stress related to a force in the direction of the  $y$ -axis, and the shear stress related to a force in the direction of the  $z$ -axis, respectively. Similarly, with stresses related to a normal surface in the  $y$ -axis,  $\sigma_y$ ,  $\tau_{yx}$  y  $\tau_{yz}$  and the stresses related to a normal surface in the  $z$ -axis are denoted as  $\sigma_z$ ,  $\tau_{zx}$  y  $\tau_{zy}$ . These nine components generate the stress tensor:

$$\bar{\sigma} = \begin{pmatrix} \sigma_x & \tau_{xy} & \tau_{xz} \\ \tau_{yx} & \sigma_y & \tau_{yz} \\ \tau_{zx} & \tau_{zy} & \sigma_z \end{pmatrix}. \quad (2.4.4)$$

However, the notation used in the Eq. 2.4.4 is not very convenient for theoretical calculations. In Eq. 2.4.5, the subscripts  $i$  and  $j$  were changed to numbers 1, 2, and 3, which represent the  $x$ ,  $y$ , and  $z$  axes, respectively. The first subscript  $i$  identifies the direction in which the stress tensor acts, while the second subscript  $j$ , represents a direction perpendicular to the plane. where  $\sigma_{11} = \sigma_x$ ,  $\sigma_{23} = \tau_{yz}$ , etc.

$$\bar{\sigma} = \begin{pmatrix} \sigma_{11} & \sigma_{12} & \sigma_{13} \\ \sigma_{12} & \sigma_{22} & \sigma_{23} \\ \sigma_{13} & \sigma_{23} & \sigma_{33} \end{pmatrix}. \quad (2.4.5)$$

### 2.4.3 Equations of Equilibrium

In addition to the forces acting on a body's surface, called contact forces, there are other forces acting on every part of the body, known as body forces. In geomechanics, the contact forces are the shear and normal stresses, or the stress tensor represented in Eq. 2.4.5. Body forces are produced by a force field around the body and depend on size and distance; an example of this is gravity.

Body forces generate stress gradients. For example, an element in a formation is not only subject to the force of gravity but also bears the weight of the formation above it. Therefore, the total stress increases with depth. According to Fjaer (2008), the components of the body force per unit mass acting at a point  $x$ ,  $y$ , and  $z$  of a body are denoted as  $f_x$ ,  $f_y$  and  $f_z$ . To continue with the stress tensor notation, the subscripts will be changed  $x$ ,  $y$ , and  $z$  for  $1$ ,  $2$ , and  $3$ .

To establish a balance of forces acting on a body, Newton's Second Law is used, which states that the sum of all forces acting on a body must produce a resultant force equal to the mass of the object multiplied by the acceleration the body experiences. In geomechanics, the accelerations are so small that they are set to zero. The equilibrium equations in three dimensions that describe this balance of forces are as follows:

$$\frac{\partial \sigma_{11}}{\partial x_1} + \frac{\partial \sigma_{12}}{\partial x_2} + \frac{\partial \sigma_{13}}{\partial x_3} + \rho f_1 = 0, \quad (2.4.6)$$

$$\frac{\partial \sigma_{21}}{\partial x_1} + \frac{\partial \sigma_{22}}{\partial x_2} + \frac{\partial \sigma_{23}}{\partial x_3} + \rho f_2 = 0, \quad (2.4.7)$$

$$\frac{\partial \sigma_{31}}{\partial x_1} + \frac{\partial \sigma_{32}}{\partial x_2} + \frac{\partial \sigma_{33}}{\partial x_3} + \rho f_3 = 0. \quad (2.4.8)$$

### 2.4.4 Strain

Strain is defined as deformation due to stress (Wayne, 2008). The deformation of a body will result in a change in length per unit of original length. Like stresses, there are two types of deformations that a structure experiences: normal deformation and shear deformation. The goal of solving this problem in geomechanics is to calculate the displacement at any point in the rock based on the knowledge of the forces applied to the rock body. (Télez, 2021)

#### 2.4.4.1 Strain in one dimension

Considering a cylindrical body in a state of uniaxial tension, where a normal stress is acting ( $\sigma_x$ ), the body undergoes elongation. For geomechanics, it is necessary to establish a relationship between the deformation ( $\epsilon$ ) and the displacement ( $u_x$ ) caused by the presence of stress on the cylinder. If a linear relationship between displacement and deformation

distance is assumed, as shown in **Fig. 2.4**, the slope would be the deformation ( $\epsilon$ ) and the following equation is obtained:

$$u_1 = \epsilon (x_1 - x_0) + u_0. \quad (2.4.9)$$

If we consider that  $h = x_1 - x_0$ , then Eq. 2.4.9 becomes:

$$u_1 = \epsilon h + u_0. \quad (2.4.10)$$

If the displacement is expressed as a function of the distances traveled, Eq. 2.4.10 changes to:

$$u(x_0 + h) = \epsilon h + u(x_0). \quad (2.4.11)$$

Solving the deformation ( $\epsilon$ ):

$$\epsilon = \frac{u(x_0+h) - u(x_0)}{h}. \quad (2.4.12)$$

Considering the limit of  $h$  approaches zero, Eq. 2.4.12 transforms to:

$$\epsilon = \frac{\partial u}{\partial x}. \quad (2.4.13)$$

This last equation represents the relationship between the displacement between two points and the original length. This type of deformation is normal since a normal stress act on the plane perpendicular to the x-direction. It is important to mention that Eq. 2.4.13 is valid only when there is a compressive stress; in the case of a tensile stress, it would change to a negative sign.

As mentioned earlier, there is another type of deformation that can be expressed as the change in the angle  $\psi$  between two directions that were initially orthogonal, as shown in Fig. 2.5. This is shear deformation and is mathematically defined as follows:

$$\gamma = \frac{1}{2} \tan \psi. \quad (2.4.14)$$

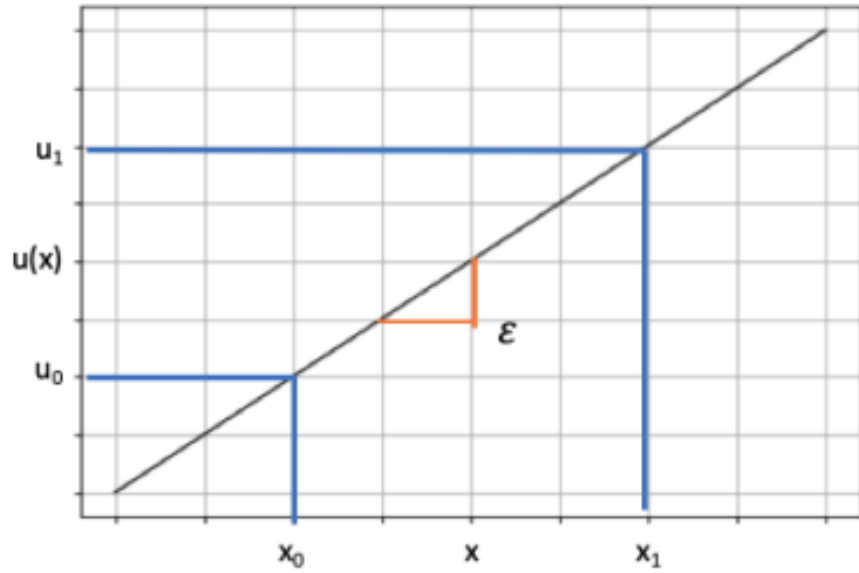


**Figure 2. 4** Plot of the relationship between displacement and distance (*Téllez, 2021*)

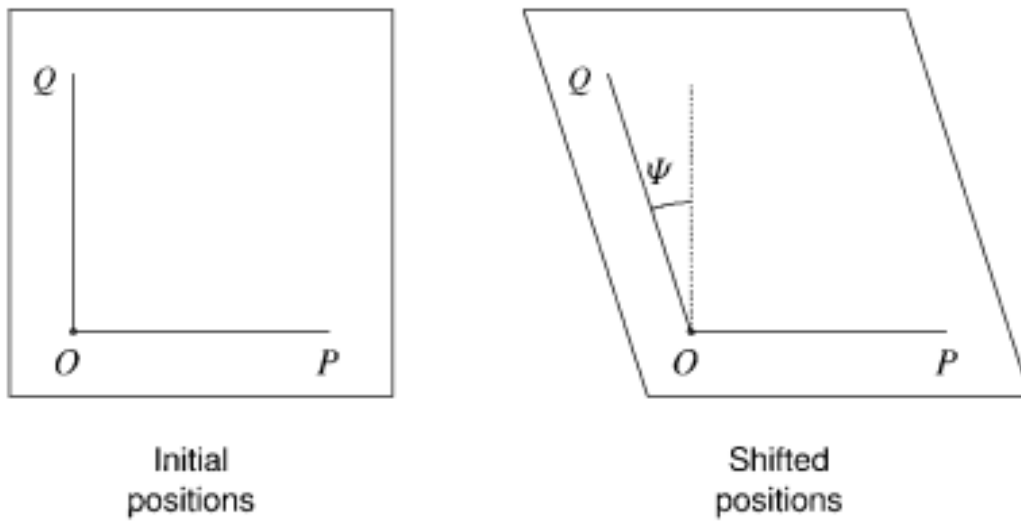


**Figure 2. 5** Shear deformation (*Fjaer, 2008*)

### 2.4.4.2 Strain in two dimensions

For many applications, only infinitesimal deformations are considered, which implies that both normal and shear deformations are so small that their products and squares can be ignored. Considering deformations in two dimensions as shown in Fig. 2.6 and assuming these are small, the corresponding shear deformation in the  $x$ -direction is found to be the following:

$$\gamma_{xy} = \frac{1}{2} \tan \psi \approx \frac{1}{2} \sin \psi = -\frac{1}{2} \cos \left( \frac{\pi}{2} + \psi \right) = -\frac{1}{2} \frac{\vec{P}'_1 \cdot \vec{P}'_2}{|\vec{P}'_1| \cdot |\vec{P}'_2|} \quad (2.4.15)$$

The vectors  $\vec{P}_1, \vec{P}'_1, \vec{P}_2$  y  $\vec{P}'_2$  are found in **Fig. 2.6**. When  $\Delta x \rightarrow 0$ ,  $\Delta y \rightarrow 0$ , and squares and products of the strains are neglected, we find that:

$$\gamma_{xy} = \frac{1}{2} \left( \frac{\partial u}{\partial y} + \frac{\partial v}{\partial x} \right). \quad (2.4.16)$$

To give a better description of the state of deformations at a point in a three-dimensional body, the elongations and shear deformations corresponding to the 3 axes are defined as follows:

$$\varepsilon_x = \frac{\partial u}{\partial x}, \quad (2.4.17)$$

$$\varepsilon_y = \frac{\partial v}{\partial y}, \quad (2.4.18)$$

$$\varepsilon_z = \frac{\partial w}{\partial z}, \quad (2.4.19)$$

$$\gamma_{xy} = \gamma_{yx} = \frac{1}{2} \left( \frac{\partial u}{\partial y} + \frac{\partial v}{\partial x} \right), \quad (2.4.20)$$

$$\gamma_{xz} = \gamma_{zx} = \frac{1}{2} \left( \frac{\partial u}{\partial z} + \frac{\partial w}{\partial x} \right), \quad (2.4.21)$$

$$\gamma_{yz} = \gamma_{zy} = \frac{1}{2} \left( \frac{\partial v}{\partial z} + \frac{\partial w}{\partial y} \right). \quad (2.4.22)$$

In **Fig. 2.6**, the notations used are  $u, v$  and  $w$ , using the equivalences, it is assumed that  $u=U_x, v=U_y, w=U_z$ .

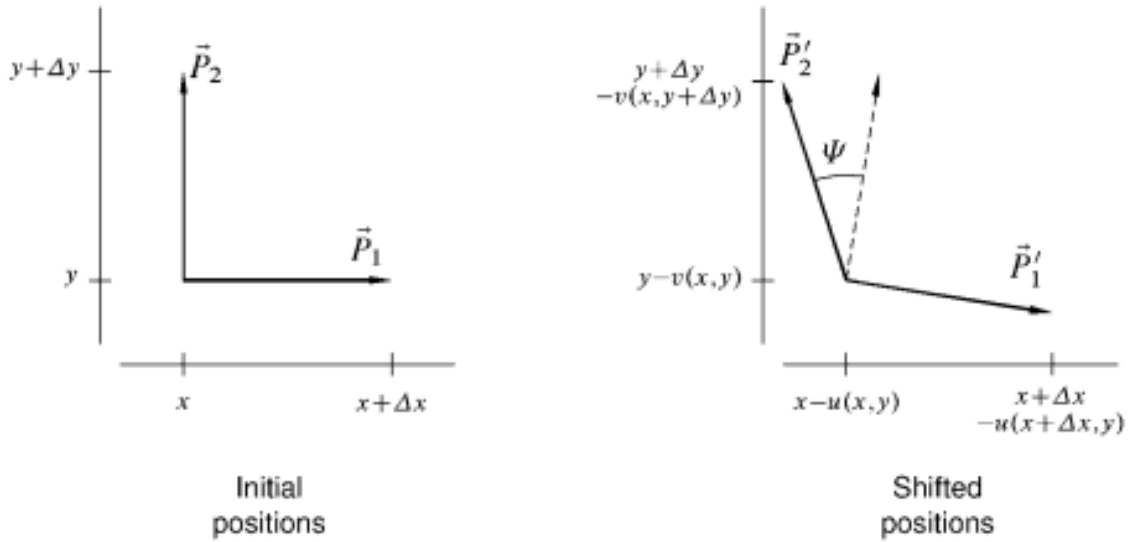


**Figure 2. 6** Parameterization of shear deformation (Fjaer, 2008)

### 2.4.5 Strain Tensor

Just like the stress tensor, it is possible to create a strain tensor by organizing Eqs. 2.4.17 - 2.4.22, where the diagonal elements contribute to volumetric deformation, while the others contribute to shear deformation.

$$\varepsilon = \begin{pmatrix} \varepsilon_x & \gamma_{xy} & \gamma_{xz} \\ \gamma_{xy} & \varepsilon_y & \gamma_{yz} \\ \gamma_{xz} & \gamma_{yz} & \varepsilon_z \end{pmatrix}. \quad (2.4.23)$$

From Eq. 2.4.23, the volumetric strain is obtained, which is the relative decrease in volume. Volumetric strain is independent of the coordinate axes, making it an invariant; so, if the coordinate system changes, the trace of the tensor in the new coordinate system still has the same value.

$$\varepsilon_{vol} = \varepsilon_x + \varepsilon_y + \varepsilon_z. \quad (2.4.24)$$

There is also another mathematical notation for strains, in which strains are defined as follows:

$$\varepsilon_{ij} = \frac{1}{2} \left( \frac{\partial u_i}{\partial x_j} + \frac{\partial u_j}{\partial x_i} \right). \quad (2.4.25)$$

## 2.4.6 Elastic Moduli

The theory of linear elasticity deals with situations where there are linear relationships between the applied stresses and the resulting strain. Many rocks behave non-linearly when subjected to large stresses; however, their behavior is described by linear relationships due to slight changes in stress. Considering an object of length  $L$  and a cross-sectional area  $A=D^2$ , like in Fig. 2.7, when the force  $F$  is applied on its end surface, the length of the sample is reduced to  $L'$ . The applied stress is then  $\sigma_x = F/A$  and the corresponding elongation is  $\epsilon_x = (L - L') / L$ . If the sample behaves linearly, there is a linear relation between  $\sigma_x$  and  $\epsilon_x$ , which is Hooke's Law (Fjaer, 2008).

$$\epsilon_x = \frac{1}{E} \sigma_x. \quad (2.4.26)$$

While the coefficient  $E$  is called Young's modulus, which is defined as the relationship between the applied stress and the resulting strain in the direction of that stress. Eq. 2.4.26 represents this modulus, which measures the stiffness of a material or the resistance of the object to being compressed by uniaxial stress. From the mathematical relationship, it can be noted that if the stress value is kept constant and the strain is varied, high strain values will result in low Young's Modulus values, meaning less stress is required to achieve these strains. Conversely, when low strain values create high Young's Modulus values, it is interpreted that the solid requires greater stress to deform.

$$E = \frac{\sigma}{\epsilon}. \quad (2.4.27)$$

It is also important to mention the erosion process. Stavropoulou et al. (1998) established that the rock will experience an erosion phenomenon, causing the rock to start losing solids from the matrix. Consequently, its geomechanical properties will begin to have less impact on the medium, which modifies the Young's Modulus, taking erosion and porosity into account,  $0 < \phi < 1$ :

$$E = \bar{E}(1 - \phi) \quad (2.4.28)$$

where  $\bar{E}$  is the Young's Modulus of the matrix and  $E$  is the Young's Modulus of the porous medium. Another consequence of the applied stress  $\sigma_x$  in **Fig. 2.7**, is an increase in the width  $D$  of the sample. The lateral elongation is  $\epsilon_y = \epsilon_z = (D - D') / D$ . In general  $D' > D$ , thus  $\epsilon_y$  and  $\epsilon_z$  become negative. The ratio is defined as:

$$\nu = -\frac{\epsilon_y}{\epsilon_x}. \quad (2.4.29)$$

Eq. 2.4.29 is another elastic parameter known as Poisson's ratio, which is defined as the negative ratio of the strain perpendicular to the applied stress to the strain in the direction of the applied stress. In other words, it is the measure of lateral expansion relative to longitudinal contraction. The range of values that exist for Poisson's ratio in rocks is between 0.15 and 0.25.

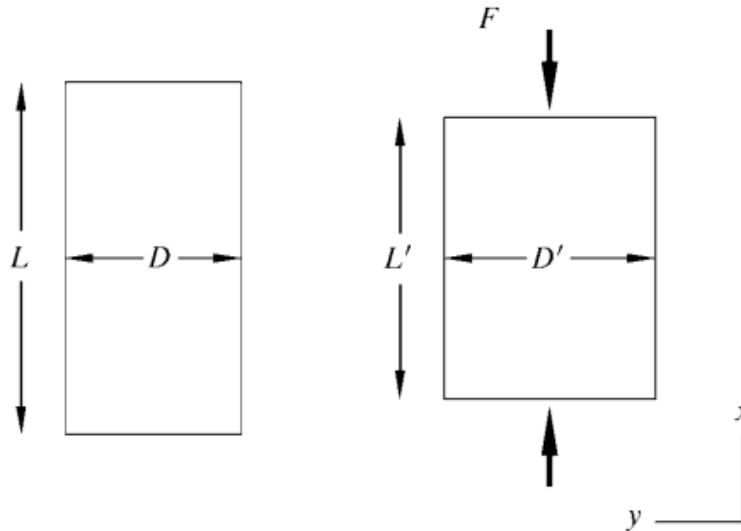


**Figure 2. 7** Deformation induced by uniaxial stress (Fjaer, 2008)

Isotropic materials are materials whose response is independent of the orientation of the applied stress; for these materials, the principal axes of stress and strain always coincide. Within the relationships between stress and strain for isotropic materials, there are other important elastic parameters known as Lamé parameters, which include  $\lambda$ , which completely characterizes the linear elastic behavior of an isotropic solid under small deformations, and  $G$ , known as the shear or rigidity modulus, which is the measure of an object's resistance to shear deformation. It is analogous to Young's modulus, with the only difference being that the former is for shear stresses and Young's modulus is for normal stresses. The Lamé parameters are defined as follows:

$$\lambda = \frac{\nu E}{(1+\nu)(1-2\nu)}, \quad (2.4.30)$$

$$G = \frac{1}{2} \left( \frac{\sigma_{12}}{\varepsilon_{12}} \right), \quad (2.4.31)$$

or

$$G = \frac{E}{2(1+\nu)}. \quad (2.4.32)$$

Another important term is the bulk modulus  $K$ , which is defined as the ratio of a hydrostatic stress  $\sigma_p$  relative to the volumetric strain  $\varepsilon_{vol}$ . It can also be defined as the measure of an object's resistance to hydrostatic compression.

$$K = \frac{\sigma_p}{\varepsilon_{vol}} = \lambda \frac{2}{3} G. \quad (2.4.33)$$

Each of these moduli  $E$ ,  $\nu$ ,  $\lambda$ ,  $K$  y  $G$ , as long as two are defined, the remaining ones can be determined since the constants are related to each other, and the moduli are measured in the same units as the stresses: Pascals, psi, or bars.

### 2.4.7 Constitutive Equation: Stress-Strain Relationship

A constitutive equation is a mathematical relationship that describes how the physical properties of a material change in response to changes in environmental or loading conditions. These equations are fundamental in engineering and physics for modeling the behavior of materials in various situations. For example, in the field of solid mechanics, a constitutive equation can describe how stress in a material varies as a function of the applied strain.

Eqs. 2.4.25 and 2.4.28 relate a stress component to a strain component. In general terms, each component of a strain is a linear function of all the stress components. With the parameters defined in the previous section, it is possible to formulate a constitutive equation that relates strain and stress in three dimensions. Considering an isotropic medium simplifies these equations, leaving only one Young's modulus and one Poisson's ratio for the three axes. Additionally, by assuming that the rock's behavior is elastic, the following simplified form is obtained:

$$E = \frac{\sigma_{11}}{\varepsilon_{11}} = \frac{\sigma_{22}}{\varepsilon_{22}} = \frac{\sigma_{33}}{\varepsilon_{33}}. \quad (2.4.34)$$

and

$$\nu = -\frac{\varepsilon_{11}}{\varepsilon_{22}} = -\frac{\varepsilon_{11}}{\varepsilon_{33}}. \quad (2.4.35)$$

The Strain in the direction  $\varepsilon_{11}$  due to the stresses in the three principal directions:

$$\varepsilon_{11} = \varepsilon_{11\sigma_{11}} + \varepsilon_{11\sigma_{22}} + \varepsilon_{11\sigma_{33}}. \quad (2.4.36)$$

Substituting the Eqs. 2.4.31 and 2.4.32 in the Eq. 2.4.33:

$$\varepsilon_{11} = \frac{\sigma_{11}}{E} - \frac{\sigma_{22}\nu}{E} - \frac{\sigma_{33}\nu}{E}. \quad (2.4.37)$$

With the previous equation, the generalization of Young's modulus equations and Poisson's ratios in all directions will give the following result:

$$\begin{cases} \varepsilon_{11} = \frac{\sigma_{11}}{E} - \frac{\sigma_{22}\nu}{E} - \frac{\sigma_{33}\nu}{E} \\ \varepsilon_{22} = \frac{\sigma_{22}}{E} - \frac{\sigma_{11}\nu}{E} - \frac{\sigma_{33}\nu}{E} \\ \varepsilon_{33} = \frac{\sigma_{33}}{E} - \frac{\sigma_{11}\nu}{E} - \frac{\sigma_{22}\nu}{E} \end{cases} \quad (2.4.38)$$

For shear stresses, the definition of the Shear Modulus is used in Eq. 2.4.30, arriving at:

$$\begin{cases} \varepsilon_{12} = \frac{\sigma_{12}}{2G} \\ \varepsilon_{13} = \frac{\sigma_{13}}{2G} \\ \varepsilon_{23} = \frac{\sigma_{23}}{2G} \end{cases} \quad (2.4.39)$$

Eq. 2.4.31 is substituted into Eq. 2.4.37:

$$\begin{cases} \varepsilon_{12} = \frac{\sigma_{12}(1+\nu)}{E} \\ \varepsilon_{13} = \frac{\sigma_{13}(1+\nu)}{E} \\ \varepsilon_{23} = \frac{\sigma_{23}(1+\nu)}{E} \end{cases} \quad (2.4.40)$$

Eqs. 2.4.36 and 2.4.38 will be represented in matrix form, using Voigt notation:

$$\begin{bmatrix} \varepsilon_{11} \\ \varepsilon_{22} \\ \varepsilon_{33} \\ 2\varepsilon_{12} \\ 2\varepsilon_{13} \\ 2\varepsilon_{23} \end{bmatrix} = \begin{bmatrix} \frac{1}{E} & -\frac{\nu}{E} & -\frac{\nu}{E} & 0 & 0 & 0 \\ -\frac{\nu}{E} & \frac{1}{E} & -\frac{\nu}{E} & 0 & 0 & 0 \\ -\frac{\nu}{E} & -\frac{\nu}{E} & \frac{1}{E} & 0 & 0 & 0 \\ 0 & 0 & 0 & \frac{2(1+\nu)}{E} & 0 & 0 \\ 0 & 0 & 0 & 0 & \frac{2(1+\nu)}{E} & 0 \\ 0 & 0 & 0 & 0 & 0 & \frac{2(1+\nu)}{E} \end{bmatrix} \begin{bmatrix} \sigma_{11} \\ \sigma_{22} \\ \sigma_{33} \\ \sigma_{12} \\ \sigma_{13} \\ \sigma_{23} \end{bmatrix} \quad (2.4.41)$$

In matrix form, it is represented as follows:  $\varepsilon = D\sigma$ ; if one wishes to express Eqs. 2.4.36 and 2.4.38 with stress as the dependent variable, then the inverse of  $D$  is obtained:

$$\begin{bmatrix} \sigma_{11} \\ \sigma_{22} \\ \sigma_{33} \\ \sigma_{12} \\ \sigma_{13} \\ \sigma_{23} \end{bmatrix} = \frac{E}{(1+\nu)(1-2\nu)} \begin{bmatrix} 1-\nu & \nu & \nu & 0 & 0 & 0 \\ \nu & 1-\nu & \nu & 0 & 0 & 0 \\ \nu & \nu & 1-\nu & 0 & 0 & 0 \\ 0 & 0 & 0 & \frac{(1-2\nu)}{2} & 0 & 0 \\ 0 & 0 & 0 & 0 & \frac{(1-2\nu)}{2} & 0 \\ 0 & 0 & 0 & 0 & 0 & \frac{(1-2\nu)}{2} \end{bmatrix} \begin{bmatrix} \varepsilon_{11} \\ \varepsilon_{22} \\ \varepsilon_{33} \\ 2\varepsilon_{12} \\ 2\varepsilon_{13} \\ 2\varepsilon_{23} \end{bmatrix}. \quad (2.4.42)$$

Substituting Eqs. 2.4.29 and 2.4.31 into 2.4.40 yields the following relationships:

$$\begin{cases} \sigma_{11} = (\lambda + 2G)\varepsilon_{11} + \lambda\varepsilon_{22} + \lambda\varepsilon_{33} \\ \sigma_{22} = (\lambda + 2G)\varepsilon_{22} + \lambda\varepsilon_{11} + \lambda\varepsilon_{33} \\ \sigma_{33} = (\lambda + 2G)\varepsilon_{33} + \lambda\varepsilon_{22} + \lambda\varepsilon_{11} \\ \sigma_{12} = 2G\varepsilon_{12} \\ \sigma_{13} = 2G\varepsilon_{13} \\ \sigma_{23} = 2G\varepsilon_{23} \end{cases}. \quad (2.4.43)$$

The relationships from Eq. 2.4.42 can be written in a more compact form using Eq 2.4.25:

$$\sigma_{ij} = \lambda\varepsilon_{vol}\delta_{ij} + 2G\varepsilon_{ij}. \quad (2.4.44)$$

where  $\delta_{ij}$  is the Kronecker delta, which is a function of two variables:

$$\delta_{ij} = \begin{cases} 1 & \text{if } i = j \\ 0 & \text{if } i \neq j \end{cases}. \quad (2.4.45)$$

## 2.4.8 Poroelasticity

Is the way rocks react to elastic responses, stresses, etc., mostly depends on the non-solid parts of the materials. The pore space is not only important for producing hydrocarbons from reservoirs but also plays an important role in the mechanical behavior of rocks. An approach based on Biot's theory considers a macroscopic description of the porous and permeable medium, idealizing it as homogeneous and isotropic, allowing the study of static and dynamic mechanical properties. This approach is known as the Gassmann limit.

### 2.4.8.1 Suspension of Solid Particles in a Fluid

Assuming a simple, porous medium, in which the solids and fluid deform independently of one another, where there is a suspension of solid particles in the fluid or a completely water-saturated unconsolidated sand. If such a mixture is placed in a container, the volumetric deformation due to an external pressure  $\sigma_p$ :

$$\varepsilon_{vol} = \frac{\sigma_p}{K_{eff}}. \quad (2.4.46)$$

where  $K_{eff}$  is the bulk modulus of the mixture; the total deformation must be equal to the sum of the deformations of each component, weighted by the volume fraction of each component.

$$\varepsilon_{vol} = \frac{V_s}{V_{tot}} \varepsilon_{vol,s} + \frac{V_f}{V_{tot}} \varepsilon_{vol,f}. \quad (2.4.47)$$

where the subscripts  $s$  and  $f$  mean solid and fluid, respectively, and  $V_{tot}$  is the total volume. We define porosity as the volume occupied by the fluid relative to the total volume:

$$\phi = \frac{V_f}{V_{tot}}. \quad (2.4.48)$$

$$\frac{V_s}{V_{tot}} = 1 - \phi. \quad (2.4.49)$$

The volumetric deformations of the solid and the fluid are given by the bulk modulus, using Eqs.2.4.33 and rewriting Eq. 2.4.47:

$$\varepsilon_{vol} = (1 - \phi) \frac{\sigma_p}{K_s} + \phi \frac{\sigma_p}{K_f}. \quad (2.4.50)$$

Combining Eqs. 2.4.46 and 2.4.50, the effective modulus of the suspension can be defined:

$$\frac{1}{K_{eff}} = \frac{1-\phi}{K_s} + \frac{\phi}{K_f}. \quad (2.4.51)$$

### 2.4.8.2 Effective stress

As mentioned before, which rocks react to mechanical stresses and deformations do not depend solely on the solid parts; the fluids within the rock also exert pressure on it. The fluid in the pores affects the way rocks fail due to pore pressure and the chemical interaction between the rock and fluid. For the purposes of this work, only the influence of the mechanical effect generated by pore pressure will be discussed,  $P_p$ . Such mechanical stress, a pressure that acts perpendicularly, can be considered a tensile stress. However, in the case of a rock with isotropic behavior, the effect will be the same in any of the three orthogonal directions. Terzaghi (1923) defined the concept of effective stress, using the following considerations:

1. Increasing the external hydrostatic pressure produces the same change in the material's volume as decreasing the pore pressure by the same amount.
2. The shear stress depends only on the difference between a normal stress and the pore pressure.
3. The soil is homogeneous and isotropic.
4. The soil is fully saturated with a fluid.
5. The solid particles are incompressible.
6. Compression and flow occur in one direction.
7. Darcy's Law is valid for all hydraulic gradients.

The mathematical form to express it is as follows:

$$\sigma' = \sigma_{ij} - \delta_{ij}P_p. \quad (2.4.52)$$

This means that the pore pressure only exerts normal stresses on the stress tensor, as the fluid pressure does not act in a shear manner (Zoback, 2007). One way to express the pore pressure is as follows:

$$P_p = \begin{bmatrix} P_p & 0 & 0 \\ 0 & P_p & 0 \\ 0 & 0 & P_p \end{bmatrix}. \quad (2.4.53)$$

The difference between the stress tensor and the pore pressure will result in the effective stress, which is the stress the rock grains support themselves. Using Eqs. 2.4.52 and 2.4.53, we obtain:

$$\sigma' = \begin{bmatrix} \sigma_{11} & \sigma_{12} & \sigma_{13} \\ \sigma_{12} & \sigma_{22} & \sigma_{23} \\ \sigma_{13} & \sigma_{23} & \sigma_{33} \end{bmatrix} - \begin{bmatrix} P_p & 0 & 0 \\ 0 & P_p & 0 \\ 0 & 0 & P_p \end{bmatrix} = \begin{bmatrix} \sigma_{11} - P_p & \sigma_{12} & \sigma_{13} \\ \sigma_{12} & \sigma_{22} - P_p & \sigma_{23} \\ \sigma_{13} & \sigma_{23} & \sigma_{33} - P_p \end{bmatrix}. \quad (2.4.54)$$

Just like Young's modulus, the geomechanical parameters begin to lose value as the rock starts to erode, leading to the following equation:

$$\sigma' = (1 - \phi) \overline{\sigma'} = (1 - \phi) \begin{bmatrix} \sigma_{11} - P_p & \sigma_{12} & \sigma_{13} \\ \sigma_{12} & \sigma_{22} - P_p & \sigma_{23} \\ \sigma_{13} & \sigma_{23} & \sigma_{33} - P_p \end{bmatrix}. \quad (2.4.55)$$

### 2.4.9 Mohr's Circles

Mohr's circles are a 2-D geometric representation of stresses, which is very useful for making quick and efficient estimates to visualize the relationship between normal and shear stresses at a point on different planes. Fig. 2.8 shows a triaxial test in which two stresses act on an object. When the compressive force of the stresses exceeds the rock's compressive strength, the rock fractures and creates a failure plane. Therefore, Mohr's circles decompose the compressive force into a normal stress and a shear stress acting on the failure plane. (Télléz, 2021)

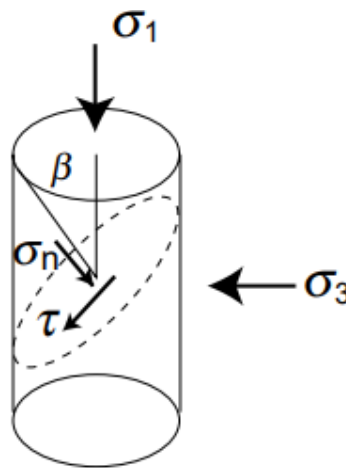


**Figure 2.8** Stress Diagram of a Triaxial Tests (Zoback, 2007)

A diagram like Fig. 2.9 shows a body subjected to a situation like a triaxial test. According to Newton's fundamental law of dynamics, it is stipulated that the resultant set of forces acting on a body is equal to the mass of the body multiplied by its acceleration:

$$\sum_{i=1}^n \vec{F}_i = m\vec{a}. \quad (2.4.56)$$

Suppose it is necessary to obtain the relationship between the stresses generated in the areas  $A_x$  y  $A_y$ , considering very small deformations. In that case, the acceleration is approximated to zero, setting equation (2.4.56) to zero. The force balance in the  $x$ -axis is as follows:

$$\sum_{i=1}^n \bar{F}_x = -\sigma_x A_x - \tau_n A_n \text{sen}(\theta) + \sigma_n A_n \cos(\theta) = 0. \quad (2.4.57)$$

And for the force balance in the  $y$ -axis:

$$\sum_{i=1}^n \bar{F}_y = -\sigma_y A_y + \tau_n A_n \cos(\theta) + \sigma_n A_n \text{sen}(\theta) = 0. \quad (2.4.58)$$

where  $A_n$  is the normal area where the normal stress acts ( $\sigma_n$ ) on the inclined plane at  $\theta$  degrees. Considering that  $A_x = A_n \cos(\theta)$  and  $A_y = A_n \text{sen}(\theta)$ , rewriting Eqs. 2.4.57 and 2.4.58 and solving for  $A_n$ :

$$-\sigma_x \cos(\theta) - \tau_n \text{sen}(\theta) + \sigma_n \cos(\theta) = 0, \quad (2.4.59)$$

$$-\sigma_y \text{sen}(\theta) + \tau_n \cos(\theta) + \sigma_n \text{sen}(\theta) = 0. \quad (2.4.60)$$

If equation (2.4.59) is multiplied by  $\cos(\theta)$ , Eq. 2.4.60 by  $\text{sen}(\theta)$  and both are added, we obtain:

$$-\sigma_x \cos^2(\theta) - \tau_n \cos(\theta) \text{sen}(\theta) + \sigma_n = 0. \quad (2.4.61)$$

Considering the following trigonometric relationships:

$$\cos^2(\theta) = \frac{1 + \cos(2\theta)}{2}, \quad (2.4.62)$$

$$\text{sen}^2(\theta) = \frac{1 - \cos(2\theta)}{2}. \quad (2.4.63)$$

and substituting into Eq. 2.4.61 we obtain:

$$\sigma_n = \frac{(\sigma_x + \sigma_y)}{2} + \frac{(\sigma_x - \sigma_y)}{2} \cos(2\theta). \quad (2.4.64)$$

To obtain the shear stress on the plane from equations (2.4.59) and (2.4.60), they should be multiplied by  $\text{sen}(\theta)$  and  $\text{cos}(\theta)$  respectively to subtract them and obtain the following:

$$\tau_n = -\frac{(\sigma_x - \sigma_y)}{2} \text{sen}(2\theta). \quad (2.4.65)$$

Equations (2.6.64) and (2.6.65) represent parametric equations to create Mohr's circles. In Fig 2.10 the coordinates are  $\sigma_n$  y  $\tau_n$  whereas  $2\theta$  is the parameter:

$$\left[ \sigma_n - \frac{(\sigma_x + \sigma_y)}{2} \right]^2 + \tau_n^2 = \left[ \frac{(\sigma_x - \sigma_y)}{2} \right]^2. \quad (2.4.66)$$

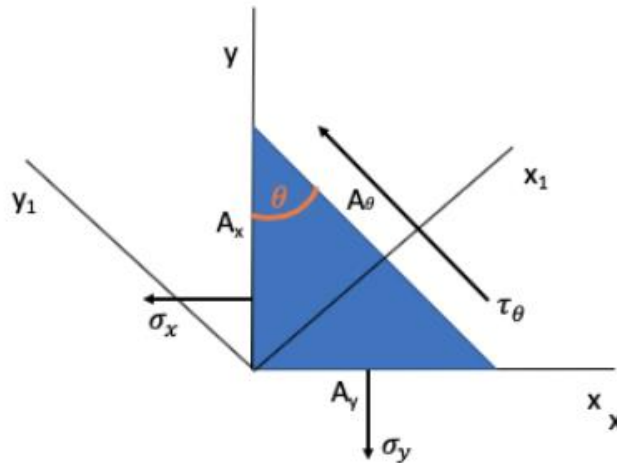


**Figure 2.9** Object Subject to Normal and Shear Stresses (Télez, 2021)

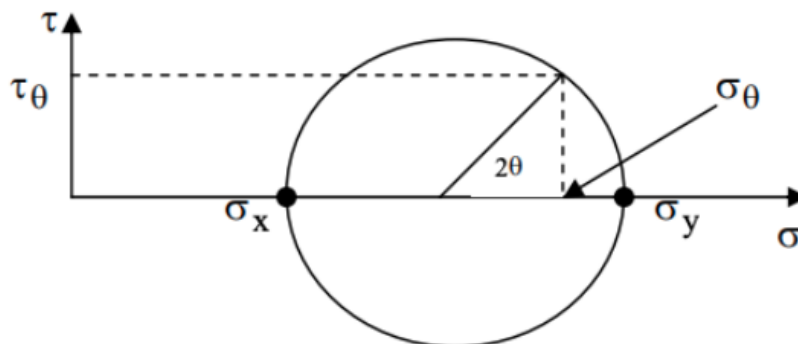


**Figure 2.10** Mohr's Circle in Two Dimensions

### 2.4.10 The Mohr-Coulomb criterion

The Mohr-Coulomb failure criterion, first introduced by Coulomb in 1773, through his experimental studies, found that soil failure plane occurs along the plane due to shear stress ( $\tau$ ). He found two phenomena: firstly, resistance to failure is observed due to a frictional force, which is proportional to the normal stress ( $\sigma$ ) acting on the plane and multiplied by a constant ( $\mu_f$ ). Secondly, material failure does not manifest until an initial force, or an internal cohesive force of the material is overcome ( $C$ ). As a result, a mathematical model was developed that combines the values of shear and normal stresses to predict the occurrence of failure in the material.

The Mohr-Coulomb criterion is represented in Fig. 2.11 and is obtained through triaxial or shear tests. These tests provide the angles of the failure plane and the cohesion of the material. By plotting these data, a diagram similar to Fig. 2.11 is obtained, where the points of Mohr's circle can be visualized. If a straight line touches the circle, it is considered that the material will fail. From the relationship between these parameters, the following equation is obtained:

$$\tau = \sigma \tan(\phi) + C. \quad (2.4.67)$$

In Eq. 2.4.67, the parameter  $C$ , representing cohesion, describes a linear relationship between shear stress and normal stress. This parameter intercepts the y-axis at a point that reflects that, in the absence of normal stress, a minimum shear stress is needed to initiate failure in the material. In other words, cohesion indicates the intrinsic resistance of the material to deformation and failure, even when no normal stress is applied. Another way to describe the Mohr-Coulomb criterion is as follows:

$$\tau = \sigma \mu + C. \quad (2.4.68)$$

where  $\mu$  represents the coefficient of friction, which depends on the slope of the graph. The criterion indicates that a state of stress below the straight line in Fig. 2.11 will not generate failure on any plane. If the stresses reach the failure line, then the rock will fail in shear. Mathematically, rock failure will occur when:

$$\tau > \sigma \mu + C. \quad (2.4.69)$$

Another form to represent Eq. 2.4.67 is observed in **Fig. 2.11**, where it is shown that  $|CP| = (|AO| + |OC|) \text{sen}(\phi)$  and considering that  $\sigma_x$  y  $\sigma_y$  are replaced by  $\sigma_1$  y  $\sigma_3$ :

$$\frac{1}{2}(\sigma_1 - \sigma_3) = \left[ \cot(\phi) C + \frac{1}{2}(\sigma_1 + \sigma_3) \right] \text{sen}(\phi), \quad (2.4.70)$$

$$\frac{1}{2}(\sigma_1 - \sigma_3) = \left[ \cos(\phi) C + \frac{1}{2}(\sigma_1 + \sigma_3) \right] \sin(\phi). \quad (2.4.71)$$

If the following terms are considered:

$$\sigma_m = \frac{1}{2}(\sigma_1 + \sigma_3), \tau_m = \frac{1}{2}(\sigma_1 - \sigma_3)$$

and they are substituted into Eq. 2.4.71, the failure criterion would be represented as:

$$\tau_m = \cos(\phi) C + \sigma_m \sin(\phi). \quad (2.4.72)$$

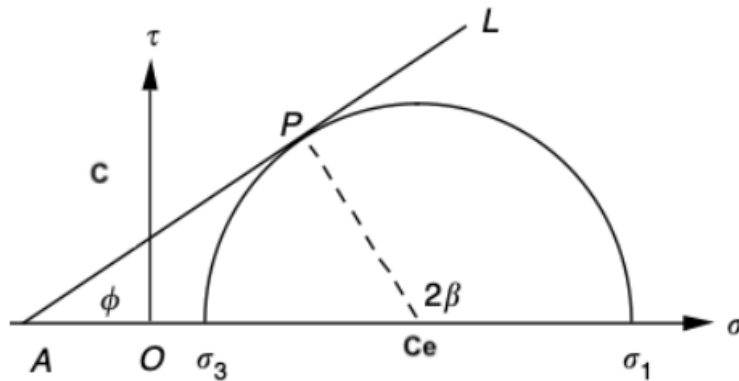


**Figure 2.11** Mohr-Coulomb Failure Criterion with fault curve with AL line. Failure will occur on this specific plane at an angle  $\beta$ , marked by the CP line (Jaeger, 2007)

### 2.4.11 Cohesion

Cohesion in rocks refers to the internal resistance of a rock to being fractured or displaced by external forces. It measures the ability of the individual particles or grains of the rock to stay bonded together. This property is influenced by several factors, such as mineralogical composition, rock texture, porosity, fractures, and fluids in the rock's pores.

Cohesion is one of the two main components of rock strength, along with friction. Together, cohesion and friction determine the overall resistance of the rock to fracture or deformation when subjected to external forces, such as soil load or underground fluid pressure. The grains are tightly bonded in more cohesive rocks, making the rock more resistant to fracture and deformation. On the other hand, in less cohesive rocks, the grains may be less bonded and more prone to separation under load.

Plumb et al. (1994) found a relationship between cohesion and porosity, stating that lower porosity tends to result in higher cohesion, meaning the rock is highly compacted. Conversely, rocks with high porosity tend not to be well compacted. Rumpf et al. (1995) describe a simple damage law, which outlines the relationship between cohesion and porosity, considering the phenomenon of erosion:

$$C = \bar{C}(1 - \phi) \quad (2.4.73)$$

If we apply Eq. 2.4.73 to the Mohr-Coulomb failure criterion, we obtain the following:

$$\tau = \sigma\mu + \bar{C}(1 - \phi) \quad (2.4.74)$$

Eq 2.4.74 refers to the Mohr-Coulomb failure criterion, taking into consideration the erosion of the rock, increased porosity, and decreased cohesion.

### 2.4.12 Local stresses

This theory describes a reservoir under an in-situ stress system (vertical stress ( $\sigma_v$ ), maximum horizontal stress ( $\sigma_H$ ), and minimum horizontal stress ( $\sigma_h$ )). However, this stress system does not match the stress system that develops during the drilling of a well, as drilling physically, chemically, thermodynamically, and hydraulically alters the stress system around the reservoir, and the in-situ stress system redistributes to a local stress system. The new local stress system is shown in Fig. 2.12, where the stresses around the wellbore wall are described by the radial stress ( $\sigma_r$ ), tangential stress ( $\sigma_\theta$ ), and axial stress ( $\sigma_a$ ).

According to Pasic et al. (2007), the local stresses result from the combination of in-situ stresses and hydraulic effects on the wellbore wall ( $r=r_w$ ), and are described as follows:

$$\sigma_r = p_{wf}, \quad (2.4.75)$$

$$\sigma_\theta = (\sigma_x - \sigma_y) - (\sigma_x - \sigma_h) \cos(2\theta) - p_{wf}. \quad (2.4.76)$$

With the previous equations and **Fig 2.12**, it can be observed that the radial stress ( $\sigma_r$ ) acts in all directions perpendicular to the well and depends on the flowing bottomhole pressure ( $p_{wf}$ ), while the tangential stress ( $\sigma_\theta$ ) is a combination of stresses surrounding the well and is the most disturbed during production.

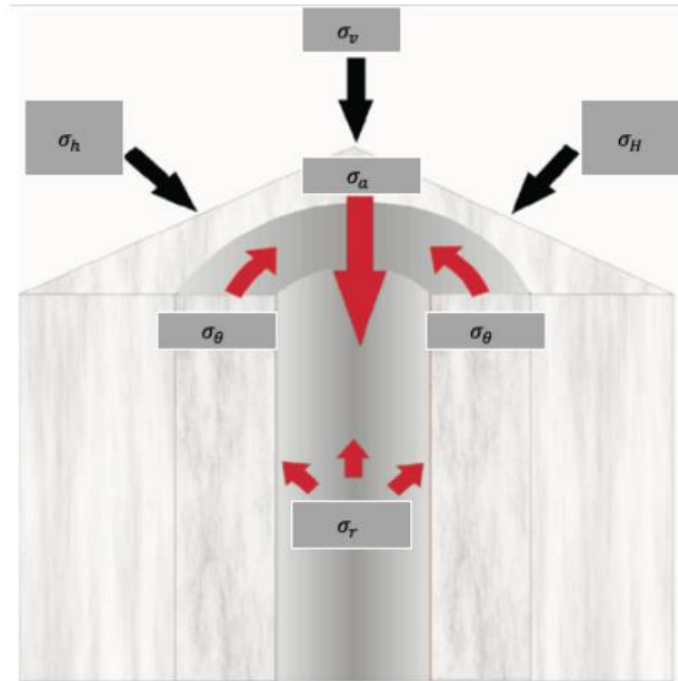


Figure 2. 12 Local Stress System Around a Well (Pasic, 2007)

## 2.5 Solids Production

When hydrocarbons are extracted from the reservoir, sometimes eroded solid particles accompany the fluid to the well, an unwanted byproduct known as solids production. Produced solids can vary from a few grams per cubic meter of fluid, representing a minor issue, to catastrophic amounts that can completely fill the borehole. It is estimated that 70% of the world's hydrocarbon reserves are found in reservoirs where solids production is a significant probability at some point. This phenomenon is common in sand reservoirs but also in carbonate and coal reservoirs.

The main cause of solids production is the mechanical failure of the formation near the well due to the effective stresses acting on the borehole walls and flow conditions that exceed the mechanical strength of the reservoir rocks. The collapse and disintegration of carbonate formations in oil wells can occur under certain circumstances, but their frequency depends on various geological, operational, and environmental factors. Some carbonate formations may be more prone to collapse and disintegration than others, depending on factors such as mineralogical composition, porosity, fractures, and geological history. For example, carbonate formations with high porosity and weaker structure may be more susceptible to these issues.

The extraction of hydrocarbons can affect the stability of the carbonate formation. Fluid extraction can reduce reservoir pressure and alter stress conditions in the formation, increasing the risk of collapse and disintegration. Additionally, the techniques used during

drilling and well completion can influence the stability of the carbonate formation. For example, applying high drilling pressures or using inadequate drilling fluids can increase the risk of formation collapse and disintegration.

Although the collapse and disintegration of carbonate formations can occur in oil wells, they are not common events in all operations. However, it is crucial that well operators are aware of the factors that can increase the risk of these issues and adopt appropriate preventive and mitigation measures to ensure the safety and efficiency of operations.

Solid's production in carbonate reservoirs is a common factor in many wells during production stages and especially under depletion conditions. Many well-established techniques for predicting sand production exist, while for carbonates, there are only a few case studies of these techniques (Asadi, 2017).

### **2.5.1 Well Completion and Solids Control**

A well-completion method that does not include specific equipment to prevent or reduce the consequences of solids production is an open hole or natural completion. This technique leaves the hole without casing and cement, allowing hydrocarbons to flow into the well through its walls. The flow area is calculated as the hole's circumference multiplied by the length of the open hole section within the reservoir. This simple completion requires the formation to be relatively strong and stable. Otherwise, support can be added through gravel packing, which acts as a filter for solids while allowing hydrocarbon production through the gravel. However, gravel packing increases costs and can reduce well productivity due to potential clogging of these filters.

In weak or unconsolidated formations, casings are installed and cemented in the formation to stabilize the hole. Subsequently, perforations are made in the casings in the reservoir zones to allow hydrocarbons to flow into the well, creating cylindrical holes of 1-2 cm in diameter and 20-50 cm in length. The size and shape of these perforations vary considerably depending on the type of charge used, the properties of the formation, and the well pressure relative to the pore pressure in the formation during the creation of the perforations.

A third well-completion alternative is to create a fracture in the formation and fill it with proppant. This technique creates a highly permeable channel in the formation, facilitating hydrocarbon production. It is widely used in low-permeability and unconsolidated formations. Each technique has advantages and disadvantages, and the choice of the most suitable one depends on the reservoir's specific characteristics and operational objectives.

### **2.5.2 Solids Production in Limestone Reservoirs**

Solid's production can be a significant problem in limestone reservoirs. Predicting and controlling limestone production can be more problematic than sand production (Fjaer, 2008). In some cases, limestone is produced slowly at a relatively constant rate. Similarly, there are occasions when large amounts of limestone enter the well, which are sufficient to kill the well.

Fjaer (2008) believes that the mechanisms causing sand production can also cause limestone production under certain conditions and effects related to the type of rock. First, the matrix permeability in limestones is low, on the order of 1 md. This implies that tensile failure conditions are more likely to occur in limestones. Second, the collapse pressure for high-porosity limestones is low, so this type of failure should be considered along with shear and tensile failure.

When a rock collapses, the pore volume is significantly reduced. This induces a sudden increase in pore pressure, which takes time to dissipate in a low-permeability material like limestone. The result can be a significant increase in pore pressure, leading to an effective mean tensile stress and liquefaction conditions.

### **2.5.3 Sand Control Method Applied in Carbonate Reservoirs**

The methods for in-situ stress and rock strength characterization are well-defined, and there are many publications for predicting sand production experimentally, analytically, and numerically. However, there are few of these techniques for solids production in carbonate reservoirs.

Asadi and Khaksar (2017) presented a field case study applying an analytical sand evaluation technique to predict solids production in a carbonate gas reservoir in the Vietnam Sea. The method consists of a poroelastic solution, which considers stresses, rock strength, reservoir, and well pressures, as well as the trajectory of the perforations and the well to predict the occurrence of solids. The properties of the carbonate reservoir in the Nam Con Son (NCS) block are relatively constant; however, the carbonates in the reservoir interval are highly heterogeneous, with poorly sorted grains, mostly limestones and dolomites. The reservoir has an average permeability of 1.0 Darcy, a porosity of 36%, reservoir pressure between 2000 and 2050 psi, and a formation temperature of 70 to 80 °C.

The analytical sand prediction method was proposed by Wilson (2002) and Rahman (2008). It assumes that the rock surrounding a well or a perforation with arbitrary orientation fails in shear when the maximum effective compressive stress exceeds the effective strength of the formation. The effective strength of the formation ( $U$ ) is determined from a calibrated core applied to a Thick-Walled Cylinder test (TWC).  $U$  is multiplied by an empirical factor called the Effective Strength Factor (ESF), which relates to sanding data from production data or well tests. Observations of solids production during a formation test, formation fluid testing and sampling, and production data are ideal for calibrating the ESF value for reservoir and completion types.

All producing wells in the field are completed in open holes with gravel packing and a screen, where no solids production has been observed at the surface, making it difficult to calibrate the solids production model. However, due to the decline in production of two observation wells after a significant pressure drawdown, it is believed that production-induced rock failure has caused clogging in the screen by fine-grained solids, reducing production.

# 3. Hydromechanical Model

This section addresses the hydromechanical aspects of solids production when carbonates disintegrate from the matrix and from the fluids in collapse situations. The processes involved in this phenomenon are associated with the transport of solids and fluids, rock/fluid interaction, and rock deformation. In this section, only the first and third phenomena are described.

Hydromechanical instability is caused by the internal erosion of the rock caused by erosive agents such as water. The friction of this fluid generates the decoupling and movement of solid particles. Most carbonates tend to present fractures, which facilitate the erosion of the rock matrix by fluids.

(Vardoulakis, Stavropoulou, & Papanastasiou, 1996) They developed a proposal that presents a deterministic method based on the three-phase mixture theory for a continuous medium, composed of solids, movable solids, and fluids. This method considers rock deformation under radial flow, and radial symmetry around the wellbore axis is assumed. These conditions imply that the deformation in the well is analyzed in a plane normal to its axis.

The three-phase mixture approach allows for more accurate modeling of hydromechanical phenomena, considering the interaction between fixed solids, movable solids, and fluids within the formation. This method considers how the stress field induces deformations in the solid skeleton, and how these deformations can influence the transport of solids and fluids. However, it is assumed that the deformation does not significantly alter the flow conditions.

This methodological approach is useful for addressing hydromechanical instability and internal erosion in carbonate formations, providing a more detailed understanding of the processes that lead to solids production and their impact on well integrity.

## 3.1 Mathematical Model

Consider a volume element  $dV$  of a saturated porous medium. The volume consists of the following components: solid ( $s$ ), fluid ( $ff$ ), and movable solids ( $fs$ ) with their respective mass  $dM_s$ ,  $dM_{ff}$ ,  $dM_{fs}$ , and volume  $dV_s$ ,  $dV_{ff}$ ,  $dV_{fs}$ . In **Fig 3.1** the symbol  $dV_v$  is used to indicate the volume of interconnected pores in the medium, which is occupied by a mixture of fluids and movable particles:

$$dV_v = dV_{ff} + dV_{fs}. \quad (3.1.1)$$

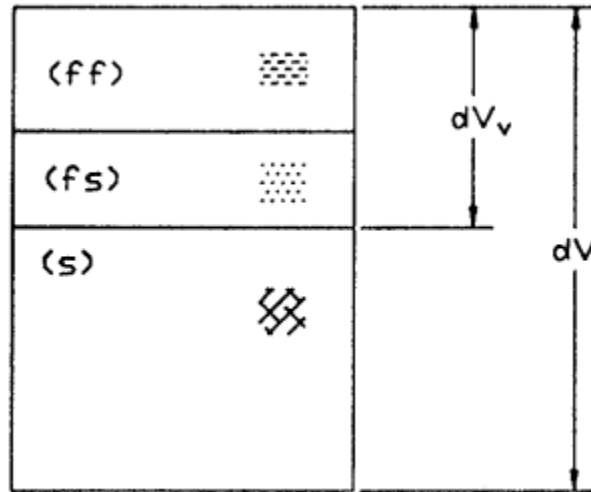


**Figure 3. 1** Phase Diagram of a Porous Medium Saturated with a Fluid and Movable Particles. (Vardoulakis, Stavropoulou, & Papanastasiou, 1996)

The movable particles are in suspension and move along with the fluid. Any other particle that is trapped within the pore space will be regarded part of the solid phase. It is also assumed that the fluid and the movable particles have the same velocity at any given instant. Similarly, it is considered that the solid phase refers only to the flow of the solid part of the rock moving as a continuous medium, as shown in Fig. 3.2. According to this, the velocities of the different components are defined as follows:

$$v_i^{fs} = v_i^{ff} = \bar{v}_v, \quad (3.1.2)$$

$$v_i^s = 0. \quad (3.1.3)$$

The previous expressions explain that solid particles can have negligible movement and be considered part of the solid phase, or they can have the velocity of the fluid and be considered part of the mixture occupying the pore space.

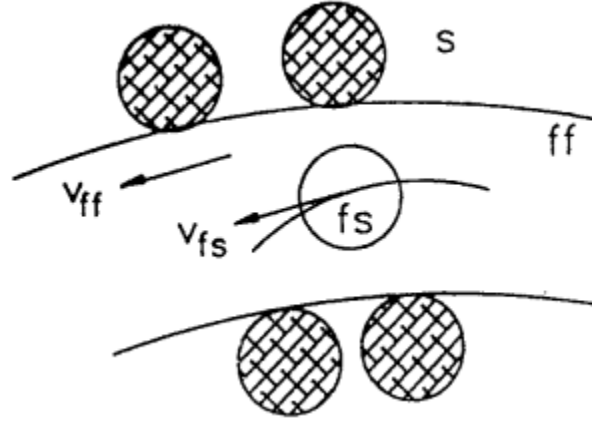


**Figure 3. 2** Pore Channel with Movable Particles (*Vardoulakis, Stavropoulou, & Papanastasiou, 1996*)

The volume fraction of the pores is expressed as absolute porosity:

$$\phi = \frac{dV_v}{dV} \quad (3.1.4)$$

The concentration of movable solids is indicated as follows:

$$c = \frac{dV_{fs}}{dV_v} \quad (3.1.5)$$

The variables  $c$  y  $\phi$  are a function of space ( $x_i$ ) and time ( $t$ ). The fluid densities  $\rho_{ff}$  and of the movable fluids  $\rho_{fs}$  are define as follows:

$$\rho_f = \frac{dM_{ff}}{dV_{ff}}, \quad (3.1.6)$$

$$\rho_s = \frac{dM_{fs}}{dV_{fs}} = \frac{dM_s}{dV_s}. \quad (3.1.7)$$

The partial density of the mixture is:

$$\bar{\rho} = \frac{dM_{ff} + dM_{fs}}{dV_{ff} + dV_{fs}}. \quad (3.1.8)$$

Taking into consideration Eqs. 3.1.5, 3.1.6, 3.1.7, and substituting into Eq. 3.1.8:

$$\bar{\rho} = (1 - c)\rho_f + c\rho_s. \quad (3.1.9)$$

Eq. 3.1.9 defines the density of the mixture, where it can be understood that a higher concentration results in a more significant influence of the solid. The partial density of the movable solid phase can be defined as follows:

$$\bar{\rho}_{fs} = \frac{dM_{fs}}{dV} = c\phi\rho_s. \quad (3.1.10)$$

The discharge velocity of the mixture is defined as:

$$v_D = \frac{dV}{dS dt}. \quad (3.1.11)$$

where  $dV$  is the flow volume through the cross-sectional area  $dS$  in each time  $dt$ . The variable  $v_D$  refers to Darcy's velocity, representing fluid flow velocity through the porous medium.

## 3.2 Law of Conservation of Mass

This section will present the mass conservation equations to describe the movement of the solid phase, which includes moving particles and fluid. The principle of mass conservation states that the matter within a closed system remains constant in quantity; this implies that the amounts of mass at different times and places within the system must remain constant.

### 3.2.1 Relation of Mass with a Control Volume

The control volume is defined by the symbol  $\Omega$  and is bounded by a surface  $\partial\Omega$ . According to the law of conservation of mass, the change in mass within  $\Omega$  is equal to the difference between the amount of mass entering the system  $\Omega$  and the amount of mass leaving it. In this context, the control volume  $\Omega$  represents a porous rock saturated with fluid and movable solids and is characterized by having a fixed volume and position.

Density, which relates mass and volume, is a property of the solid and the fluid.

$$\rho = \frac{m}{V\Omega}. \quad (3.2.1)$$

Density is an intensive property defined in any region of the system  $\Omega$ ; in the case of a large reservoir, density, and porosity may vary. If  $\Omega$  is divided into very small parts, this would approximate the problem such that:

$$M_i = \rho_i V_i \text{ for } i=1, 2, N$$

If the total mass of the system is calculated, we obtain:

$$m = \sum_{i=1}^N M_i = \sum_{i=1}^N \rho_i V_i. \quad (3.2.2)$$

To represent a continuous medium, the system must be divided into the maximum known number of parts, when  $N \rightarrow \infty$ , rewriting the previous equation:

$$m = \lim_{N \rightarrow \infty} \sum_{i=1}^N \rho_i V_i. \quad (3.2.3)$$

Eq. 3.2.3 is the definition of a volume integral, so the equation for the mass contained in the entire system is defined as follows:

$$m = \int_{\Omega} \rho(x, t) dV. \quad (3.2.4)$$

The subscript  $\Omega$  in Eq. 3.2.4 indicates that the integral is defined with respect to the control volume, and  $dV$  represents a differential element of the system volume. Eq. 3.2.4 is modified when heterogeneity in properties is introduced, it turns out that mass does not vary as a function of space, given that it was initially mentioned that  $\Omega$  it is a fixed control volume, and the mass in Eq. 3.2.4 represents that of the entire system. In conclusion, mass only varies as a function of time. Taking this into account, it can be concluded that:

$$m(t) = \int_{\Omega} \rho(x, t) dV. \quad (3.2.5)$$

It can be observed that in Eq. 3.2.5 porosity is not involved, because this equation serves to model the fluid, the movable solid, and the fixed solid.

### 3.2.2 Mass flow

The fluid and the movable solids will flow through the porous medium, with fluid and movable solid entering and leaving over a certain time interval. Therefore, it is important to quantify how much mass enters and leaves through the boundaries of the control volume. Considering that the fluid and the movable solids travel at a certain velocity ( $v$ ) through a certain area ( $A$ ), we can obtain:

$$F_m = \rho v A. \quad (3.2.6)$$

In Eq. 3.2.6,  $F_m$  refers to the mass flux and is represented as a scalar quantity, which is not general in a flow system. In a flow system, velocity is represented as a vector quantity and the area is a plane through which the mass flux passes. If one wants to quantify the amount of mass passing through this plane, a coordinate system must first be established as shown in Fig. 3.3, where the plane is aligned with the  $y$  and  $z$ -axes. In this configuration, the velocity vector manifests only in the  $x$  direction and aligns with the positive direction opposite to the  $x$ -axis. Therefore, the correct expression would be:

$$F_m = -\rho(\vec{v} \cdot \vec{i})A_p = -\rho v_x A_p. \quad (3.2.7)$$

The difference between Eqs. 3.2.6 and 3.2.7 lies in the fact that in Eq. 3.2.7 the velocity variable is formulated in a vectorial form. However, it is important to note that in this case it is assumed that the plane through which the mass flux passes is perpendicular to the  $x$ -axis. This may not always be correct, as the plane can have any arbitrary shape. Therefore, if one wants to calculate the mass flux, the velocity vector must be decomposed into directions different from the one in this case. If we consider that the projection of the velocity vector  $\vec{v}$ , which passes through an area perpendicular ( $A_p$ ), with respect to the normal is obtained with the dot product between them, we get:

$$F_m = -\rho(\vec{v} \cdot \vec{n})A_p. \quad (3.2.8)$$

Equation (3.2.8) states that the velocity vector shown in **Fig. 3.3** can enter in any direction, and by projecting the dot product of the normal vector ( $\vec{n}$ ), the final value of the velocity vector with respect to the YZ plane will be obtained. Additionally, to adjust the direction, a negative sign is introduced to indicate that Eq. 3.2.8 refers to a flow going from outside to inside. Therefore, the normal vector outward and  $-\vec{n}$  points inward. Dividing the surface of the plane into  $N$  elements of small areas where the flux is calculated through each element, Eq. 3.2.8 transforms into:

$$F_{mi} = -(\vec{v}_i \cdot \vec{n}_i)\rho_i A_{pi} \text{ for } i=1, 2, N$$

Since this equation will model the total flux, the fluxes of each subdivision of elements are summed in  $\partial\Omega$  and the net flux is calculated as:

$$F_m = \sum_{i=1}^N F_{mi} = \sum_{i=1}^N -(\vec{v}_i \cdot \vec{n}_i)\rho_i A_{pi}. \quad (3.2.9)$$

Therefore, assuming the sum of the limit of elements to calculate the net flux, we have:

$$F_m = \lim_{N \rightarrow \infty} \sum_{i=1}^N F_{mi} = \lim_{N \rightarrow \infty} \sum_{i=1}^N -(\vec{v}_i \cdot \vec{n}_i)\rho_i A_{pi}. \quad (3.2.10)$$

Since we are discussing the total flux of the system, it only varies with respect to time, and equation (3.2.10) becomes:

$$F_m(t) = - \int_{\partial\Omega} \rho(\vec{v} \cdot \vec{n})dA_p. \quad (3.2.11)$$

Eq. 3.2.11 expresses the mass flux through the surface  $\partial\Omega$  of a control volume  $\Omega$  at a certain time  $t$ . It is important to consider that  $\vec{v}$  refers to the velocity of the fluid considering the entire plane. Therefore, when it is necessary to know the velocity through porous media, it is essential to take porosity into account and convert it to Darcy velocity.

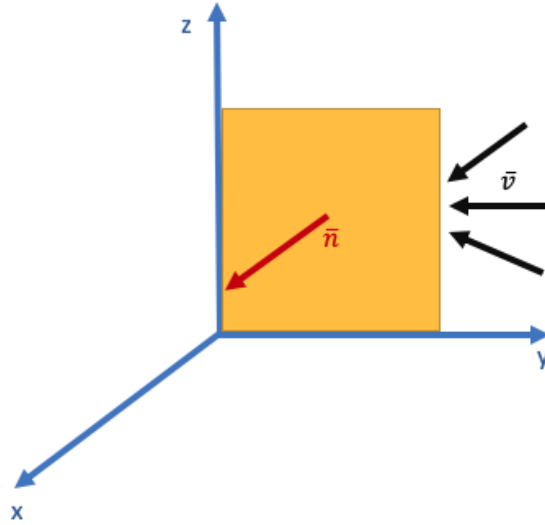


**Figure 3. 3** Vector Flow through a YZ Plane.  
(Téllez, 2021)

### 3.2.3 Source and/or Sink Term

In the previous subsection, an equation representing the mass flux was obtained, but it does not yet address the problem of solids production, as it does not calculate the movable solids generated from the rock matrix. These movable solids lose cohesion strength as erosion and porosity increase. This suggests that a certain amount of mass must appear over time as an injected volume of solids, while at the same time, an amount of rock matrix (fixed) is eroded. The parameter that addresses this phenomenon is the source/sink term, which considers the external mass flux of the system and includes the generation and production of movable solids ( $p$ ). This term is defined as follows:

$$q_m = pq. \quad (3. 2. 12)$$

Eq. 3.2.12 describes the amount of mass entering a system, but it does not explicitly specify that the system into which it will be injected or from which it will be produced is the control volume  $\Omega$ . Therefore, the  $\bar{q}$  is introduced, which characterizes the amount of volume produced from fluid or movable solids per unit of time and unit of rock volume (control volume). This variable allows Eq. 3.2.12 to explicitly relate to the control volume system  $\Omega$ , and thus we obtain:

$$q_m = \int_{\Omega} p\bar{q}dV. \quad (3. 2. 13)$$

Eq. 3.2.13 only varies with respect to time, as spatially it represents the entire control volume, which is fixed:

$$q_m(t) = \int_{\Omega} p\bar{q}dV. \quad (3.2.14)$$

### 3.2.4 Integral Form of Mass Conservation

The control volume will be analyzed  $\Omega$  over a certain time range  $[t_0, t]$ , where  $t_0$  is constant and  $t$  variable. The mass at a certain moment in time is represented by Eq. 3.2.5, so  $m(t) - m(t_0)$  determines the change in mass over a time range. The amount of mass entering at an instant is:

$$F_m(t) = - \int_{\partial\Omega} \rho(v \cdot \bar{n})dA_p. \quad (3.2.15)$$

Since the goal is to determine the amount of mass that has entered the control volume over the time range  $[t_0, t]$  and considering that during this time range the mass flux remained constant, the total amount of mass that has entered the system is as follows:

$$m(t) - m(t_0) = (t - t_0) \cdot F_m. \quad (3.2.16)$$

In the case of variable mass flux, the range of  $[t_0, t]$  into  $N$  intervals, the number of which will depend on the duration of the different fluxes, and summing the total, we get the following:

$$\sum_{i=1}^N F_m(t_i)(t_i - t_{i-1}). \quad (3.2.17)$$

Approximating the sum of  $N$  intervals to infinity ( $N \rightarrow \infty$ ) we obtain:

$$m(t) - m(t_0) = \int_{t_0}^t F_m(T)dT. \quad (3.2.18)$$

The equation only includes the mass flux of the mixture that exists in the porous medium, but it lacks the additional flux term in the system. Adjusting Eqs. 3.2.18 and 3.2.14, the following expression is obtained:

$$m(t) - m(t_0) = \int_{t_0}^t F_m(T)dT + \int_{t_0}^t q_m(T)dT. \quad (3.2.19)$$

Substituting the definitions of each variable, or Eqs. 3.2.5, 3.2.11, and 3.2.14, and isolating the term on the left side that includes the initial time, we obtain:

$$\int_{\Omega} \rho(x, t) dV = \int_{\Omega} \rho(x, t_0) dV + \int_{t_0}^t \int_{\Omega} \rho(x, T) \bar{q}(x, T) dV dT - \int_{t_0}^t \int_{\Omega} \rho(x, T) (v(x, T) \cdot \bar{n}(x)) dA_p dT. \quad (3.2.20)$$

Eq. 3.2.20 explicitly expresses the dependence of the variables with respect to distance and time. In this equation, the amount of mass at different times is calculated, considering the amount of mass that enters due to the flow of fluids and movable solids in the reservoir, as well as the amount of mass that enters due to the source term.

### 3.2.5 Differential Form of Mass Conservation

To discretize in finite differences and develop the mathematical model of the simulator, it is necessary to obtain equations in their differential form. Eq. 3.2.20 is in its integral form, but by deriving it with respect to the dependent variables, its differential form can be obtained. This process involves applying the Fundamental Theorem of Calculus and the appropriate differentiation rules to obtain the partial derivatives of the equation with respect to the dependent variables. Once these derivatives are obtained, they can be discretized using finite difference methods to approximate the solution to the problem numerically. For the mass terms, we obtain:

$$\frac{d}{dt} m(t_0) = 0, \quad (3.2.21)$$

$$\frac{d}{dt} m(t) = \frac{d}{dt} \int_{\Omega} \rho(x, t) dV = \int_{\Omega} \frac{\partial}{\partial t} (\rho(x, t)) dV. \quad (3.2.22)$$

For the mass flux integrals and the source term, the Fundamental Theorem of Calculus will be applied:

$$f(t) = \frac{d}{dt} \int_{t_0}^t f(T) dT. \quad (3.2.23)$$

Applying Eq. 3.2.23 to 3.2.11 and 3.2.14:

$$\frac{d}{dt} \int_{t_0}^t F_m(T) dT = F_m(t), \quad (3.2.24)$$

$$\frac{d}{dt} \int_{t_0}^t q_m(T) dT = q_m(t). \quad (3.2.25)$$

The material balance equation in its differential form is:

$$\frac{d}{dt}m(t) = F_m(t) + q_m(t). \quad (3.2.26)$$

Eq. 3.2.26 can be written explicitly as follows:

$$\int_{\Omega} \frac{\partial}{\partial t}(\rho(x, t))dV = \int_{\Omega} \rho(x, T)\bar{q}(x, T)dV - \int_{\Omega} \rho(x, T)(v(x, T) \cdot \bar{n}(x))dA_p. \quad (3.2.27)$$

It can be observed that Eq. 3.2.2 operates through volume and surface integrals. To homogenize the surface terms to volume, Gauss's Theorem, also known as the Divergence Theorem, is used. This theorem relates the flux of a vector field through a closed surface to the integral of its divergence over the volume bounded by that surface. Mathematically, Gauss's Theorem is expressed as follows:

$$\iint_{\partial\Omega} F \cdot \bar{n}dA = \iiint_{\Omega} \nabla \cdot FdV. \quad (3.2.28)$$

Using Eq. 3.2.27 for the mass flux term, we obtain:

$$\int_{\partial\Omega} \rho(x, T)(\bar{u}(x, T) \cdot \bar{n}(x))dA_p = \int_{\Omega} \nabla \cdot (\rho(x, T)(v(x, T)))dV. \quad (3.2.29)$$

Substituting Eq. 3.2.29 into Eq. 3.2.27 and rearranging it, we obtain:

$$\int_{\Omega} \frac{\partial}{\partial t}(\rho(x, t))dV - \int_{\Omega} \rho(x, T)\bar{q}(x, T)dV + \int_{\Omega} \nabla \cdot (\rho(x, T)(v(x, T)))dV = 0. \quad (3.2.30)$$

or

$$\int_{\Omega} \left( \frac{\partial}{\partial t}(\rho(x, t)) - \rho(x, T)\bar{q}(x, T) + \nabla \cdot (\rho(x, T)(\bar{v}(x, T))) \right) dV = 0. \quad (3.2.31)$$

Eq. 3.2.31 demonstrates that, regardless of the shape, size, and position of the control volume the integral must be zero, thus the integrand must be exactly zero. Therefore, we can remove the volume integral as follows:

$$\frac{\partial}{\partial t}(\rho(x, t)) = \rho(x, T)\bar{q}(x, T) - \nabla \cdot (\rho(x, T)\bar{v}(x, T)). \quad (3.2.32)$$

Eq. 3.2.32 expresses mass conservation in its differential form and is the equation that will be used as the basis for deriving the following sections. It is important to remember that this equation not only models the flow of fluids and movable solids but also the behavior of the

solid itself. In the next section, additional considerations will be made to adapt Eq. 3.2.32 to obtain equations that describe the general behavior of the solids production phenomenon.

It is important to note that Eq. 3.2.32 is weaker than Eq. 3.2.20 because in the differential form we need functions to be at least differentiable meanwhile the integral form requires integrability. For example, discontinuous functions can be integrated but their derivative is undefined at the discontinuities. If the properties of the medium, such as porosity and density, are heterogeneous with abrupt changes, then the differential equation may cease to make sense. Consequently, in the simulator that is going to be developed, it is proposed that the medium be initially homogeneous and that changes in properties are not abrupt.

### 3.2.6 Material Balance Equation of the Phases

In this section, the mass equation for the solid, fluid, and movable solids will be developed using Eq. 3.2.32 and considering that:

$$\rho(x, t) = (1 - \phi)\rho_s. \quad (3. 2. 33)$$

It is considered that the porosity ( $\phi$ ) is dependent on space and time, just like density. If Eq.3.2.33 is substituted into Eq. 3.2.32, we obtain the following:

$$\frac{\partial}{\partial t}(\rho_s(1 - \phi)) = \rho_s\bar{q} - \nabla \cdot (\rho_s(1 - \phi)(\bar{v}_x)). \quad (3. 2. 34)$$

From Eq. 3.2.34, it can be observed that the density and porosity variables vary with respect to distance and time, and these are substituted only in the mass flux terms as a function of time. Considering that the velocity of the solid ( $\bar{v}_x$ ) is zero, Eq. 3.1.3 can be substituted into Eq. 3.2.34, and thus we obtain:

$$\frac{\partial}{\partial t}(\rho_s(1 - \phi)) = \rho_s\bar{q}. \quad (3. 2. 35)$$

In the phenomenon of solids production, movable solids are generated when the rock matrix loses cohesion and solid begins to detach from this medium. Therefore, Eq. 3.2.35 indicates that the fixed rock matrix will be losing solid and producing movable solids. The parameter  $\bar{q}$  represents the volume of solid that the matrix loses per unit of time. Mathematically, the right side of Eq. 3.2.35 becomes negative because it is desired that  $\bar{q}$  be a positive quantity that determines the losses of solids, and this lost part will appear in the system of movable solids:

$$\frac{\partial}{\partial t}(\rho_s(1 - \phi)) = -\rho_s\bar{q}. \quad (3. 2. 36)$$

Considering that  $\rho_s$  is constant over time:

$$\frac{\partial}{\partial t}((1 - \phi)) = -\bar{q}, \quad (3.2.37)$$

$$\frac{\partial \phi}{\partial t} = \bar{q}. \quad (3.2.38)$$

From now on, it will be considered that:

$$F_m = \bar{q}\rho_s. \quad (3.2.39)$$

Eq. 3.2.39 refers to the amount of mass that the matrix loses in a unit of time per unit volume. Combining Eqs. 3.2.38 and 3.2.39:

$$\frac{\partial \phi}{\partial t} = \frac{F_m}{\rho_s}. \quad (3.2.40)$$

Eq. 3.2.40 represents the continuity equation of the solid, which determines the change in porosity concerning time when the rock is eroding due to mass flow. With the equation governing the solid, the aim is to obtain the equation for movable solids. For this equation, density is considered, which is the mass of the movable solids per unit volume of the rock.

$$\rho_2 = c\phi\rho_{fs} = c\phi\rho_s. \quad (3.2.41)$$

Eq. 3.2.41 defines the density of the movable solid. Substituting Eq. 3.2.41 into Eq. 3.2.32, we obtain the following:

$$\frac{\partial}{\partial t}(c\rho_s\phi) = \rho_s\bar{q} - \nabla \cdot (c\rho_s\phi(\bar{v}_x)). \quad (3.2.42)$$

Eq. 3.2.42 considers that density and porosity vary with respect to distance and time. The sink/source term is considered positive since the solid detaching from the rock matrix is accumulating in the control volume.

$$\frac{\partial}{\partial t}(c\rho_s\phi) + \nabla \cdot (c\rho_s\phi(\bar{v}_x)) = F_m, \quad (3.2.43)$$

$$\frac{\partial(c\phi)}{\partial t} + \nabla \cdot (c\phi\bar{v}_x) = \frac{F_m}{\rho_s}. \quad (3.2.44)$$

It is observed that the unit of  $\bar{v}_x$  refers to the interstitial velocity or the fluid flow within the rock. This term is not defined through a porous medium, so it needs to be transformed into Darcy velocity with the following relationship:

$$\bar{v}_x = \frac{v_D}{\phi}. \quad (3.2.45)$$

Substituting Eq. 3.2.45 into Eq. 3.2.44 we obtain the following:

$$\frac{\partial(c\phi)}{\partial t} + \nabla \cdot (cv_D) = \frac{F_m}{\rho_s}. \quad (3.2.46)$$

Eq. 3.2.46 establishes the relationship between the flow of movable solids, the degradation of porosity over time, and the amount of solid produced in the system due to the solids detaching from the rock. If Eqs. 3.2.46 and 3.2.40 are combined, we obtain:

$$\frac{\partial(c\phi)}{\partial t} + \nabla \cdot (cv_D) = \frac{\partial\phi}{\partial t}. \quad (3.2.47)$$

To describe the fluid, the definition of fluid mass per unit volume of rock is used, and the following definition of density is considered:

$$\rho_3 = (1 - c)\phi\rho_f. \quad (3.2.48)$$

Eq. 3.2.48 represents the density of the fluid that will be in the fluid flow through the porous medium. Substituting Eq. 3.2.48 into Eq. 3.2.32, we obtain:

$$\frac{\partial}{\partial t} \left( (1 - c)\rho_f\phi \right) = \rho_f\bar{q} - \nabla \cdot \left( (1 - c)\rho_f\phi(\bar{v}_x) \right). \quad (3.2.49)$$

The sink/source term will be removed from Eq. 3.2.49, so Eq. 3.2.49 transforms to:

$$\frac{\partial}{\partial t} \left( (1 - c)\rho_f\phi \right) = -\nabla \cdot \left( (1 - c)\rho_f\phi(\bar{v}_x) \right). \quad (3.2.50)$$

Substituting interstitial velocity with its relationship to Darcy velocity, we obtain:

$$\frac{\partial}{\partial t} \left( (1 - c)\rho_f\phi \right) = -\nabla \cdot \left( (1 - c)\rho_f v_D \right). \quad (3.2.51)$$

If the density of the fluid ( $\rho_f$ ) is constant:

$$\frac{\partial}{\partial t}((1-c)\phi) = -\nabla \cdot ((1-c)v_D). \quad (3.2.52)$$

Combining Eqs. 3.2.47 and 3.2.52, the following equation is obtained:

$$\frac{\partial}{\partial t}((1-c)\phi) + \nabla \cdot ((1-c)v_D) + \frac{\partial(c\phi)}{\partial t} + \nabla \cdot (cv_D) = \frac{\partial\phi}{\partial t}. \quad (3.2.53)$$

Reducing Eq. 3.2.53:

$$\nabla \cdot v_D = 0. \quad (3.2.54)$$

Eq. 3.2.54 is the continuity equation that refers to the fluid flow through the porous medium, where  $\bar{q}$  is equivalent to Darcy's velocity ( $v_D$ ). This equation requires Darcy's Law to obtain the physical parameters for the flow through the porous medium and to define the pressure explicitly. Eqs. 3.2.40, 3.2.47, and 3.2.54 constitute the set of mass balance equations for the proposed problem. These equations are not sufficient to solve the problem, as a term representing the generation of solids and the rate at which solid is being introduced into the mixture is needed. This term is obtained in the following section.

### 3.3 Constitutive Law of Mass Generation

H. A. Einstein conducted extensive theoretical and experimental studies related to the filtration of non-colloidal particles in porous media. For the problem under analysis, a constitutive law is needed to describe the rate of mass eroded from the rock matrix and the rate at which new movable solids enter the mixture in the flow of the porous medium. This constitutive law is fundamental for understanding and adequately modeling the behavior of the system under study.

$$\dot{m}_{er} = \lambda' \|m_i^{fs}\|. \quad (3.3.1)$$

where  $\dot{m}_{er} = F_m$

Eq. 3.3.1 shows that the erosion phenomenon is governed by the flow of the movable solids ( $m_i^{fs}$ ). If this parameter increases, then erosion increases due to the kinetic forces in the system. The other variable that affects Eq. 3.3.1 is the ratio ( $\lambda'$ ), which relates to spatial frequency of the erosion potential. This coefficient reflects the frequency of points with erosion potential in the system; therefore, if the coefficient increases, the rock becomes weaker. The coefficient has dimensions of inverse length  $\lambda' = [L^{-1}]$ .

In the coupling of the erosion process and the rock's geomechanics,  $\lambda'$  is expected to increase as a function of rock damage or when there is an increase in porosity, which is implicitly related inversely to cohesion. (Vardoulakis, Stavropoulou, & Papanastasiou, 1996) They mention that the erosion process will be more active in intact zones (characterized by small pore channels), so they assume that:

$$\lambda' = \lambda(1 - \phi). \quad (3.3.2)$$

The variable  $\|m_i^{fs}\|$  refers to the norm of the mass velocity of the movable solid, which represents the magnitude of the mass velocity vector. This variable is represented as:

$$m_i^{fs} = \rho_s \bar{c} v_D. \quad (3.3.3)$$

Combining Eqs. 3.3.1, 3.3.2, and 3.3.3, the mass flux is obtained:

$$\dot{m}_{er} = \lambda(1 - \phi) \|\rho_s \bar{c} v_D\|. \quad (3.3.4)$$

Because  $\rho_s$  and  $c$  are scalar variables, Eq. 3.3.4 converts to:

$$\dot{m}_{er} = \lambda(1 - \phi) \rho_s \bar{c} \|v_D\|. \quad (3.3.5)$$

Eq. 3.3.5 offers an intuitive interpretation of the erosion phenomenon. It indicates that the rate of erosion is proportional to the concentration of movable solids in the system, to the coefficient  $\lambda$  which represents the frequency of erosion potential, and to Darcy's velocity present in the system. As for  $(1 - \phi)$ , the equation indicates that if there is porosity, the erosion process will occur in the system. If porosity is 1 (there is no rock in the system), the equation becomes zero, indicating that there will no longer be any erosion potential.

The counterpart of Eq. 3.3.5 is the term  $\bar{c}$ , which lacks physical meaning when the balance between erosion and deposition of movable solids is not considered. This means that a critical concentration of movable solids is required, at which these solids deposit and clog the pore space. This balance is obtained as follows:

$$\bar{c} = c - \frac{c^2}{c_{cr}}. \quad (3.3.6)$$

Eq. 3.3.36 represents the concentration at which the balance between deposition and erosion is found. When  $c$  and  $c_r$  have the same value, Eq. 3.3.6 will give a value of zero, which will indicate that the porous medium is clogged by the movable solids and, therefore, new solids cannot be generated until the concentration value decreases. This depends on the petrophysical properties of the rock, such as porosity, permeability, or rock fabric. By substituting Eq. 3.3.6 into 3.3.5, we obtain:

$$\dot{m}_{er} = \lambda(1 - \phi)\rho_s \left( c - \frac{c^2}{c_{cr}} \right) \|v_D\| = F_m. \quad (3.3.7)$$

By combining Eq. 3.3.7 with 3.2.40, the following equation is obtained:

$$\frac{\partial \phi}{\partial t} = \lambda(1 - \phi) \left( c - \frac{c^2}{c_{cr}} \right) \|v_D\|. \quad (3.3.8)$$

### 3.4 Darcy's Law

Darcy's law is used to describe the flow of fluids through porous media. This law was established by Henry Philibert Darcy in 1856 when he was studying the flow of water through a sand pack. Later, Muskat (1931) adapted Darcy's law for the oil industry, allowing the modeling of oil flow. Darcy's law establishes a proportional relationship between the flow rate ( $q$ ) through a porous medium of a certain permeability ( $k$ ), the dynamic viscosity of the fluid ( $\mu$ ), and the pressure drop ( $\frac{dp}{dl}$ ) along a homogeneous medium.

$$q = -\frac{kA dp}{\mu dl}. \quad (3.4.1)$$

Eq. 3.4.1 has a negative sign because the fluid flows from the high-pressure zone to the low-pressure zone. This equation does not consider gravitational effects. Since it is necessary to know Darcy's velocity ( $v_D$ ) and the previous equation is in terms of flow rate ( $q$ ), therefore equation (3.4.1) will be divided by the area ( $A$ ):

$$v_D = -\frac{k dp}{\mu dl}. \quad (3.4.2)$$

Changes in porosity due to the phenomenon of formation collapse affect the system's permeability. Therefore, it is necessary to relate permeability to porosity, so that each time porosity changes, permeability changes simultaneously.

One aspect to consider in Eq. 3.4.2 is that dynamic viscosity does not consider the density of the mixture and, therefore, does not calculate the variation as the concentration of movable solids changes. Due to this, the variable is modified by introducing the concept of kinematic viscosity through Eq. 3.1.9, which is of high importance in the study of solids production. Kinematic viscosity is defined as follows:

$$\eta_k = \frac{\mu}{\bar{\rho}}. \quad (3.4.3)$$

Eq. 3.4.3 describes kinematic viscosity, which represents the resistance of a fluid to flow when there are no external forces other than gravity and likewise considers the density of the mixture ( $\bar{\rho}$ ). Substituting Eq. 3.4.3 into 3.4.2 we obtain:

$$v_D = -\frac{k dp}{\eta_k \bar{\rho} dl}. \quad (3.4.4)$$

Substituting Eq. 3.1.9 into Eq. 3.4.4, we obtain the following equation:

$$v_D = -\frac{k dp}{\eta_k((1-c)\rho_f + c\rho_s) dl}. \quad (3.4.5)$$

### 3.5 Kozeny-Carman Equation

In this section, we will discuss an equation that considers the modification of permeability so that the variable included in Eq. 3.4.5 changes with porosity. If porosity increases, it is more likely that there will be more flow channels, and the permeability value will increase. The mathematical relationship that relates the change in permeability with porosity is the Kozeny-Carman equation:

$$k = k_0 \frac{\phi^3}{(1-\phi)^2}. \quad (3.5.1)$$

Where  $k_0$  is a constant that represents the initial permeability.

### 3.6 Continuity Equation

Eqs. 3.2.47 and 3.3.8 are considered, where the first models the mass balance between the concentration of solids and the effect that porosity has, and the second models the change in porosity with respect to time. Additionally, Eqs. 3.4.5 and 3.5.1 are considered, which models the fluid flow and the variation of permeability in relation to porosity. However, an equation that describes the relationship between all these equations and models the fluid flow and the movable solids is needed. To achieve this, Eqs. 3.4.5 and 3.5.1 will be combined:

$$v_D = -\frac{k_0 \phi^3}{(1-\phi)^2 [\eta_k((1-c)\rho_f + c\rho_s)]} \frac{dp}{dr}. \quad (3.6.1)$$

Substituting Eq. 3.6.1 into Eq. 3.2.54:

$$\frac{\partial^2 p}{\partial r^2} + \frac{\partial p}{\partial r} \left[ \frac{1}{r} + \alpha_c \frac{\partial \phi}{\partial r} + \beta_c \frac{\partial c}{\partial r} \right] = 0. \quad (3.6.2)$$

where:

$$\alpha_c = \frac{3 - \phi}{\phi(1 - \phi)}, \beta_c = -\frac{\rho_s - \rho_f}{(1 - c)\rho_f + c\rho_s}$$

### 3.7 Borehole stresses, deformation and failure

To understand the effect generated by local stresses near the well, it is necessary to create a mechanical model that calculates the moment when the rock will collapse. For this problem, an axisymmetric deformation analysis in the plane is considered, as shown in Fig 3.4. The regional stresses are transformed into three new local stresses: radial stress ( $\sigma_r$ ), tangential stress ( $\sigma_\theta$ ) and axial stress ( $\sigma_a$ ). For the proposed simulator, which is one-dimensional, the axial stress will not influence the numerical value. Under these conditions, the deformations are expressed only in terms of radial displacement  $u_r = u(r, t)$ , therefore:

$$\varepsilon_r = \frac{\partial u}{\partial r}, \quad (3.7.1)$$

$$\varepsilon_\theta = \frac{u}{r}. \quad (3.7.2)$$

Considering Eqs. 2.4.42, 2.4.55, and 2.4.75, the elastic constitutive relationships between stress and total strain are obtained:

$$\sigma_r = \frac{\bar{E}(1-\phi)}{(1+\nu)(1-2\nu)} [(1-\nu)\varepsilon_r + \nu\varepsilon_\theta], \quad (3.7.3)$$

$$\sigma_\theta = \frac{\bar{E}(1-\phi)}{(1+\nu)(1-2\nu)} [(1-\nu)\varepsilon_\theta + \nu\varepsilon_r]. \quad (3.7.4)$$

Where the equilibrium Eq. 2.4.6 in an axisymmetric plane transforms to:

$$\frac{\partial \sigma_r}{\partial r} + \frac{\sigma_r - \sigma_\theta}{r} = 0. \quad (3.7.5)$$

Substituting Eqs. 3.7.1 - 3.7.4 into Eq. 3.7.5, we obtain the following:

$$\frac{\partial^2 u}{\partial r^2} + g_1 \frac{\partial u}{\partial r} - g_2 u = g_3 \frac{\partial(\phi p)}{\partial r}. \quad (3.7.6)$$

where:

$$g_1(r) = \frac{1}{r} - \frac{1}{1-\phi} \frac{\partial \phi}{\partial r}, \quad (3.7.7)$$

$$g_2(r) = \frac{1}{r^2} + \frac{1}{r} \frac{v}{1-v} \frac{1}{1-\phi} \frac{\partial \phi}{\partial r}. \quad (3.7.8)$$

$$g_3(r) = \frac{(1+v)(1-2v)}{\bar{E}(1-\phi)(1-v)}. \quad (3.7.9)$$

Eq. 3.7.6 describes the behavior of displacement as the variables of porosity, concentration, pressure, and geomechanical properties change. Knowing the behavior of displacement will help determine the behavior of effective stress and thereby calculate when the rock will collapse.

# 4. Simulator Model

## 4.1 Introduction

A cylindrical structure is considered for the development of the simulation model, as shown in Fig. 4.1. This model contemplates the flow in the radial direction towards the well, an isotropic reservoir with constant thickness, and a vertical cylindrical well located in the center, which will produce at a constant pressure. The simulator is based on the following principles:

1. Hydromechanical Model. - This consists of the mass balance equation and the porosity evolution equation governing erosion. The first equation describes the behavior of the concentration variable ( $c$ ), while the second describes the behavior of the porosity variable ( $\phi$ ).
2. Darcy's Law. - It describes the flow movement through a porous medium where the porosity is variable. As the effective porosity increases, the permeability also increases. Consequently, Darcy's Law was coupled with the Kozeny-Carman equation to relate the change in permeability concerning porosity.
3. Continuity Equation. This equation integrates all the changes and interactions of the variables of porosity, concentration, and pressure to calculate the flow of the mixture.
4. Geomechanical Equation. - This equation integrates the variables of porosity and cohesion with geomechanical parameters. The decrease in cohesion due to increased porosity is considered to predict rock collapse using the Mohr-Coulomb criterion.

With the four characteristics combined, a numerical simulation is conducted in which the primary variables, such as porosity, concentration, pressure, and displacement, change with time and space. The effect of mechanical damage is implicitly incorporated, using the values of effective stress to predict the mechanical failure of the rock and the near-well collapse.

Radial Displacement ( $u_r$ ) is determined by numerically solving the differential Eq. 3.7.6 with the boundary conditions presented in this chapter. Once the variables  $u$  and  $\frac{\partial u}{\partial r}$  are determined, the stress is calculated by substituting the results into Eqs. 3.7.3 and 3.7.4. Due to the lack of dependence of Eqs. 4.2.1, 4.2.2, and 4.2.3 on the variable  $u$ , it is possible to solve for the variable in parallel over the same time interval.

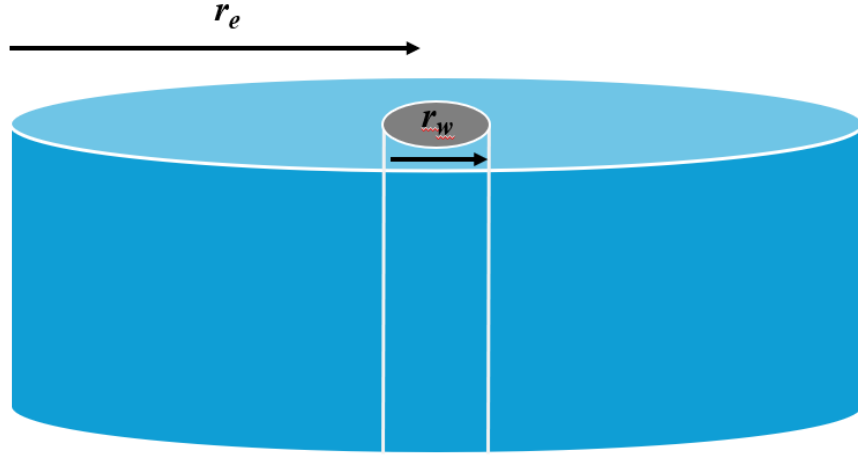


**Figure 4. 1** Cylindrical Model of the Simulator

## 4.2 Simulator Equations

As mentioned earlier, this simulator is based on four fundamental principles, which are described in the following equations:

$$\frac{\partial(c\phi)}{\partial t} + v_D \frac{\partial c}{\partial r} = \frac{\partial \phi}{\partial t}, \quad (4. 2. 1)$$

$$\frac{\partial \phi}{\partial t} = \lambda(1 - \phi) \left( c - \frac{c^2}{c_{cr}} \right) \|v_D\|. \quad (4. 2. 2)$$

In Eq. 4.2.1  $v_D$  comes out of the derivative because its divergence is 0 and Eq. 4.2.2 represent the equations of the hydromechanical model.

$$\frac{\partial^2 p}{\partial r^2} + \frac{\partial p}{\partial r} \left[ \frac{1}{r} + \alpha_c \frac{\partial \phi}{\partial r} + \beta_c \frac{\partial c}{\partial r} \right] = 0. \quad (4. 2. 3)$$

Eq. 4.2.3 represents the continuity equation for the flow of the mixture. Essentially, Eqs. 4.2.1, 4.2.2, and 4.2.3 represent the equations that model the phenomenon of solids production. However, it is important to note that they depend on the variable  $v_D$ , which can be represented as follows:

$$v_D = - \frac{k_0 \phi^3}{(1-\phi)^2 \eta_k [(1-c)\rho_f + c\rho_s]} \frac{\partial p}{\partial r}. \quad (4.2.4)$$

From Eqs. 4.2.1 - 4.2.4, the main variables are:  $c$ ,  $\phi$  and  $p$ ; while the other parameters are constants. The three mentioned variables change at each time step, making the equations nonlinear and consequently difficult to solve, where Eq. 4.2.4 is responsible for most of the nonlinearity among the equations.

#### 4.2.1 Initial and Boundary Conditions

Eqs. 4.2.1, 4.2.2, and 4.2.3 are differential equations with solutions for a continuous medium. However, for the simulator to provide a valid computational solution, this medium must be finite and have boundary conditions.

For an initial time ( $t_0$ ), it is considered that the rock-fluid system is in equilibrium. Therefore, the reservoir is at the same initial pressure ( $p_0$ ), and there is no fluid and solids flow ( $v_D = 0$ ). Additionally, it is assumed that there is an initial concentration ( $c$ ) of movable solids throughout the reservoir and that the porosity ( $\phi$ ) is homogeneous throughout the formation. A boundary condition with a constant external pressure is established at the reservoir's outer boundary. The initial and boundary conditions for the pressure are as follows:

$$p(r_w \leq r \leq r_e, t_0) = p_0, \quad (4.2.5)$$

$$p_e = p_{cte1}, \quad (4.2.6)$$

$$p_{wf} = p_{cte2}. \quad (4.2.7)$$

The initial and boundary conditions for porosity are:

$$\phi(r_w \leq r \leq r_e, t_0) = \phi_0, \quad (4.2.8)$$

$$\phi_e = \phi_0. \quad (4.2.9)$$

The initial and boundary conditions for concentration are:

$$c(r_w \leq r \leq r_e, t_0) = c_0, \quad (4.2.10)$$

$$c_c = c_0. \quad (4.2.11)$$

Eqs. 4.2.5 - 4.2.11 establish the necessary conditions to solve the solids production problem. These equations represent the initial and boundary conditions of the hydromechanical model. On the other hand, for the geomechanical model, the following boundary conditions are obtained:

$$\sigma_r(r_w, t) = -p_{wf}, \quad (4.2.12)$$

$$\sigma_r(r_e, t) = -\sigma_e. \quad (4.2.13)$$

where Eqs. 4.2.12 and 4.2.13 in terms of displacement become:

$$\left. \frac{\partial u}{\partial r} \right|_{r=r_w} = -\frac{v}{1-v} \frac{u(r_w)}{r_w} - g_3(r_w, t) [\phi(r_w, t)p_{wf} - p_{wf}], \quad (4.2.14)$$

$$\left. \frac{\partial u}{\partial r} \right|_{r=r_e} = -\frac{v}{1-v} \frac{u(r_e)}{r_e} + g_3(r_e, t) [\phi(r_e, t)p_e - \sigma_e]. \quad (4.2.15)$$

### 4.3 Finite Differences

The equations that describe the flow of the mixture of solids and fluids are in differential form and are nonlinear, making their analytical solution difficult. It is necessary to simplify these equations to consider all changes simultaneously in space and time. The variables  $c$ ,  $\phi$ ,  $p$  and  $u$  are the most relevant, so we will call them the main variables.

The finite difference method is based on approximating a continuous medium by a discrete medium. This transformation facilitates calculations, although it introduces an associated error due to the medium's discontinuity. It is crucial to divide this set of discrete spaces into a finite number of points throughout the reservoir. This set is called a mesh and will have an arrangement like the one shown in Fig. 4.2.

Essentially, the finite difference method replaces differential equations with sets of algebraic equations that relate the four main variables. Discretization is also applied to the displacement variable ( $u$ ), but in this case, the equation is discretized in parallel.

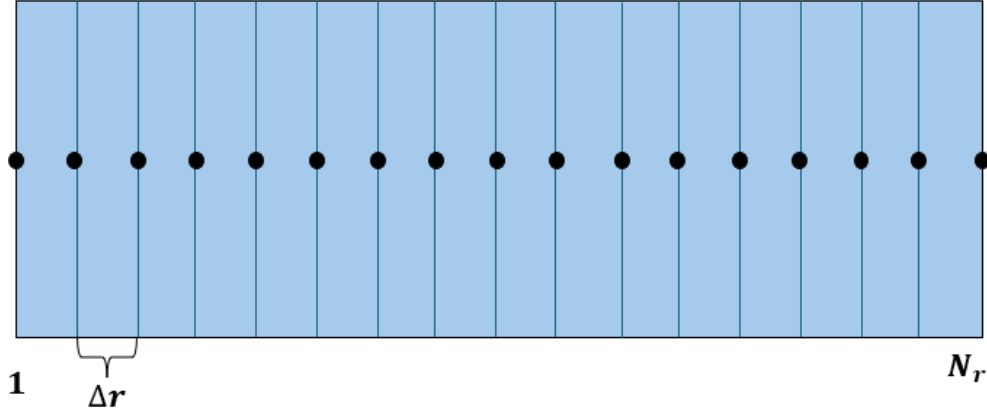


**Figure 4. 2** Spatially Discretized Mesh with Centered and Uniform Nodes.

### 4.3.1 Spatial Discretization

Spatial discretization approximates the derivatives that depend on space using a derivative approximation. For the first-order spatial derivative, a central scheme is used (**see Appendix A**). This approach is adopted because these terms are related to diffusion processes that act in all directions. The central scheme for the first order is formulated as follows:

$$\frac{df}{dx} \approx \frac{f_{i+1} - f_{i-1}}{2\Delta x}. \quad (4.3.1)$$

For a second-order central scheme, we obtain the following:

$$\frac{d^2y}{dx^2} \approx \frac{f_{i+1} - 2f_i + f_{i-1}}{\Delta x^2}. \quad (4.3.2)$$

When using Darcy's velocity, the first-order derivative is used and discretized in the central scheme:

$$\frac{df}{dx} \approx \frac{f_{i+1} - f_{i-1}}{2\Delta x}. \quad (4.3.3)$$

where  $f$  is the main variable,  $x$  represents the space, and  $i$  is the node where the main variable is located. In this case, the four main variables will be represented in the same way as  $f$ . It is important to remember the truncation error that exists in each scheme. Spatially discretizing Eqs. 4.2.1 - 4.2.4 and substituting 4.2.4 into 4.2.1, 4.2.2, and 4.2.3:

$$\frac{\partial(c_i\phi_i)}{\partial t} + \left( -\frac{k_0\phi_i^3}{(1-\phi_i)^2\eta_k[(1-c_i)\rho_f+c_i\rho_s]} \frac{p_{i+1}-p_{i-1}}{\Delta r_i} \right) \frac{c_{i+1}-c_{i-1}}{\Delta r_i} = \frac{\partial\phi_i}{\partial t}, \quad (4.3.4)$$

$$\frac{\partial \phi}{\partial t} = \lambda(1 - \phi_i) \left( c_i - \frac{c_i^2}{c_{cr_i}} \right) \left( \frac{k_0 \phi^3}{(1-\phi_i)^2 \eta_k [(1-c_i)\rho_f + c_i\rho_s]} \frac{p_{i+1} - p_{i-1}}{\Delta r_i} \right), \quad (4.3.5)$$

$$\begin{aligned} \frac{p_{i+1} - 2p_i + p_{i-1}}{\Delta r_i^2} + \frac{p_{i+1} - p_{i-1}}{2\Delta r_i} \left[ \frac{1}{r_i} + \left( \frac{3 - \phi_i}{\phi_i(1 - \phi_i)} \right) \frac{\phi_{i+1} - \phi_{i-1}}{2\Delta r_i} + \right. \\ \left. \left( \frac{\rho_f - \rho_s}{(1 - c_i)\rho_f + c_i\rho_s} \right) \frac{c_{i+1} - c_{i-1}}{2\Delta r_i} \right] = 0. \end{aligned} \quad (4.3.6)$$

where:

$$\Delta r_i = r_{i+1} - r_i$$

Eqs. 4.3.4 – 4.3.6 represent the spatially discretized equations.

### 4.3.2 Temporal Discretization

Temporal discretization is necessary because it makes the main variables present in the current time. The two ways to discretize an equation temporally are:

1. Explicit Method: This is when the variables are evaluated at the known time ( $n$ ), and the variable at the unknown time ( $n + 1$ ) in the temporal derivative.
2. Implicit Method: This is when the variables are evaluated at the unknown time ( $n + 1$ ), and the variable at the known time ( $n$ ) in the temporal derivative.

The explicit method is simpler because there will only be one unknown per variable, but this ease generates more errors due to instability. Due to this problem, the implicit method will be used as it is unconditionally stable (see **Appendix B**). The Time-Implicit method is described as follows:

$$y^{n+1} = y^n + f(t^{n+1}, y^{n+1})\Delta t \quad (4.3.7)$$

In equation (4.3.7),  $y$  represents the main variable,  $n$  the current time,  $n+1$  the next time,  $t$  the time, and  $\Delta t$  the time increment. Applying the implicit method to Eqs. 4.3.4 – 4.3.6:

$$\begin{aligned} \frac{c_i^{n+1}\phi_i^{n+1} - c_i^n\phi_i^n}{\Delta t} + \left( - \frac{k_0\phi_i^{n+1^3}}{(1-\phi_i^{n+1})^2 \eta_k [(1-c_i^{n+1})\rho_f + c_i^{n+1}\rho_s]} \frac{p_{i+1}^{n+1} - p_{i-1}^{n+1}}{\Delta r_i} \right) \frac{c_{i+1}^{n+1} - c_i^{n+1}}{\Delta r_i} = \\ \frac{\phi_i^{n+1} - \phi_i^n}{\Delta t}, \end{aligned} \quad (4.3.8)$$

$$\frac{\phi_i^{n+1} - \phi_i^n}{\Delta t} = \lambda(1 - \phi_i^{n+1}) \left( c_i^{n+1} - \frac{c_i^{n+1^2}}{c_{cr_i}} \right) \left( \frac{k_0 \phi_i^{n+1^3}}{(1 - \phi_i^{n+1})^2 \eta_k [(1 - c_i^{n+1}) \rho_f + c_i^{n+1} \rho_s]} \frac{p_{i+1}^{n+1} - p_i^{n+1}}{\Delta r_i} \right), \quad (4.3.9)$$

$$\frac{p_{i+1}^{n+1} - 2p_i^{n+1} + p_{i-1}^{n+1}}{\Delta r_i^2} + \frac{p_{i+1}^{n+1} - p_{i-1}^{n+1}}{2\Delta r_i} \left[ \frac{1}{r_i} + \left( \frac{3 - \phi_i^{n+1}}{\phi_i^{n+1} (1 - \phi_i^{n+1})} \right) \frac{\phi_{i+1}^{n+1} - \phi_{i-1}^{n+1}}{2\Delta r_i} + \left( \frac{\rho_f - \rho_s}{(1 - c_i^{n+1}) \rho_f + c_i^{n+1} \rho_s} \right) \frac{c_{i+1}^{n+1} - c_{i-1}^{n+1}}{2\Delta r_i} \right] = 0 \quad (4.3.10)$$

Eqs. 4.3.8 - 4.3.10 represent the equations for all internal nodes incorporated into the mesh; the boundary conditions will be applied to the external nodes.

## 4.4 Coupling of Boundary Conditions

Eqs. 4.3.8, 4.3.9, and 4.3.10 represent the equations to describe the solids production problem for internal nodes. For a specific simulation, boundary conditions are needed to provide a unique solution to the system of differential equations. These boundary conditions must be adapted to the mesh, as shown in Fig. 4.3. The system of discretized equations is divided into three groups: the initial node  $i=1$ , the internal nodes  $i=2, Nr-1$ , and the final node  $i=Nr$ . This also applies to equation (4.3.8):

$i = 1$

$$\frac{c_1^{n+1} \phi_1^{n+1} - c_1^n \phi_1^n}{\Delta t} + \left( - \frac{k_0 \phi_1^{n+1^3}}{(1 - \phi_1^{n+1})^2 \eta_k [(1 - c_1^{n+1}) \rho_f + c_1^{n+1} \rho_s]} \frac{p_2^{n+1} - p_1^{n+1}}{\Delta r_1} \right) \frac{c_2^{n+1} - c_1^{n+1}}{\Delta r_1} = \frac{\phi_1^{n+1} - \phi_1^n}{\Delta t}, \quad (4.4.1)$$

$i = 2, Nr - 1$

$$\frac{c_i^{n+1} \phi_i^{n+1} - c_i^n \phi_i^n}{\Delta t} + \left( - \frac{k_0 \phi_i^{n+1^3}}{(1 - \phi_i^{n+1})^2 \eta_k [(1 - c_i^{n+1}) \rho_f + c_i^{n+1} \rho_s]} \frac{p_{i+1}^{n+1} - p_i^{n+1}}{\Delta r_i} \right) \frac{c_{i+1}^{n+1} - c_i^{n+1}}{\Delta r_i} = \frac{\phi_i^{n+1} - \phi_i^n}{\Delta t}, \quad (4.4.2)$$

$i = Nr$

$$\frac{c_{Nr}^{n+1} \phi_{Nr}^{n+1} - c_{Nr}^n \phi_{Nr}^n}{\Delta t} + \left( - \frac{k_0 \phi_{Nr}^{n+1^3}}{(1 - \phi_{Nr}^{n+1})^2 \eta_k [(1 - c_{Nr}^{n+1}) \rho_f + c_{Nr}^{n+1} \rho_s]} \frac{p_{Nr+1}^{n+1} - p_{Nr}^{n+1}}{\Delta r_{Nr}} \right) \frac{c_{Nr+1}^{n+1} - c_{Nr}^{n+1}}{\Delta r_{Nr}} = \frac{\phi_{Nr}^{n+1} - \phi_{Nr}^n}{\Delta t}. \quad (4.4.3)$$

For Eq. 4.3.9, we obtain:

$i = 1$

$$\frac{\phi_1^{n+1} - \phi}{\Delta t} = \lambda(1 - \phi_1^{n+1}) \left( c_1^{n+1} - \frac{c_1^{n+1^2}}{c_{cr_1}} \right) \left( \frac{k_0 \phi_1^{n+1^3}}{(1 - \phi_1^{n+1})^2 \eta_k [(1 - c_1^{n+1}) \rho_f + c_1^{n+1} \rho_s]} \frac{p_2^{n+1} - p_1^{n+1}}{\Delta r_1} \right). \quad (4.4.4)$$

$i = 2, Nr - 1$

$$\frac{\phi_i^{n+1} - \phi_i^n}{\Delta t} = \lambda(1 - \phi_i^{n+1}) \left( c_i^{n+1} - \frac{c_i^{n+1^2}}{c_{cr_i}} \right) \left( \frac{k_0 \phi_i^{n+1^3}}{(1 - \phi_i^{n+1})^2 \eta_k [(1 - c_i^{n+1}) \rho_f + c_i^{n+1} \rho_s]} \frac{p_{i+1}^{n+1} - p_i^{n+1}}{\Delta r_i} \right). \quad (4.4.5)$$

$i = Nr$

$$\frac{\phi_{Nr}^{n+1} - \phi_{Nr}^n}{\Delta t} = \lambda(1 - \phi_{Nr}^{n+1}) \left( c_{Nr}^{n+1} - \frac{c_{Nr}^{n+1^2}}{c_{cr_{Nr}}} \right) \left( \frac{k_0 \phi_{Nr}^{n+1^3}}{(1 - \phi_{Nr}^{n+1})^2 \eta_k [(1 - c_{Nr}^{n+1}) \rho_f + c_{Nr}^{n+1} \rho_s]} \frac{p_{Nr+1}^{n+1} - p_{Nr}^{n+1}}{\Delta r_{Nr}} \right). \quad (4.4.6)$$

And finally with equation (4.3.10):

$i = 1$

$$\frac{p_2^{n+1} - 2p_1^{n+1} + p_0^{n+1}}{\Delta r_1^2} + \frac{p_2^{n+1} - p_0^{n+1}}{2\Delta r_1} \left[ \frac{1}{r_1} + \left( \frac{3 - \phi_1^{n+1}}{\phi_1^{n+1}(1 - \phi_1^{n+1})} \right) \frac{\phi_2^{n+1} - \phi_0^{n+1}}{2\Delta r_1} + \left( \frac{\rho_f - \rho_s}{(1 - c_1^{n+1}) \rho_f + c_1^{n+1} \rho_s} \right) \frac{c_2^{n+1} - c_0^{n+1}}{2\Delta r_1} \right] = 0, \quad (4.4.7)$$

$i = 2, Nr - 1$

$$\frac{p_{i+1}^{n+1} - 2p_i^{n+1} + p_{i-1}^{n+1}}{\Delta r_i^2} + \frac{p_{i+1}^{n+1} - p_{i-1}^{n+1}}{2\Delta r_i} \left[ \frac{1}{r_i} + \left( \frac{3 - \phi_i^{n+1}}{\phi_i^{n+1}(1 - \phi_i^{n+1})} \right) \frac{\phi_{i+1}^{n+1} - \phi_{i-1}^{n+1}}{2\Delta r_i} + \left( \frac{\rho_f - \rho_s}{(1 - c_i^{n+1}) \rho_f + c_i^{n+1} \rho_s} \right) \frac{c_{i+1}^{n+1} - c_{i-1}^{n+1}}{2\Delta r_i} \right] = 0, \quad (4.4.8)$$

$i = Nr$

$$\frac{p_{Nr+1}^{n+1} - 2p_{Nr}^{n+1} + p_{Nr-1}^{n+1}}{\Delta r_{Nr}^2} + \frac{p_{Nr+1}^{n+1} - p_{Nr-1}^{n+1}}{2\Delta r_{Nr}} \left[ \frac{1}{r_{Nr}} + \left( \frac{3 - \phi_{Nr}^{n+1}}{\phi_{Nr}^{n+1}(1 - \phi_{Nr}^{n+1})} \right) \frac{\phi_{Nr+1}^{n+1} - \phi_{Nr-1}^{n+1}}{2\Delta r_{Nr}} + \left( \frac{\rho_f - \rho_s}{(1 - c_{Nr}^{n+1}) \rho_f + c_{Nr}^{n+1} \rho_s} \right) \frac{c_{Nr+1}^{n+1} - c_{Nr-1}^{n+1}}{2\Delta r_{Nr}} \right] = 0. \quad (4.4.9)$$

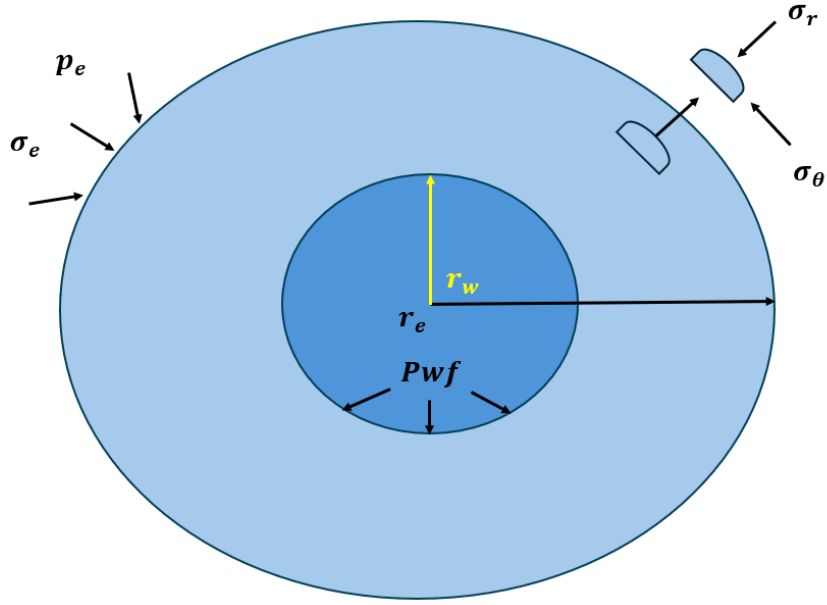


**Figure 4. 3** Simulator Configuration with Boundary Conditions.

In Eqs. 4.4.1 - 4.4.9, there are variables that correspond to nodes not defined in the mesh, such as the nodes labeled  $i=0$  or  $Nr + 1$ . Therefore, it is necessary to apply the boundary conditions and rewrite the equations that contain these variables. Applying the boundary conditions 4.2.5 - 4.2.11 to equations 4.4.1 - 4.4.9, we obtain the following:

$i = 1$

$$\frac{c_1^{n+1}\phi_1^{n+1} - c_1^n\phi_1^n}{\Delta t} + \left( -\frac{k_0\phi_1^{n+1^3}}{(1-\phi_1^{n+1})^2 \eta_k[(1-c_1^{n+1})\rho_f + c_1^{n+1}\rho_s]} \frac{p_2^{n+1} - p_1^{n+1}}{\Delta r_1} \right) \frac{c_2^{n+1} - c_1^{n+1}}{\Delta r_1} = \frac{\phi_1^{n+1} - \phi_1^n}{\Delta t}, \quad (4.4.10)$$

$i = Nr$

$$\frac{c_{Nr}^{n+1}\phi_{Nr}^{n+1} - c_{Nr}^n\phi_{Nr}^n}{\Delta t} + \left( -\frac{k_0\phi_{Nr}^{n+1^3}}{(1-\phi_{Nr}^{n+1})^2 \eta_k[(1-c_{Nr}^{n+1})\rho_f + c_{Nr}^{n+1}\rho_s]} \frac{p_{Nr+1}^{n+1} - p_{Nr}^{n+1}}{\Delta r_{Nr}} \right) \frac{c_{Nr+1}^{n+1} - c_{Nr}^{n+1}}{\Delta r_{Nr}} = \frac{\phi_{Nr}^{n+1} - \phi_{Nr}^n}{\Delta t}. \quad (4.4.11)$$

For equation (4.3.9), we obtain:

$i = 1$

$$\frac{\phi_1^{n+1} - \phi_1^n}{\Delta t} = \lambda(1 - \phi_1^{n+1}) \left( c_1^{n+1} - \frac{c_1^{n+1^2}}{c_{cr1}} \right) \left( \frac{k_0 \phi_1^{n+1^3}}{(1 - \phi_1^{n+1})^2 \eta_k [(1 - c_1^{n+1}) \rho_f + c_1^{n+1} \rho_s]} \frac{p_2^{n+1} - p_1^{n+1}}{\Delta r_1} \right), \quad (4.4.12)$$

$i = Nr$

$$\frac{\phi_{Nr}^{n+1} - \phi_{Nr}^n}{\Delta t} = \lambda(1 - \phi_{Nr}^{n+1}) \left( c_{Nr}^{n+1} - \frac{c_{Nr}^{n+1^2}}{c_{crNr}} \right) \left( \frac{k_0 \phi_{Nr}^{n+1^3}}{(1 - \phi_{Nr}^{n+1})^2 \eta_k [(1 - c_{Nr}^{n+1}) \rho_f + c_{Nr}^{n+1} \rho_s]} \frac{p_{Nr+1}^{n+1} - p_{Nr}^{n+1}}{\Delta r_{Nr}} \right). \quad (4.4.13)$$

And finally with equation (4.3.10)

$i = 1$

$$\frac{p_2^{n+1} - 2p_1^{n+1} + p_{wf}}{\Delta r_1^2} + \frac{p_2^{n+1} - p_{wf}}{2\Delta r_1} \left[ \frac{1}{r_1} + \left( \frac{3 - \phi_1^{n+1}}{\phi_1^{n+1} (1 - \phi_1^{n+1})} \right) \frac{\phi_2^{n+1} - 1}{2\Delta r_1} + \left( \frac{\rho_f - \rho_s}{(1 - c_1^{n+1}) \rho_f + c_1^{n+1} \rho_s} \right) \frac{c_2^{n+1} - c_1}{2\Delta r_1} \right] = 0, \quad (4.4.14)$$

$i = Nr$

$$\frac{p_e - 2p_{Nr}^{n+1} + p_{Nr-1}^{n+1}}{\Delta r_{Nr}^2} + \frac{p_e - p_{Nr-1}^{n+1}}{2\Delta r_{Nr}} \left[ \frac{1}{r_{Nr}} + \left( \frac{3 - \phi_{Nr}^{n+1}}{\phi_{Nr}^{n+1} (1 - \phi_{Nr}^{n+1})} \right) \frac{\phi_{Nr} - \phi_{Nr-1}^{n+1}}{2\Delta r_{Nr}} + \left( \frac{\rho_f - \rho_s}{(1 - c_{Nr}^{n+1}) \rho_f + c_{Nr}^{n+1} \rho_s} \right) \frac{c_0 - c_{Nr-1}^{n+1}}{2\Delta r_{Nr}} \right] = 0. \quad (4.4.15)$$

It should be noted that Eqs. 4.4.10 - 4.4.15 already consider the boundary conditions, and it should also be noted that, in general, we have three equations and three unknowns, which are  $p^{n+1}$ ,  $\phi^{n+1}$  and  $c^{n+1}$ ; so, this system is solvable. The variable  $u^{n+1}$  will be added in parallel in section 4.6.

## 4.5 Newton-Raphson Method

In the previous section, a system of nonlinear algebraic equations was obtained in Eqs. 4.4.10 - 4.4.15. The nonlinearity exists in the product of the main variables that multiply each other and are at the same time step ( $n + 1$ ). This represents a problem because it is impossible to adapt a linear equation-solving algorithm. There are multiple ways to linearize a system of nonlinear equations, each with a specific stability criterion. In this case, the Newton-Raphson method will be used to linearize the system of equations, as it is the most efficient and straightforward method for solving nonlinear equations. This method will obtain all the unknowns at the time step ( $n + 1$ ). Let's consider a general system of nonlinear differential equations:

$$L_m\{F_m[w(x)]\} = f_m(x) \quad (4.5.1)$$

where  $m = 1, 2, \dots, M$ ,  $x \in \Omega$  and  $L_m$  denotes a linear differential operator,  $F_m(\cdot)$  is a nonlinear function,  $w = (w_1, w_2, \dots, w_m)^T$  is the vector of dependent variables (in our example it is  $p, \phi, c, u$ ),  $f = (f_1, f_2, \dots, f_m)^T$  is a given vector,  $M$  is the total number of equations, and  $T$  denotes the transpose of a vector. The Newton-Raphson method for solving equation (4.5.1) establishes an iterative equation system. The Taylor series expansion is:

$$F_m(w + \delta w) = F_m(w) + \nabla F_m(w) \cdot \delta w + O(|\delta w|^2) \quad (4.5.2)$$

Where  $|\delta w|$  is the Euclidean norm of  $\delta w$ . If the term  $O(|\delta w|^2)$  is truncated, then  $F_m(w + \delta w)$  approximates to:

$$F_m(w + \delta w) \approx F_m(w) + \nabla F_m(w) \cdot \delta w \quad (4.5.3)$$

If we substitute Eq. 4.5.3 into 4.5.1, we obtain the following iterative equations:

$$L_m\{F_m(w^l) + \nabla F_m(w^l) \cdot \delta w^{l+1}\} = f_m(x) \quad (4.5.4)$$

where  $w^l$  is the  $l$ -th iterative solution of  $w$  and  $\nabla F_m(w^l)$  is  $\nabla F_m(w)$  when  $w = w^l$  with an initial solution  $w^0$ . In the iterative equation system (4.5.4), the correction vector  $\delta w^{l+1}$  is the unknown. This system can be rewritten as follows:

$$L_m\{\nabla F_m(w^l) \cdot \delta w^{l+1}\} = g_m(x) \quad (4.5.5)$$

where  $g_m(x) = f_m(x) - L_m\{F_m(w^l)\}$ ,  $F_m(w^l)$  and  $\nabla F_m(w^l)$  are fixed. Now Eq. 4.5.5 is a linear system for  $\delta w^{l+1}$ . Note that  $\nabla F_m(w^l)$  is the Jacobian matrix of  $F_m$ , and that  $g_m$  is the residual of Eq. 4.5.1 at  $w^l$ . Consider  $g_m(x) = R_i$ , where  $i$  will be equal to the number of main variables. An updated solution vector  $w^{l+1}$  is obtained by adding the correction vector  $\delta w^{l+1}$  to the previous iteration of the solution vector  $w^l$ :

$$w^{l+1} = w^l + \delta w^{l+1} \quad (4.5.6)$$

This iterative process continues until the Euclidean norm of  $\delta w^{l+1}$  is very small, being a number close to 0. This number must be a prescribed value and is usually called tolerance described by the equation  $|w^{l+1} - w^l| < \textit{tolerance}$ . Defining the residuals  $R_i$  for the following Eqs. 4.3.8 – 4.3.10:

$$R_i^1 = \frac{c_i^{n+1}\phi_i^{n+1} - c_i^n\phi_i^n}{\Delta t} + \left( -\frac{k_0\phi_i^{n+3}}{(1-\phi_i^{n+1})^2\eta_k[(1-c_i^{n+1})\rho_f + c_i^{n+1}\rho_s]} \frac{p_{i+1}^{n+1} - p_{i+1}^n}{\Delta r_i} \right) \frac{c_{i+1}^{n+1} - c_{i+1}^n}{\Delta r_i} - \frac{\phi_i^{n+1} - \phi_i^n}{\Delta t} = 0, \quad (4.5.7)$$

$$R_i^2 = \frac{\phi_i^{n+1} - \phi_i^n}{\Delta t} - \lambda(1 - \phi_i^{n+1}) \left( c_i^{n+1} - \frac{c_i^{n+1^2}}{c_{cr_i}} \right) \left( \frac{k_0\phi_i^{n+3}}{(1-\phi_i^{n+1})^2\eta_k[(1-c_i^{n+1})\rho_f + c_i^{n+1}\rho_s]} \frac{p_{i+1}^{n+1} - p_{i+1}^n}{\Delta r_i} \right), \quad (4.5.8)$$

$$R_i^3 = \frac{p_{i+1}^{n+1} - 2p_i^{n+1} + p_{i-1}^{n+1}}{\Delta r_i^2} + \frac{p_{i+1}^{n+1} - p_{i-1}^{n+1}}{2\Delta r_i} \left[ \frac{1}{r_i} + \left( \frac{3 - \phi_i^{n+1}}{\phi_i^{n+1}(1 - \phi_i^{n+1})} \right) \frac{\phi_{i+1}^{n+1} - \phi_{i-1}^{n+1}}{2\Delta r_i} + \left( \frac{\rho_f - \rho_s}{(1 - c_i^{n+1})\rho_f + c_i^{n+1}\rho_s} \right) \frac{c_{i+1}^{n+1} - c_{i-1}^{n+1}}{2\Delta r_i} \right] = 0. \quad (4.5.9)$$

If we derive the residual with respect to each node of the main variable, we obtain the Jacobian matrix  $\nabla F_m(w^l)$ , which is formed by the first-order partial derivatives. If we apply the residual Eq. 4.5.5 concerning the main variables and considering that  $l = n$ , we will have the following for the variable  $p$ :

$$\frac{\partial R_i^{k^n}}{\partial p_{j+1}} \delta p_{i+1}^{n+1} + \frac{\partial R_i^{k^n}}{\partial p_j} \delta p_i^{n+1} + \frac{\partial R_i^{k^n}}{\partial p_{j-1}} \delta p_{i-1}^{n+1} = -R_i^{k^n}. \quad (4.5.10)$$

For the variable  $c$ :

$$\frac{\partial R_i^{k^n}}{\partial c_{j+1}} \delta c_{i+1}^{n+1} + \frac{\partial R_i^{k^n}}{\partial c_j} \delta c_i^{n+1} + \frac{\partial R_i^{k^n}}{\partial c_{j-1}} \delta c_{i-1}^{n+1} = -R_i^{k^n}. \quad (4.5.11)$$

And for the variable  $\phi$ :

$$\frac{\partial R_i^{k^n}}{\partial \phi_{j+1}} \delta \phi_{i+1}^{n+1} + \frac{\partial R_i^{k^n}}{\partial \phi_j} \delta \phi_i^{n+1} + \frac{\partial R_i^{k^n}}{\partial \phi_{j-1}} \delta \phi_{i-1}^{n+1} = -R_i^{k^n}. \quad (4.5.12)$$

where  $k = 1, 2, 3, i = 1, \dots, Nr$  and  $j = 1, \dots, N$

Eqs. 4.5.10 – 4.5.12 can be represented in matrix form, a matrix with nine sub-matrices for each Jacobian, so the number of unknowns would be  $3Nr$ . Eqs. 4.5.10 – 4.5.12 are represented in matrix form as follows:

$$\begin{bmatrix} \left[ \frac{\partial R_i^{1n}}{\partial \phi_j} \right] & \left[ \frac{\partial R_i^{1n}}{\partial c_j} \right] & \left[ \frac{\partial R_i^{1n}}{\partial p_j} \right] \\ \left[ \frac{\partial R_i^{2n}}{\partial \phi_j} \right] & \left[ \frac{\partial R_i^{2n}}{\partial c_j} \right] & \left[ \frac{\partial R_i^{2n}}{\partial p_j} \right] \\ \left[ \frac{\partial R_i^{3n}}{\partial \phi_j} \right] & \left[ \frac{\partial R_i^{3n}}{\partial c_j} \right] & \left[ \frac{\partial R_i^{3n}}{\partial p_j} \right] \end{bmatrix}^n \begin{bmatrix} \delta \phi_i \\ \delta c_i \\ \delta p_i \end{bmatrix}^{n+1} = - \begin{bmatrix} [R_i^1] \\ [R_i^2] \\ [R_i^3] \end{bmatrix}^n. \quad (4.5.13)$$

If we analyze the system of linear equations in the form  $[A]\{\vec{x}\} = \{\vec{b}\}$ , we can deduce that the solution is found using a solution algorithm for systems of linear equations. In Eqs. 4.5.13, the matrix is at time  $n$ , while the deltas are at time  $n + 1$ , which suggests that the only unknowns are at time  $n + 1$  and will be calculated using Eq. 4.5.6. The Jacobians and residuals of Eqs. 4.5.10 - 4.5.12 can be found in **Appendix C**. To find the variables  $p^{n+1}, \phi^{n+1}$  and  $c^{n+1}$ , the following equations will simply be used:

$$p^{n+1} = p^n + \delta p^{n+1}, \quad (4.5.14)$$

$$\phi^{n+1} = \phi^n + \delta \phi^{n+1}, \quad (4.5.15)$$

$$c^{n+1} = c^n + \delta c^{n+1}. \quad (4.5.16)$$

## 4.6 Coupling of Mechanical Deformation

Since the parameters  $\phi$ ,  $c$ , and  $p$  of each node and time are calculated at the time  $(n+1)$ , the partial differential Eq. 3.7.6 is solved using a finite difference scheme. The unknown variable will be the displacement function ( $u$ ) at the nodes. Eq. 3.7.6 with the boundary conditions 4.2.12 and 4.2.13 are spatially discretized to obtain the following matrix arrangement:

$$[A]\{\vec{u}\} = \{\vec{b}\}. \quad (4.6.1)$$

It is important to mention that to arrive at Eq. 4.6.1, the temporal discretization will be implicit, which implies updating the displacement variable with respect to the three main variables. This is possible because the coupling of Eq. 4.6.2 is a weak coupling, that is, the variable  $u$  depends on the three main variables  $\phi$ ,  $c$  and  $p$ , while these three main variables do not depend on the displacement variable  $u$ . So, by spatially discretizing Eq. 3.7.6, we arrive at:

$$\frac{u_{i+1} - 2u_i + u_{i-1}}{\Delta r_i^2} + g_{1i} \frac{u_{i+1} - u_{i-1}}{2\Delta r_i} - g_{2i} u_i = g_3 \frac{(\phi p)_{i+1} - (\phi p)_i}{\Delta r_i}. \quad (4.6.2)$$

where:

$$g_{1i} = \frac{1}{r_i} - \frac{1}{1-\phi_i} \frac{\phi_{i+1} - \phi_i}{\Delta r_i}, \quad (4.6.3)$$

$$g_{2i} = \frac{1}{r_i^2} + \frac{1}{r_i} \frac{v}{1-v} \frac{1}{1-\phi_i} \frac{\phi_{i+1} - \phi_i}{\Delta r_i}, \quad (4.6.4)$$

$$g_{3i} = \frac{(1+v)(1-2v)}{\bar{E}(1-\phi_i)(1-v)}. \quad (4.6.5)$$

Temporally discretizing the deformation variable at level  $k+1$ , while for the main variables  $n+1$  is still used, we obtain:

$$\frac{u_{i+1}^{k+1}-2u_i^{k+1}+u_{i-1}^{k+1}}{\Delta r_i^2} + g_{1_i}^{n+1} \frac{u_{i+1}^{k+1}-u_{i-1}^{k+1}}{2\Delta r_i} - g_{2_i}^{n+1} u_i^{k+1} = g_{3_i}^{n+1} \frac{(\phi p)_{i+1}^{n+1} - (\phi p)_i^{n+1}}{\Delta r_i}. \quad (4.6.6)$$

For each node, we obtain the following:

Node  $i = 1$

$$\frac{u_2^{k+1}-2u_1^{k+1}+u_0^{k+1}}{\Delta r_1^2} + g_{1_1}^{n+1} \frac{u_2^{k+1}-u_0^{k+1}}{2\Delta r_1} - g_{2_1}^{n+1} u_1^{k+1} = g_{3_1}^{n+1} \frac{(\phi p)_2^{n+1} - (\phi p)_1^{n+1}}{\Delta r_1}, \quad (4.6.7)$$

Node  $i = 1, \dots, Nr - 1$

$$\frac{u_{i+1}^{k+1}-2u_i^{k+1}+u_{i-1}^{k+1}}{\Delta r_i^2} + g_{1_i}^{n+1} \frac{u_{i+1}^{k+1}-u_{i-1}^{k+1}}{2\Delta r_i} - g_{2_i}^{n+1} u_i^{k+1} = g_{3_i}^{n+1} \frac{(\phi p)_{i+1}^{n+1} - (\phi p)_i^{n+1}}{\Delta r_i}, \quad (4.6.8)$$

Node  $i = Nr$

$$\frac{u_{Nr+1}^{k+1}-2u_{Nr}^{k+1}+u_{Nr-1}^{k+1}}{\Delta r_{Nr}^2} + g_{1_{Nr}}^{n+1} \frac{u_{Nr+1}^{k+1}-u_{Nr-1}^{k+1}}{2\Delta r_{Nr}} - g_{2_{Nr}}^{n+1} u_{Nr}^{k+1} = g_{3_{Nr}}^{n+1} \frac{(\phi p)_{Nr+1}^{n+1} - (\phi p)_{Nr}^{n+1}}{\Delta r_{Nr}}. \quad (4.6.9)$$

Applying the boundary conditions to the equation found in **Appendix D**:

Node  $i = 1$

$$\frac{u_2^{k+1}-2u_1^{k+1}}{\Delta r_1^2} + g_{1_1}^{n+1} \frac{u_2^{k+1}}{2\Delta r_1} + \left( \frac{1}{\Delta r_1^2} - \frac{g_{1_1}^{n+1}}{2\Delta r_1} \right) \left( u_2^{k+1} + 2\Delta r_1 \left( \frac{v}{1-v} \frac{u_1^{k+1}}{r_1} + g_{3_1}^{n+1} [\phi_1 p_1 - p_1] \right) \right) - g_{2_1}^{n+1} u_1^{k+1} = g_{3_1}^{n+1} \frac{(\phi p)_2^{n+1} - (\phi p)_1^{n+1}}{\Delta r_1}. \quad (4.6.10)$$

Eq. 4.6.10 can be simplified as follows:

$$\frac{2u_2^{k+1}-2u_1^{k+1}}{\Delta r_1^2} - g_{2_1}^{n+1} u_1^{k+1} + \left( \frac{2}{\Delta r_1^2} - g_{1_1}^{n+1} \right) \left( \frac{v}{1-v} \frac{u_1^{k+1}}{r_1} \right) = g_{3_1}^{n+1} \frac{(\phi p)_2^{n+1} - (\phi p)_1^{n+1}}{\Delta r_1} + \left( g_{3_1}^{n+1} g_{1_1}^{n+1} - \frac{2g_{3_1}^{n+1}}{\Delta r_1} \right) + [\phi_1 p_1 - p_1]. \quad (4.6.11)$$

In the same way for the node  $i = Nr - 1$

$$\frac{-2u_{Nr}^{k+1}+2u_{Nr-1}^{k+1}}{\Delta r_{Nr}^2} + \left( \frac{2}{\Delta r_{Nr-1}^2} - g_{1_{Nr-1}}^{n+1} \right) \left( \frac{v}{1-v} \frac{u_{Nr-1}^{k+1}}{r_{Nr-1}} \right) - g_{2_{Nr-1}}^{n+1} u_{Nr-1}^{k+1} = \dots g_{3_{Nr-1}}^{n+1} \frac{(\phi p)_{Nr}^{n+1} - (\phi p)_{Nr-1}^{n+1}}{\Delta r_{Nr}} + \dots \left( g_{3_{Nr-1}}^{n+1} g_{1_{Nr-1}}^{n+1} - \frac{2g_{3_{Nr-1}}^{n+1}}{\Delta r_{Nr-1}} \right) + [\phi_e p_e - S_e]. \quad (4.6.12)$$

Once the boundary conditions have been coupled, Eqs. 4.6.8, 4.6.10, and 4.6.12 are adapted into the following matrix arrangement:

$$\{\vec{u}\} = \begin{Bmatrix} u_1 \\ u_2 \\ \vdots \\ u_i \\ \vdots \\ u_{Nr} \end{Bmatrix}^{k+1}, \quad (4.6.13)$$

$$\{\vec{b}\} = \left\{ \begin{array}{l} g_{3_1}^n \frac{(\phi p)_2^n - (\phi p)_1^n}{\Delta r_{Nr}} + (g_{3_1}^n g_{1_1}^n - \frac{2g_{3_1}^n}{\Delta r_1}) + [\phi_1 p_1 - p_1] \\ g_{3_2}^n \frac{(\phi p)_3^n - (\phi p)_2^n}{\Delta r_2} \\ \vdots \\ g_{3_i}^n \frac{(\phi p)_{i+1}^n - (\phi p)_i^n}{\Delta r_i} \\ \vdots \\ g_{3_{Nr-1}}^n \frac{(\phi p)_{Nr}^n - (\phi p)_{Nr-1}^n}{\Delta r_{Nr-1}} + (g_{3_{Nr-1}}^n g_{1_{Nr-1}}^n - \frac{2g_{3_{Nr-1}}^n}{\Delta r_{Nr-1}}) + [\phi_e p_e - S_e] \end{array} \right\}^{n+1}. \quad (4.6.14)$$

The matrix arrangement now has the following form:

$$[A]^{n+1} \{\vec{u}\}^{k+1} = \{\vec{b}\}^{n+1} \quad (4.6.15)$$

The system of Eqs. 4.6.15 is solved using conventional methods for solving systems of linear equations, which allows us to obtain the values of the displacement vector ( $\vec{u}$ ). In this way, the deformation is updated in the same time step as the main variables  $\phi$ ,  $c$  and  $p$ .

## 4.7 Solution Algorithm

---

**Algorithm 4.1** General Solution Algorithm

---

```
1: Start.
2: Input initial values.
3: Define simulation mesh.
4: Define time increment, delta time, and total time.
5: Define tolerance.
6: While  $time < simulation\ time$  do:
7:   While  $\Delta Norm > tolerance$  do:
8:     Obtain Jacobian matrix of residuals and residual vector (as in Eq. 4.5.13).
9:     Solve the system of equations.
10:    Calculate  $\Delta Norm$ .
11:    If  $\Delta Norm > tolerance$  :
12:      Find the main variables with Eqs. 4.5.14 – 4.5.16.
13:      The solutions are  $p^{n+1}, \varphi^{n+1} y c^{n+1}$ .
14:    If Not  $\Delta Norm > tolerance$  :
15:      Return to step 1 and check for possible errors.
16: Substitute the main variables at time  $n + 1$  into Eq. 4.6.15 to obtain the displacement vector.
17: The solution is  $u^{n+1}$ .
18: Find effective stresses with the result of  $u^{k+1}$ .
19: Print graphs and results.
20: End.
```

---

## 4.8 Simulator Validation

To validate and verify the simulator's operation, multiple runs were conducted using the Python programming language, version 3, to replicate the results of the work by Stavropoulou et al. (1998). The data from Table 1 proposed by Stavropoulou were used, and they are presented in Table 4.1 of this section.

Figs. 3 and 4 from Stavropoulou's work are reproduced, showing the alteration of porosity with respect to distance at different times and the alteration of pressure with respect to distance at different times. Figs. 4.4a and 4.4b represent Figs. 3 and 4 of the original work. Figs. 4.5a and 4.5b are those generated by the proposed simulator.

It is important to note that the main difference lies in the fact that the original article used the finite element method, while the simulator in this work was based on the finite difference method. The difference between having a finite difference scheme lies in the fact that the error can be more pronounced because the approximation of the derivatives is based on a Taylor series, which can lead to significant errors, especially in cases where a Taylor series do not easily represent the function. On the other hand, in finite element methods, the error tends to be minimized. This is because the discretization is performed using a continuous integral scheme instead of direct derivatives.

<b>Physical Parameters</b>	<b>Value</b>
<i>Well radius</i>	$r_{wf} = 0.1 [m]$
<i>External radius</i>	$r_e = 5 [m]$
<i>Initial Porosity</i>	$\varphi_0 = 0.25$
<i>Initial Concentration</i>	$c_0 = 10^{-3}$
<i>Critical Concentration</i>	$c_{cr} = 0.3$
<i>Initial Permeability</i>	$k = 373 [md]$
<i>Young Modulus</i>	$E = 2 [GPa]$
<i>Poisson's Ratio</i>	$\nu = 0.3$
<i>Kinematic Viscosity of the Fluid</i>	$\eta_k = 5 \times 10^{-6} [m^2 s^{-1}]$
<i>Fluid Density</i>	$\rho_f = 840 [kg m^{-3}]$
<i>Densidad of the Rock</i>	$\rho_s = 2,650 [kg m^{-3}]$
<i>pwf</i>	$p_{wf} = 5 [MPa] (725 \text{ psi})$
<i>External Pressure</i>	$p_e = 8 [MPa] (1160 \text{ psi})$
<i>External Stress</i>	$\sigma_e = 20 [MPa] (2900 \text{ psi})$
<i>Erosion Coefficient</i>	$\lambda = 5 [m^{-1}]$
<i>Initial Cohesion</i>	$C_o = 7.5 [MPa] (1088 \text{ psi})$
<i>Internal Friction Angle</i>	$\theta = 37^\circ$
<i>Number of Nodes</i>	$N_r = 100$
<i>Final Time</i>	$t_f = 10,000 [s]$
<i>Time Delta</i>	$dt = 10 [s]$
<i>Radius Delta</i>	$dr = 0.5$
<i>Newton-Raphson Epsilon</i>	$\varepsilon_{NR} = 1 \times 10^{-5}$

**Table 4. 1** Input Data for the Simulator (*Stavropoulou, Papanastasiou, & Vardoulakis, 1998*)

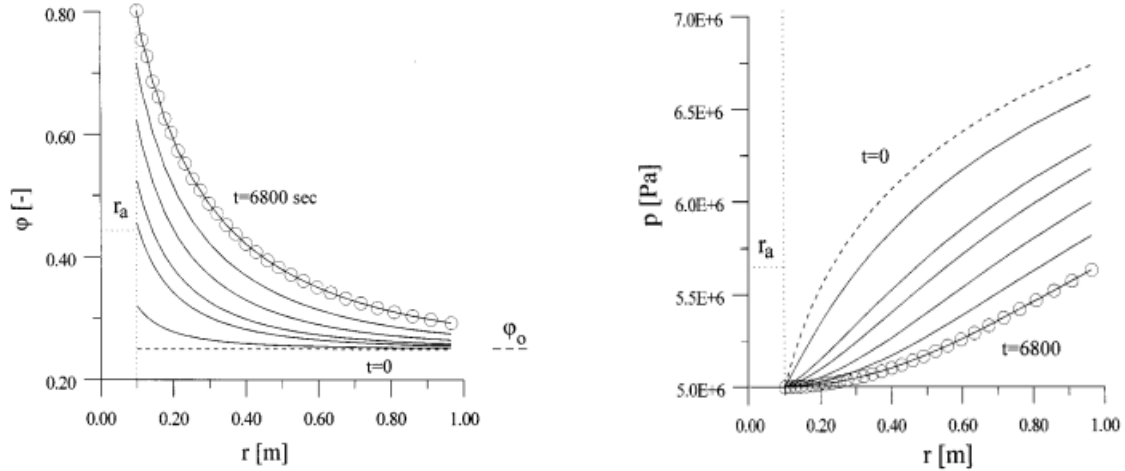


**Figure 4. 4:** a) Spatial Profile of Porosity at Various Times. b) Spatial Profile of Pressure at Various Times. (Stavropoulou, Papanastasiou, & Vardoulakis, 1998)

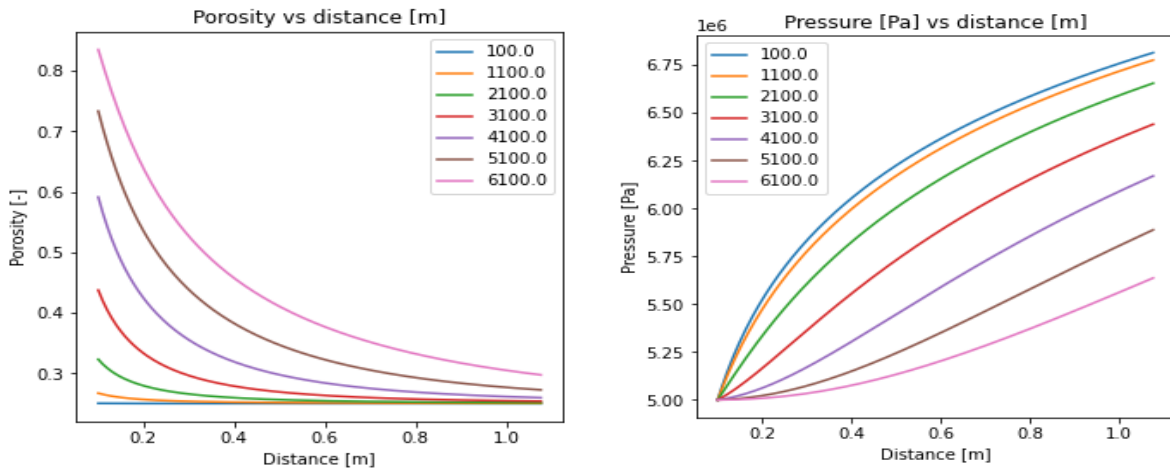


**Figure 4. 5 At Various Simulation Times:** a) Spatial Profile of Porosity b) Spatial Profile of Pressure.

Figs. 5 and 6 show how porosity and transport concentration at the first node vary over time. These figures are represented in Figs. 4.6a and 4.6b. The results obtained from the simulator of this study are compared with those in Figs. 4.7a and 4.7b. A rapid increase in porosity and concentration is observed after a specific time. In Fig. 4.7a, it is noted how the value approaches 1, which is the maximum porosity or a free surface. Fig. 4.7b shows that the concentration converges to the asymptotic value of 0.3, corresponding to the critical concentration.

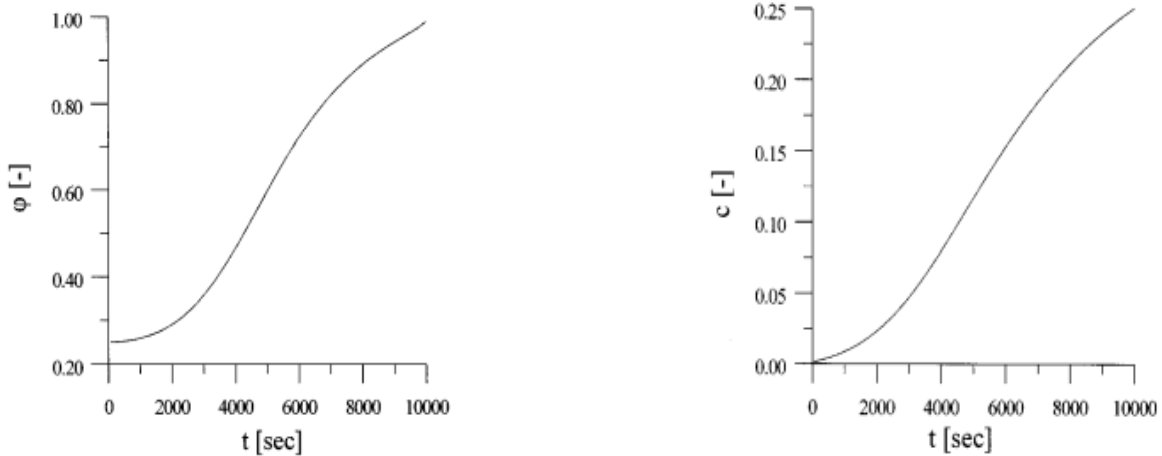


**Figure 4. 6** a) Porosity Variation with Respect to Time at the Initial Node. b) Variation of Transport Concentration with Respect to Time at the First Node. (*Stavropoulou, Papanastasiou, & Vardoulakis, 1998*)

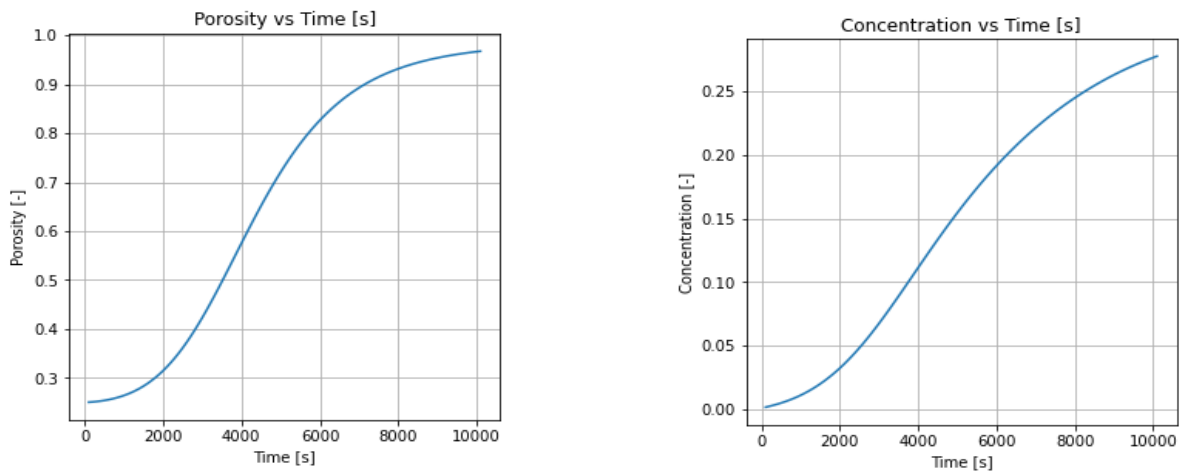


**Figure 4. 7** a) Variation of Porosity with Respect to Time at the First Node of the Simulator. b) Variation of Transport Concentration with Respect to Time at the First Node of the Simulator.

Deformation is first determined for the geomechanical parameters to calculate the effective stresses. Figs. 4.8 and 4.9 of the paper are compared using Figs. 4.8a and 4.9b. The figures are reproduced with the simulator, resulting in Figs. 4.9, 4.10a, and 4.10b. It should be noted that erosion in the vicinity of the well induces a mechanical alteration of the medium. Fig. 4.9 presents the spatial profiles of radial displacement at different times. Figs. 4.10a and 4.10b show the temporal variation of radial displacement and its derivative at the well face.

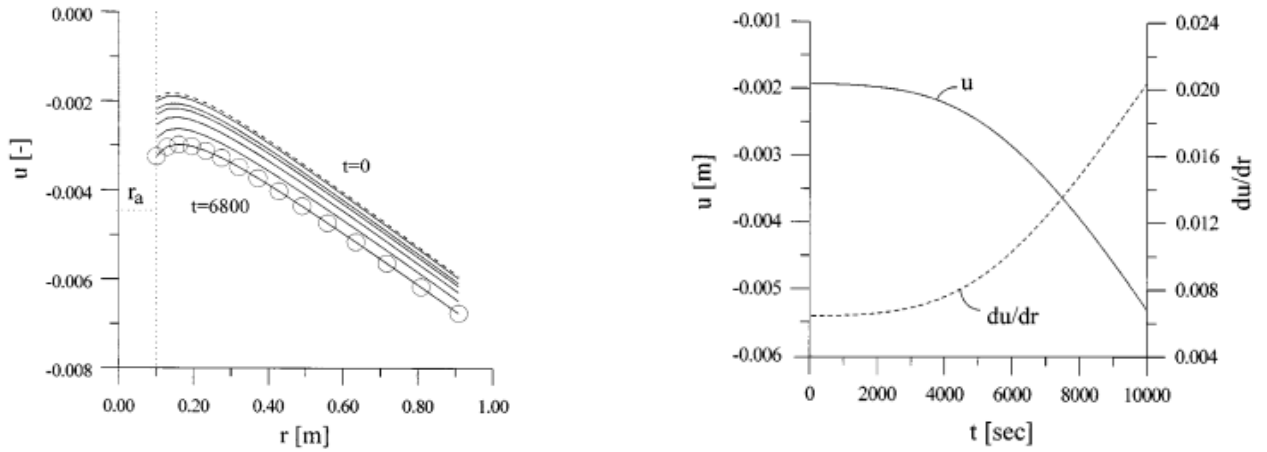


**Figure 4. 8** a) Distribution of Radial Displacement Simulated at Various Times. b) Variation of Radial Displacement and Strain with Respect to Time, Evaluated at the Well Radius. (Stavropoulou, Papanastasiou, & Vardoulakis, 1998)

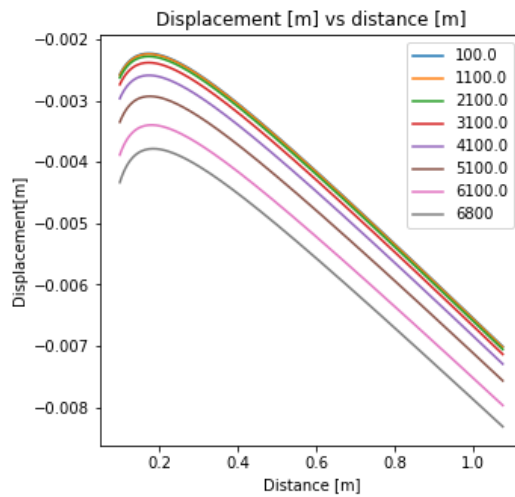


**Figure 4. 9** Distribution of Radial Displacement Simulated at Various Times.

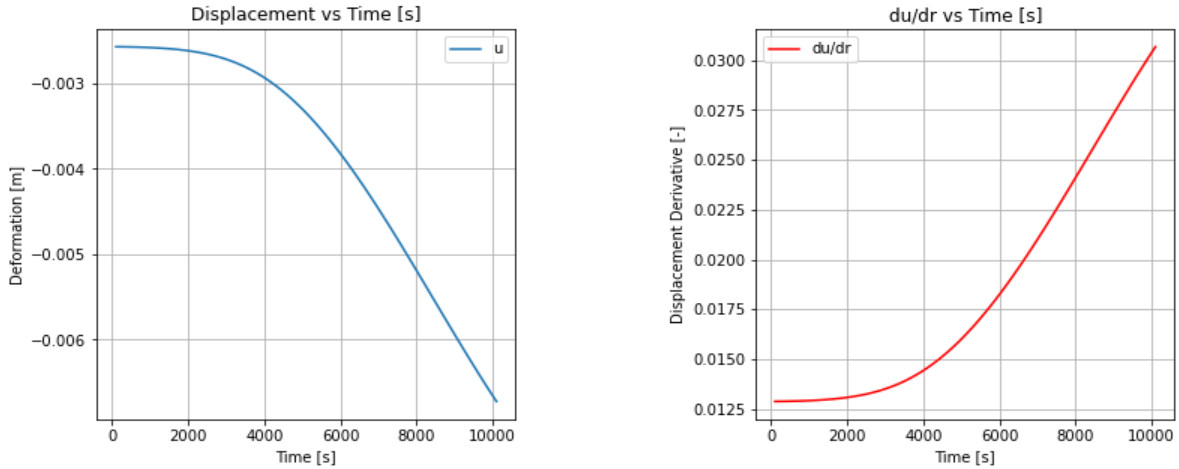


**Figure 4. 10** a) Temporal Variation of Radial Displacement at the Wellbore Wall Obtained by the Simulator. b) Temporal Variation of the Strain Derivative at the Wellbore Wall Obtained by the Simulator.

For the effective stresses, Figs. 10 and 11 of the article are obtained, represented by Figs. 4.11a and 4.11b. These figures are compared with Figs. 4.12a and 4.12b, respectively. As observed earlier, there is an increase in the absolute value of radial displacement and its slope. These increases cause a decrease in the gradient of radial effective stress, as shown in Fig. 4.12a, and in turn a decrease in tangential effective stress, as seen in Fig. 4.12b.

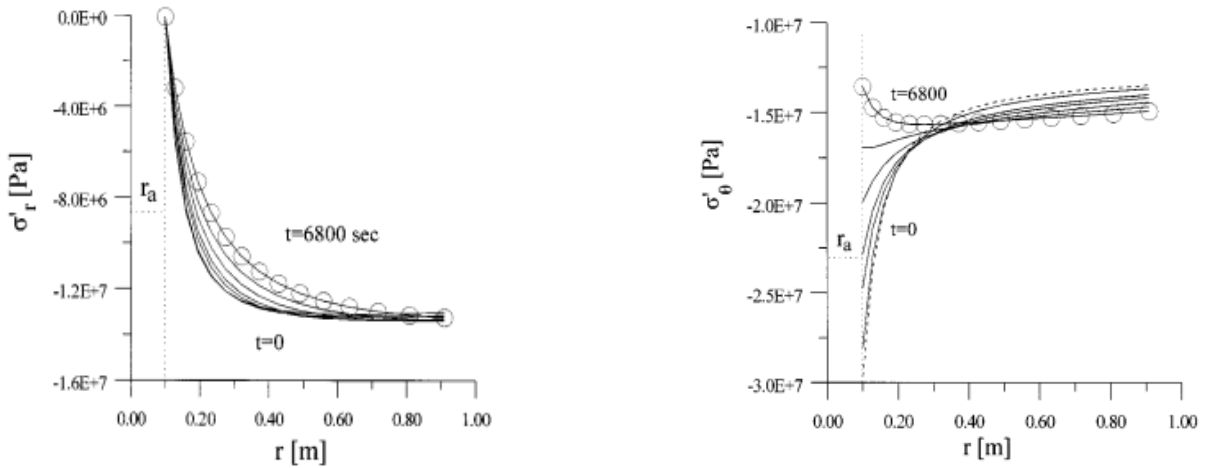


**Figure 4. 11** Various Times Distribution of a) Radial Effective Stress. b) Tangential Effective Stress. (Stavropoulou, Papanastasiou, & Vardoulakis, 1998)

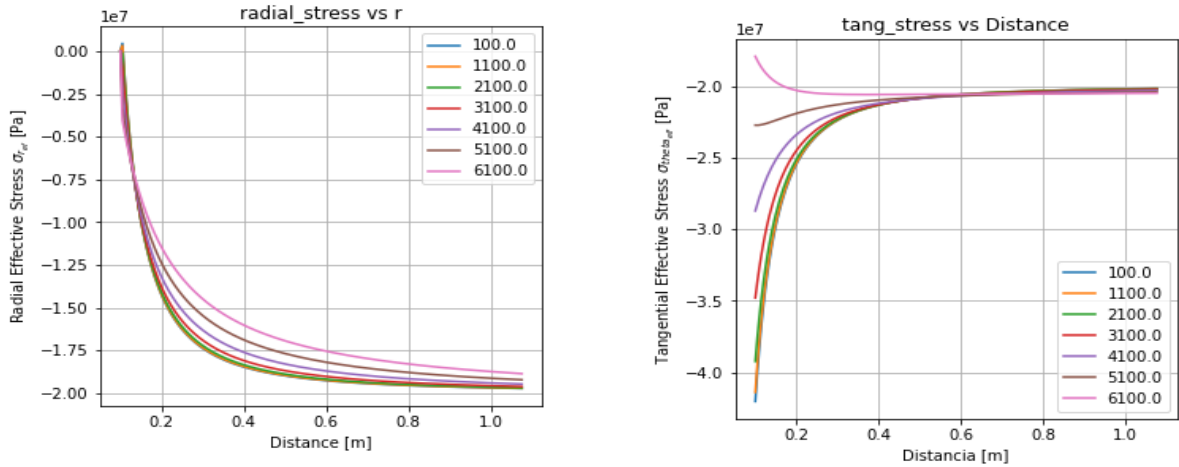


**Figure 4. 12** Various Time Distribution of a) Radial Effective Stress from the Simulator. b) Tangential Effective Stress obtained by the Simulator.

Considering the solution of the elastic stress problem, a well failure analysis is performed using the modified Mohr-Coulomb criterion. The results of the article are shown in Fig. 4.13, while the simulator results are presented in Fig. 4.14a and in more detail in Fig. 4.14b. In Fig. 4.14a, continuous observation of how the failure envelope reaches the stress field indicates rock collapse at that point. Additionally, it is noted that in Fig. 4.14b, the failure envelope intersects the stress field around 3,500-time units, causing the formation node to collapse at that moment.

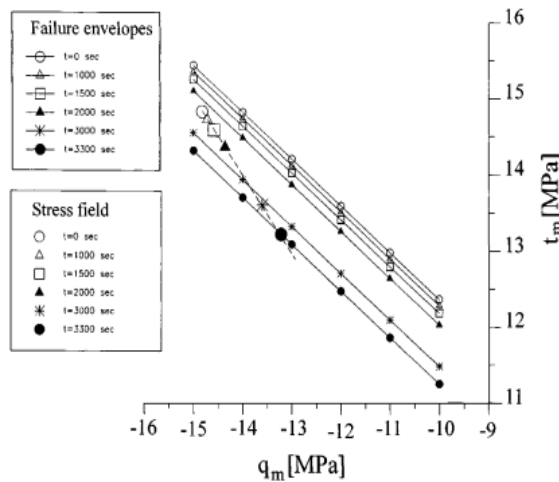


**Figure 4. 13** Failure Envelopes and Critical Stresses Corresponding to the Inner Boundary  $r = r_w$ , at Different Times ( $\theta = 37^\circ, \bar{C} = 7.5 [Mpa]$ ) (Stavropoulou, Papanastasiou, & Vardoulakis, 1998)

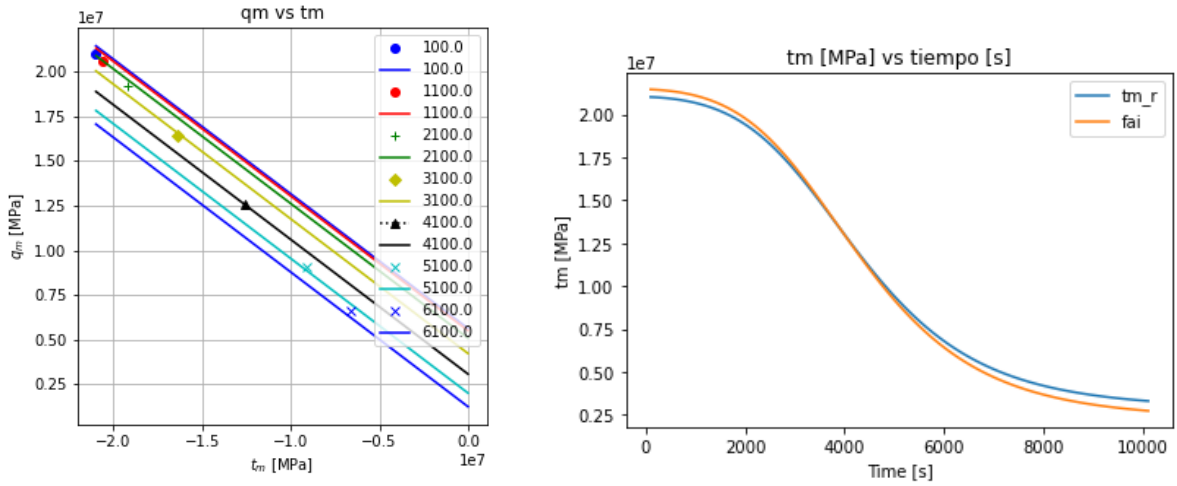


**Figure 4. 14** a) Failure Envelopes and Critical Stresses Corresponding to the Inner Boundary  $r = r_w$ , at Different Times ( $\theta = 37^\circ$ ,  $\bar{C} = 7.5$  [Mpa]) Obtained by the Simulator. b) Variation of the Failure Envelope and Stress Field at the Inner Boundary  $r = r_w$ , at Different Times ( $\theta = 37^\circ$ ,  $\bar{C} = 7.5$  [Mpa]) Obtained by the Simulator.

## 4.9 Case Study Analysis

The main objective of this analysis is to adapt the explicit model of Stavropoulou (1998) to a carbonate reservoir in an implicit scheme, as there is not much information in the literature about prediction models for the collapse of such formations. In this section, a case study was conducted with characteristics of a real carbonate reservoir located in the state of Indiana, United States, which are represented with data from Table 4.2.

One important aspect to consider is that the model only applies within the investigation radius where the in-situ stress system has been modified to a local stress system. As the distance increases, the formation's geomechanical behavior begins to show deviations and errors.

Physical Parameters	Values
<i>Well Radius</i>	$r_{wf} = 0.1 [m]$
<i>External Radius</i>	$r_e = 5 [m]$
<i>Initial Porosity</i>	$\varphi_0 = 0.15$
<i>Initial Concentration</i>	$c_0 = 10^{-3}$
<i>Critical Concentration</i>	$c_{cr} = 0.3$
<i>Initial Permeability</i>	$k = 5.0 [md]$
<i>Young's Modulus</i>	$E = 29 [GPa]$
<i>Poisson's Ratio</i>	$\nu = 0.18$
<i>Kinematic Viscosity of the Fluid</i>	$\eta_k = 4.0 \times 10^{-6} [m^2 s^{-1}]$
<i>Fluid Density</i>	$\rho_f = 834 [kg m^{-3}]$
<i>Density of the Solids</i>	$\rho_s = 2250 [kg m^{-3}]$
<i>pwf</i>	$p_{wf} = 10 [MPa] (1450 \text{ psi})$
<i>External Pressure</i>	$p_e = 15 [MPa] (2175 \text{ psi})$
<i>External Stress</i>	$\sigma_e = 20 [MPa] (2900 \text{ psi})$
<i>Erosion Coefficient</i>	$\lambda = 5 [m^{-1}]$
<i>Initial Cohesion</i>	$C_o = 10 [MPa] (1450 \text{ psi})$
<i>Internal Friction Angle</i>	$\theta = 35^\circ$
<i>Number of Nodes</i>	$N_r = 200$

<i>Final Time</i>	$t_f = 40$ [hrs]
<i>Time Delta</i>	$dt = 100$ [s]
<i>Radius Delta</i>	$dr = 0.5$
<i>Newton-Raphson Epsilon</i>	$\varepsilon_{NR} = 1 \times 10^{-5}$

**Table 4. 2** Input Data for the Case Simulator

### 4.9.1 Physical Analysis

To validate a simulator, it is necessary to vary the parameters. For this work, the parameter varied are permeability, cohesion, Poisson's ratio, and the internal friction angle. From the values in Table 4.2, Fig. 4.16 is obtained. It can be observed in Fig. 4.16a that the rock will begin to fail at a porosity close to 0.6; from then on, the slope gradually decreases, which means that the rock continues to erode but at a slower rate. From Fig. 4.16c, we can see that at approximately 32 hours, the failure envelope reaches the stress field.

Also, it can be observed that by applying the explicit model in an implicit scheme, instability problems arose for extended periods. This occurs because the Newton-Raphson algorithm tends to minimize errors. As a result, it was necessary to perform multiple simulations using different time delta values to determine the optimal value that stabilized the model.

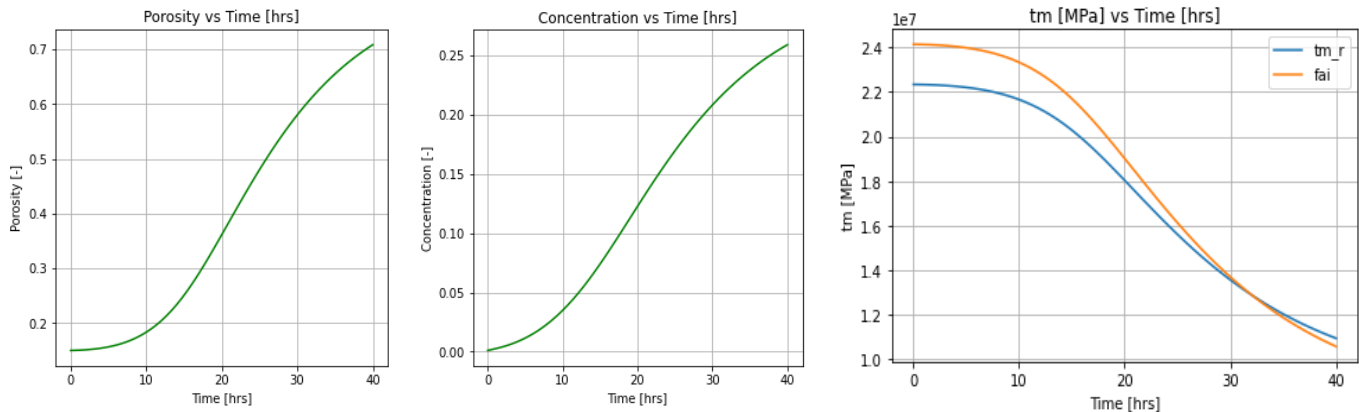


**Figure 4. 15** Variation of Porosity with Respect to Time at the Initial Node. b) Variation of Transport Concentration at the Initial Node. c) Variation of the Failure Envelope and Stress Field at the Inner Boundary  $r = r_w$ , at Different Times.

### 4.9.2 Physical Effect of Permeability

Permeability is one of the most important parameters when analyzing fluid flow; if the permeability increases, the flow rate will be higher, and if the flow rate is higher, the erosion forces will also be greater, and the rock failure will be faster. Fig. 4.17 demonstrates that with higher permeability, the porosity and concentration reach their critical value more quickly, and this can be confirmed with Fig. 4.17c, where the formation fails at approximately 8 hours.

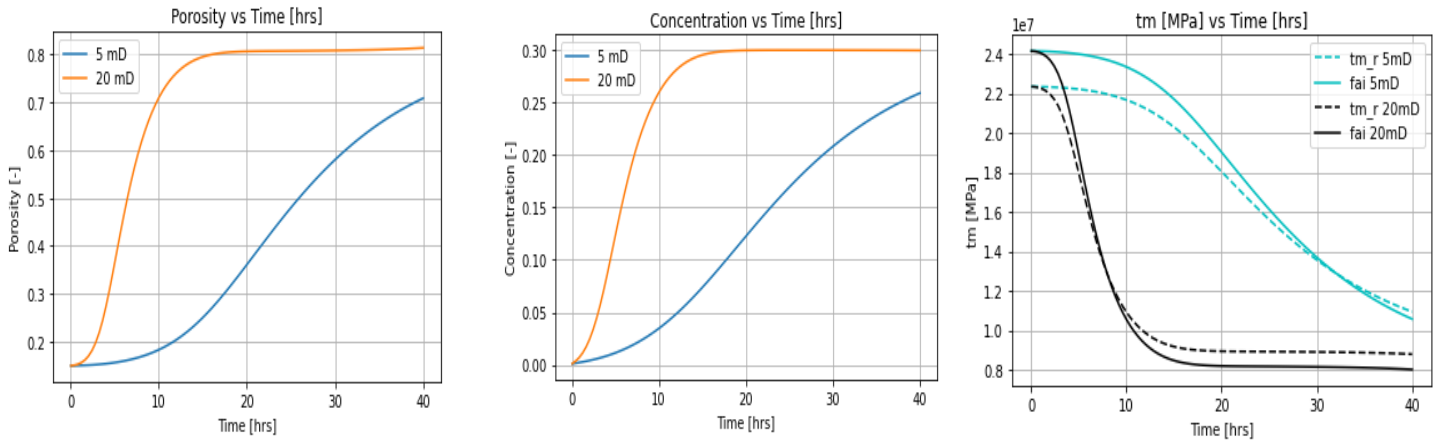


**Figure 4. 16** a) Variation of Porosity, Figure a), transport concentration, Figure b) and Failure Envelope and Stress Field at the Inner Boundary  $r = r_w$ , Concerning Time at the Initial Node at Two Different Permeabilities.

### 4.9.3 Physical Effect of Cohesion

Cohesion is one of the main geomechanical parameters highlighted in this flow model adapted to movable solids. When the rock's cohesion decreases, the formation erodes earlier. As can be seen in Fig 4.18, if we increase the cohesion value to 20 MPa, the rock will take longer to collapse. A higher cohesion mean that the rock has greater compaction; this is why the collapse takes longer to occur.

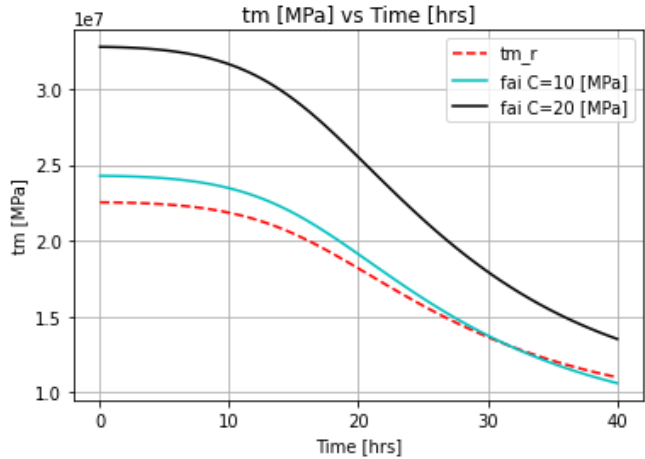


**Figure 4. 17** Variation of the Failure Envelope and Stress Field at the Inner Boundary  $r = r_w$ , at Different Times Obtained by the Simulator at Two Different Cohesion Values.

### 4.9.3 Physical Effect of Poisson's Ratio

Poisson's ratio is an equation that measures the hardness of a rock and is a critical property related to fracture closure stress. As for its influence on rock failure, it is not very significant, Fig. 4.19 shows that the change indicates how easily the rock can fail. However, by increasing Poisson's ratio, the generation of the stress field is affected, causing a shift between the two curves to higher values. However, the rock collapses almost simultaneously.

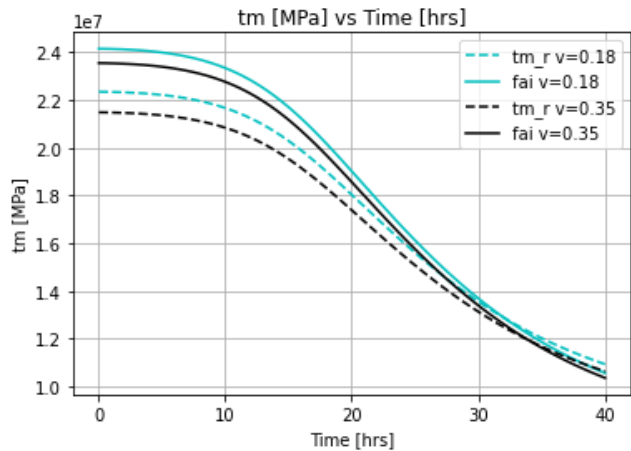


**Figure 4. 18** Variation of the Failure Envelope and Stress Field at the Inner Boundary  $r = r_w$ , at Different Times Obtained by the Simulator, at Two Different Poisson's Ratios.

### 4.9.4 Physical Effect of Internal Friction Angle

The internal friction angle is generally obtained from triaxial tests, although the term originates from Eq. 2.4.68. Savage et al. (1996) argued that this effect is due to friction forces that occur by sliding along the micro-scale portions of the fault surface that are not intact. Fig. 4.20 shows that when the angle is larger, the failure lines are further away from the stress fields, delaying failure. It can be observed that at an angle of  $43^\circ$ , collapse does not occur within the first 40 hours.

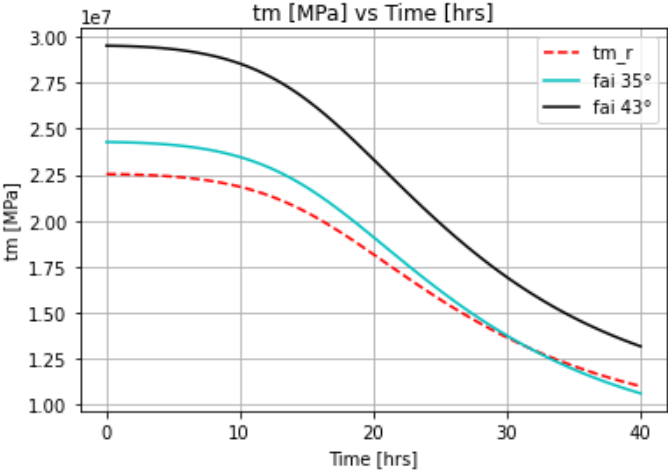


**Figure 4. 19** Variation of the failure envelope and the stress field at the inner boundary  $r = r_w$ , at different times obtained through the simulator at two different internal friction angles.

## 5. Conclusions

The collapse of the formation and the potential production of solids in carbonate reservoirs depend on the rock's physical and mechanical properties. The interaction between these two aspects generates uncertainty regarding the time of rock failure. However, accurately predicting these events is complex due to the nature of rock formations, especially in carbonate formations.

In the existing literature, no specific models predict the collapse in carbonate formations, which led to the adaptation of a model designed initially for sands in an explicit scheme. However, when attempting to apply this model in an implicit scheme, instability problems arose for extended periods. This occurs because the Newton-Raphson algorithm tends to minimize errors, but the speed at which information is transmitted between neighboring nodes introduces errors, especially when the physical information is not generated adequately. As a result, it was necessary to perform multiple simulations using different time delta values to determine the optimal value that stabilized the model.

The developed numerical model finds its main application in wells located in mature reservoirs with open-hole completion, where the formation has been exposed to prolonged fluid production, causing erosion and weakening of the rock. Additionally, this model is useful when detailed geomechanical data or fluid tests are available. However, it is important to note that the current model only contemplates oil production. To improve its scope, it is suggested that the model be extended to consider multiphase flow, as the presence of gas and water can significantly alter the conditions that lead to the collapse of the formation. Similarly, the mesh could be discretized logarithmically to work with larger models over long time periods.

Another crucial aspect to consider is that the model only applies within the investigation radius where the in-situ stress system has been modified to a local stress system. As the distance increases, the formation's geomechanical behavior begins to show deviations and errors.

Accurately obtaining geomechanical data is essential to improving prediction accuracy. Therefore, it is highly recommended to collect cores during the drilling stage, which will allow obtaining the rock's static parameters. Additionally, the acquisition of geophysical logs is essential to determining the formation's dynamic parameters, which will contribute to generating more robust and reliable models.

Although the current model represents a significant advance in predicting the collapse of carbonate formations under depletion conditions, its accuracy largely depends on the correct collection and analysis of geomechanical data and the future inclusion of multiphase flows to better represent the actual reservoir conditions.

# Nomenclature

$\bar{a}$	Acceleration [ $ft/s^2$ ]
$A$	Area [ $ft^2$ ]
$A_p$	Perpendicular area of the YZ plane YZ [ $ft^2$ ]
$A_n$	Normal area [ $ft^2$ ]
$b_i$	Body force [ $lb_i$ ]
$c$	Concentration of mobile solids []
$c_{cr}$	Critical Concentration [-]
$C_o$	Initial Cohesion with damage [ $psi$ ]
$C$	Cohesion [ $psi$ ]
$dS_i$	Sectional Area [ $ft^2$ ]
$e_i$	Axis direction in $i$ [-]
$E$	Young's Modulus [ $psi$ ]
$F$	Force [ $lb_i$ ]
$F_m$	Mass Flow rate [ $lb/s$ ]
$G$	Shear Modulus [ $psi$ ]
$h_w$	Well height [ $ft$ ]
$k$	Permeability [ $mD$ ]
$k_0$	Initial Permeability [ $md$ ]
$l$	System length [ $ft$ ]
$m$	Mass [ $lb$ ]
$\dot{m}_{cr}$	Critical mass flow rate [ $lb/s$ ]

$M_s$	Solid mass [ <i>lb</i> ]
$M_{ff}$	Fluid mass [ <i>lb</i> ]
$M_{fs}$	Movable solid mass [ <i>lb</i> ]
$\bar{n}$	Vector norm [-]
$p$	Pressure [ <i>psi</i> ]
$p_p$	Poro Pressure [ <i>psi</i> ]
$q$	Darcy's flow rate [ <i>ft/s</i> ]
$q_m$	Sink/Source term [ <i>1/s</i> ]
$r_w$	Well radius [ <i>ft</i> ]
$R$	Plastic zone radius [ <i>ft</i> ]
$S$	Stress tensor [ <i>psi</i> ]
$S_{ij}$	Stress in the <i>ij</i> direction [ <i>psi</i> ]
$t$	Time [ <i>hours</i> ]
$t_0$	Initial Time [ <i>hours</i> ]
$\bar{t}$	Traction vector [ <i>psi</i> ]
$u_i$	Displacement in the <i>i</i> direction [ <i>ft</i> ]
$\bar{u}$	Projection vector [ <i>adim</i> ]
$\bar{v}_x$	Interstitial velocity [ <i>ft/s</i> ]
$v$	Material velocity [ <i>ft/s</i> ]
$v_D$	Darcy velocity [ <i>ft/s</i> ]
$v_i^{ff}$	Fluid velocity [ <i>ft/s</i> ]
$v_i^{fs}$	Movable solids velocity [ <i>ft/s</i> ]

$v_i^s$	Solids velocity [ <i>ft/s</i> ]
$\bar{v}$	Mixture velocity [ <i>ft/s</i> ]
$\nu_p$	Poisson's ratio [-]
$V$	Total volume [ <i>ft</i> <sup>3</sup> ]
$V_s$	Solid volume [ <i>ft</i> <sup>3</sup> ]
$V_{fs}$	Movable solids volume [ <i>ft</i> <sup>3</sup> ]
$V_{ff}$	Fluid volume [ <i>ft</i> <sup>3</sup> ]
$V_v$	Porous space volume [ <i>ft</i> <sup>3</sup> ]
$V_\Omega$	Control system volume $\Omega$ [ <i>ft</i> <sup>3</sup> ]
$w$	Displacement in the <i>y</i> direction [ <i>ft</i> ]

### Greek Letters

$\alpha, \beta,$	Angle between two lines [°]
$\varepsilon_i$	Strain in the <i>i</i> direction [-]
$\varepsilon_{vol}$	Volumetric strain [-]
$\eta_k$	Kinematic viscosity [ <i>Poise</i> ]
$\theta$	Internal friction angle [°]
$\lambda_i$	Lamé's constant [-]
$\lambda$	Erosión coefficient [ <i>1/ft</i> ]
$\mu$	Dynamic viscosity [ <i>Sf</i> ]
$\mu_f$	Friction coefficient [-]
$\rho$	Density [ <i>lb/ft</i> <sup>3</sup> ]
$\rho_s$	Solid density [ <i>lb/ft</i> <sup>3</sup> ]

$\rho_{ff}$	Fluid density [lb/ft <sup>3</sup> ]
$\rho_{fs}$	Movable solid density [lb/ft <sup>3</sup> ]
$\bar{\rho}$	Mixture density [lb/ft <sup>3</sup> ]
$\sigma_1$	Maximum vertical stress [psi]
$\sigma'_3$	Minimum horizontal stress [psi]
$\sigma'_i$	Effective stress [psi]
$\sigma_h$	Hydrostatic stress [psi]
$\sigma_n$	Normal stress [psi]
$\sigma_r$	Radial stress [psi]
$\sigma_\theta$	Tangential stress [psi]
$\sigma_{ij}$	Stress in the $i j$ direction [psi]
$\varphi$	Porosity [-]
$\tau_{ij}$	Shear stresses on the $i j$ plane [psi]
$\tau_m$	Average shear stress [psi]
$\tau_n$	Normal shear stress [psi]
$\Omega$	Control volume [ft <sup>3</sup> ]
$\delta \Omega$	Control surface [ft <sup>2</sup> ]
$\Gamma_{xy}$	Strain in the $xy$ direction [-]

# Appendix A

## Formulation of Spatial Discretization

For the binary operations handled by computers, only additions and subtractions exist. Other operations, such as multiplication, powers, division, etc., are derived from iterations of these two operations. Similarly, to obtain the derivative, a method is required to approximate the derivative in a computable way, ensuring that the approximate solution is as close as possible to the solution of the original function. The definition of the derivative is:

$$\frac{df}{dx} = \lim_{h \rightarrow 0} \frac{f(x+h) - f(x)}{h} \quad (\text{A. 1})$$

If the function is approximated by considering that  $h$  will be sufficiently small to approximate Eq. A.1:

$$\frac{df}{dx} \approx \frac{f(x+h) - f(x)}{h} \quad (\text{A. 2})$$

Eq. A.2 is in a format that is computable, but the error generated by this approximation is not known. In general, the error represents the difference between the real and the measured value, so if the derivative is approximated at a point and the approximation is denoted as:

$$f'(x_i) \approx \frac{\delta f}{\delta x}(x_i) \quad (\text{A. 3})$$

Therefore, the approximation error is:

$$\epsilon(x_i) = f'(x_i) - \frac{\delta f}{\delta x}(x_i) \quad (\text{A. 4})$$

The goal is to quantify the error generated if Eq. A.2 is used. To do this, the derivative of the function  $f$  is approximated using a series of continuous equations. The Taylor series is used to approximate functions based on polynomials. The Taylor series is expressed as follows:

$$f(x) = f_i + f'_i(x - x_i) + \frac{f_i^{(2)}}{2}(x - x_i)^2 + \dots + \frac{f_i^{(n)}}{n!}(x - x_i)^2 \quad (\text{A. 5})$$

In Eq. A.5,  $f_i$  denotes the function evaluated at the point  $x_i$  and similarly with the derivatives. If Eq. A.5 is used to calculate  $f_{i+1}$  and is considered that  $h = x_{i+1} - x_i$  we have:

$$f_{i+1} = f_i + f'_i(x - x_i) + \frac{f_i^{(2)}}{2}(x - x_i)^2 + \dots + \frac{f_i^{(n)}}{n!}(x - x_i)^2 \quad (\text{A. 6})$$

Solving for the derivative from Eq. A.6, we have:

$$f'_i = \frac{f_{i+1} - f_i}{h} - \frac{f_i^2}{2}h - \dots - \frac{f_i^n}{2}h^{n-1} \quad (\text{A. 7})$$

If the error definition A.4 is used for Eqs. A.2 and A.7, we obtain the following:

$$\epsilon = \frac{f_i^2}{2}h - \dots - \frac{f_i^n}{2}h^{n-1} \quad (\text{A. 8})$$

Note from Eq. A.8 that, since there is no control over the coefficients, the error depends on  $h$ , and the highest value will be  $h$ , as if it is a term less than 1, the powers will only make it smaller. That said, the dominant term will be the  $h$  term, and the error will be of the order of  $h$ :

$$\epsilon = O(h) \quad (\text{A. 9})$$

And this new Eq. A.9 will be the truncation error obtained, and Eq. A.7 becomes:

$$f'_i = \frac{f_{i+1} - f_i}{h} + O(h) \quad (\text{A. 10})$$

$$f'_i \approx \frac{f_{i+1} - f_i}{h} \quad (\text{A. 11})$$

Eq. A.11 is known as the forward finite difference approximation. Similarly, the centered difference equation, which is established in Eq. 4.3.1, can be obtained. Therefore, the approximation for  $f'_{i-1}$  is sought, we have:

$$f_{i-1} = f_i + f'_i h + \frac{f_i^2}{2}h^2 + \dots + \frac{f_i^n}{n!}h^n \quad (\text{A. 12})$$

If eq. A.7 and A.12 are combined, we have:

$$f_{i+1} - f_{i-1} = 2hf'_i + 2\frac{f_i^3}{6}h^3 + \dots \quad (\text{A. 13})$$

Solving for  $f'_i$  from Eq. A.12, we have:

$$f'_i \approx \frac{f_{i+1} - f_{i-1}}{2h} + O(h^2) \quad (\text{A. 14})$$

Eq. A.14 represents Eq. 4.31. For this scheme, known as centered differences, the approximation error is  $h^2$ , so this scheme has less error compared to forward differences. Schemes A.11 and A.14 are used to discretize the main variable with respect to space, so that the partial derivatives of a main variable with respect to space are solved using these schemes.

The finite difference method converts derivatives into a series of discrete operations such as additions, subtractions, multiplications, and divisions. This allows the equations to be computable and solvable numerically.

# Appendix B

## Formulation of Temporal Discretization

Just like the partial derivatives with respect to space, the partial derivatives with respect to time must also be discretized. The mathematical operation is similar, but the variables considered are different. It is worth noting that in Appendix A, the variables considered to solve the problem are of the same type but at different spatial nodes; in this case, they will be considered at discrete time intervals. Suppose we have the following differential equation:

$$\frac{dy}{dt} = f(t, y); y(t_0) = y_0; t \in [t_0, t_f] \quad (\text{B. 1})$$

The function  $y(t)$  must be found such that  $y(t_0) = t_0$ , which satisfies the condition of the ordinary differential equation for time in the interval  $t \in [t_0, t_f]$ . If the continuous variable  $t$  is discretized into intervals where all times are considered, where  $t_{Nt} = t_f$ :

$$y = [y(t_0), y(t_1) \dots y(t_{Nt-1}), y(t_{Nt})] \quad (\text{B. 2})$$

Then, considering vector B.0.2 and considering the following notation  $y_j = y(t_j)$  where  $j = 1, 2, \dots, Nt$ .

### B.1. Explicit Euler

The explicit Euler method is the simplest method.:

$$\int_{t_j}^{t_{j+1}} \frac{dy}{dt} dt = \int_{t_j}^{t_{j+1}} f(t, y(t)) dt \quad (\text{B. 1. 1})$$

$$y_{j+1} - y_j = \int_{t_j}^{t_{j+1}} f(t, y(t)) dt \quad (\text{B. 1. 2})$$

he explicit Euler method is the simplest method. It involves integrating the right-hand side of equation B.1.2 in a discrete form:

$$\int_{t_j}^{t_{j+1}} f(t, y(t)) dt \approx f(t_j, y_j) \Delta t_j \quad (\text{B. 1. 3})$$

where  $\Delta t_j = t_{j+1} - t_j$ . If it is necessary to determine the error associated with using equation (B.1.3), the function  $y(t)$  is expanded using Taylor series as follows:

$$y(t) = y(t_j) + (t - t_j) \frac{dy}{dt}(t_j) + \frac{(t - t_j)^2}{2} \frac{d^2y}{dt^2}(t_j) + \dots \quad (\text{B. 1. 4})$$

Solving  $y(t)$  from equation (B.1.4) and substituting it into equation (B.1.3) yields the following:

$$y(t) \approx y(t_j) + (t - t_j)f(t_j, y_j) \quad (\text{B. 1. 5})$$

Finding the solution for time  $t_{j+1}$ , we have:

$$y(t_{j+1}) = y(t_j) + f(t_j, y_j)\Delta t_j \quad (\text{B. 1. 6})$$

Where  $\Delta t_j = t_{j+1} - t_j$

Note that on the right-hand side of Eq. (B.1.6), no terms from the next time step are included; practically all terms are at the same time step, which are known when the first-time step is proposed. Although this method is very simple to solve, it tends to be conditionally stable, meaning that the method is stable only for certain values of  $\Delta t$ .

## B.2. Implicit Euler

The implicit Euler method is like the explicit method, but the change it introduces is quite radical and significantly influences the numerical stability of the solution. Thus, Eq. B.1.3 becomes:

$$\int_{t_j}^{t_{j+1}} f(t, y(t))dt \approx f(t_{j+1}, y_{j+1})\Delta t_j \quad (\text{B. 2. 1})$$

Note that now the function variables are at time  $j + 1$ . This suggests that the Taylor series expansion changes to:

$$y(t) = y(t_{j+1}) + (t - t_{j+1}) \frac{dy}{dt}(t_{j+1}) + \frac{(t - t_{j+1})^2}{2} \frac{d^2y}{dt^2}(t_{j+1}) + \dots \quad (\text{B. 2. 2})$$

Truncating the series B.2.2 and evaluating it at  $t = t_j$  yields the following:

$$y(t_j) = y(t_{j+1}) + (t_j - t_{j+1}) \frac{dy}{dt}(t_{j+1}) \quad (\text{B. 2. 3})$$

Alternatively, in a similar manner to Eq. B.1.6, we have:

$$y(t_{j+1}) = y(t_j) + f(t_{j+1}, y_{j+1})\Delta t_j \quad (\text{B. 2. 4})$$

Note that on the right-hand side of Eq. B.2.4, the variables  $t_{j+1}$  and  $y_{j+1}$  are at the next time step. This presents a problem, especially when the equation is nonlinear, due to algebraic manipulation and the fact that the variables at the next time step are unknowns. The great advantage of this method is its stability. Unlike the explicit Euler method, this method is unconditionally stable, which means that its behavior does not change with different values of  $\Delta t_j$ . It is only necessary to ensure that the values of  $\Delta t_j$  are small enough to achieve convergence. The fact that there are three nonlinear equations with three main variables indicates that this method is suitable for this problem, as it helps to avoid stability issues when choosing the time step values.

# Appendix C

## Jacobian Matrix

Observing Eq. 4.5.13, it is noted that we have an equation of the form  $[A]\{\vec{b}\} = \{\vec{x}\}$ ; It is necessary to determine the value of the elements of Matrix  $A$  and vector  $\vec{x}$  to obtain the result of vector  $\vec{b}$ , where  $i$  represents rows and  $j$  represents columns.

**Derivative**  $\frac{\partial R_i^{1^n}}{\partial \varphi_j}$ :

Node  $i = 1, j = 1$

$$\frac{\partial R_1^{1^n}}{\partial \varphi_1} = \frac{c_1^{n+1} - c_1^n}{\Delta t} + \left( -\frac{k_0}{\eta_k[(1 - c_i^{n+1})\rho_f + c_i^{n+1}\rho_s]} \frac{p_{i+1}^{n+1} - p_i^{n+1}}{\Delta r_i} \right) \left( \frac{(\varphi_1^{n+1} - 3)\varphi_1^{n+1^2}}{(\varphi_1^{n+1} - 1)^3} \right) \dots \frac{c_2^{n+1} - c_1^{n+1}}{\Delta r_i} - \frac{1}{\Delta t} \quad (\text{C. 1})$$

Node  $i = 1, j = 2$

$$\frac{\partial R_1^{1^n}}{\partial \varphi_2} = 0 \quad (\text{C. 2})$$

Node  $i = 2, \dots, Nr - 1, j = i - 1$

$$\frac{\partial R_1^{1^n}}{\partial \varphi_{i-1}} = 0 \quad (\text{C. 3})$$

Node  $i = 2, \dots, Nr - 1, j = i$

$$\frac{\partial R_i^{1^n}}{\partial \varphi_i} = \frac{c_i^{n+1} - c_i^n}{\Delta t} + \left( -\frac{k_0}{\eta_k[(1 - c_i^{n+1})\rho_f + c_i^{n+1}\rho_s]} \frac{p_{i+1}^{n+1} - p_i^{n+1}}{\Delta r_i} \right) \left( \frac{(\varphi_i^{n+1} - 3)\varphi_i^{n+1^2}}{(\varphi_i^{n+1} - 1)^3} \right) \dots \frac{c_{i+1}^{n+1} - c_i^{n+1}}{\Delta r_i} - \frac{1}{\Delta t} \quad (\text{C.4})$$

Node  $i = 2, \dots, Nr - 1, j = i + 1$

$$\frac{\partial R_i^{1^n}}{\partial \varphi_{i+1}} = 0 \quad (\text{C. 5})$$

Node  $i = Nr, j = Nr - 1$

$$\frac{\partial R_{Nr}^{1^n}}{\partial \varphi_{Nr}} = 0 \quad (\text{C. 6})$$

Node  $i = Nr, j = Nr$

$$\frac{\partial R_{Nr}^{1^n}}{\partial \varphi_{Nr}} = \frac{c_{Nr}^{n+1} - c_{Nr}^n}{\Delta t} + \quad (C. 7)$$

$$\left( -\frac{k_0}{\eta_k [(1 - c_{Nr}^{n+1}) \rho_f + c_{Nr}^{n+1} \rho_s]} \frac{p_e - p_{Nr}^{n+1}}{\Delta r_{Nr}} \right) \left( \frac{(\varphi_{Nr}^{n+1} - 3) \varphi_{Nr}^{n+1^2}}{(\varphi_{Nr}^{n+1} - 1)^3} \right) \dots \frac{c_e - c_{Nr}^{n+1}}{\Delta r_{Nr}} - \frac{1}{\Delta t}$$

**Derivative**  $\frac{\partial R_i^{1^n}}{\partial c_i}$ :

Node  $i = 1, j = 1$

$$\frac{\partial R_1^{1^n}}{\partial c_1} = \frac{\varphi_1^{n+1} - \varphi_1^n}{\Delta t} + \left( \frac{k_0 \varphi_1^{n+1^3}}{(1 - \varphi_1^{n+1})^2 \eta_k} \frac{p_2^{n+1} - p_1^{n+1}}{\Delta r_1} \right) \left( \frac{\rho_f - \rho_s}{((\rho_s - \rho_f) c_1^{n+1} + \rho_f)^2} \right) \frac{1}{\Delta r_1} \quad (C. 8)$$

Node  $i = 1, j = 2$

$$\frac{\partial R_1^{1^n}}{\partial c_2} = \left( -\frac{k_0 \varphi_1^{n+1^3}}{(1 - \varphi_1^{n+1})^2 \eta_k [(1 - c_1^{n+1}) \rho_f + c_1^{n+1} \rho_s]} \frac{p_2^{n+1} - p_1^{n+1}}{\Delta r_1} \right) \frac{1}{\Delta r_1} \quad (C. 9)$$

Node  $i = 2, \dots, Nr - 1, j = i - 1$

$$\frac{\partial R_i^{1^n}}{\partial c_{i-1}} = 0 \quad (C. 10)$$

Node  $i = 2, \dots, Nr - 1, j = i$

$$\frac{\partial R_i^{1^n}}{\partial c_i} = \frac{\varphi_i^{n+1} - \varphi_i^n}{\Delta t} + \left( \frac{k_0 \varphi_i^{n+1^3}}{(1 - \varphi_i^{n+1})^2 \eta_k} \frac{p_{i+1}^{n+1} - p_i^{n+1}}{\Delta r_i} \right) \left( \frac{\rho_f - \rho_s}{((\rho_s - \rho_f) c_i^{n+1} + \rho_f)^2} \right) \frac{1}{\Delta r_i} \quad (C. 11)$$

Node  $i = 2, \dots, Nr - 1, j = i + 1$

$$\frac{\partial R_i^{1^n}}{\partial c_{i+1}} = \left( -\frac{k_0 \varphi_i^{n+1^3}}{(1 - \varphi_i^{n+1})^2 \eta_k [(1 - c_{i+1}^{n+1}) \rho_f + c_{i+1}^{n+1} \rho_s]} \frac{p_{i+1}^{n+1} - p_i^{n+1}}{\Delta r_i} \right) \frac{1}{\Delta r_i} \quad (C. 12)$$

Node  $i = Nr - 1$

$$\frac{\partial R_i^{1^n}}{\partial c_{Nr-1}} = 0 \quad (C. 13)$$

Node  $i = Nr, j = Nr$

$$\frac{\partial R_{Nr}^{1^n}}{\partial c_{Nr}} = \frac{\varphi_{Nr}^{n+1} - \varphi_{Nr}^n}{\Delta t} + \left( \frac{k_0 \varphi_{Nr}^{n+1^3}}{(1 - \varphi_{Nr}^{n+1})^2 \eta_k} \frac{p_e - p_{Nr}^{n+1}}{\Delta r_{Nr}} \right) \left( \frac{\rho_f - \rho_s}{((\rho_s - \rho_f) c_{Nr}^{n+1} + \rho_f)^2} \right) \frac{1}{\Delta r_{Nr}} \quad (C. 14)$$

**Derivative**  $\frac{\partial R_i^{1n}}{\partial p_i}$ :

Node  $i = 1, j = 1$

$$\frac{\partial R_1^{1n}}{\partial p_1} = \left( \frac{k_0 \varphi_1^{n+1^3}}{(1 - \varphi_1^{n+1})^2 \eta_k [(1 - c_1^{n+1}) \rho_f + c_1^{n+1} \rho_s]} \frac{1}{\Delta r_1} \right) \frac{c_2^{n+1} - c_1^{n+1}}{\Delta r_1} \quad (\text{C. 15})$$

Node  $i = 1, j = 2$

$$\frac{\partial R_1^{1n}}{\partial p_2} = \left( - \frac{k_0 \varphi_1^{n+1^3}}{(1 - \varphi_1^{n+1})^2 \eta_k [(1 - c_1^{n+1}) \rho_f + c_1^{n+1} \rho_s]} \right) \frac{c_2^{n+1} - c_1^{n+1}}{\Delta r_1} \quad (\text{C. 16})$$

Node  $i = 2, \dots, Nr - 1, j = i - 1$

$$\frac{\partial R_i^{1n}}{\partial p_{i-1}} = 0 \quad (\text{C. 17})$$

Node  $i = 2, \dots, Nr - 1, j = i$

$$\frac{\partial R_i^{1n}}{\partial p_i} = \left( - \frac{k_0 \varphi_i^{n+1^3}}{(1 - \varphi_i^{n+1})^2 \eta_k [(1 - c_i^{n+1}) \rho_f + c_i^{n+1} \rho_s]} \frac{1}{\Delta r_i} \right) \frac{c_{i+1}^{n+1} - c_i^{n+1}}{\Delta r_i} \quad (\text{C. 18})$$

Node  $i = 2, \dots, Nr - 1, j = i + 1$

$$\frac{\partial R_i^{1n}}{\partial p_{i+1}} = \left( - \frac{k_0 \varphi_i^{n+1^3}}{(1 - \varphi_i^{n+1})^2 \eta_k [(1 - c_i^{n+1}) \rho_f + c_i^{n+1} \rho_s]} \frac{1}{\Delta r_i} \right) \frac{c_{i+1}^{n+1} - c_i^{n+1}}{\Delta r_i} \quad (\text{C. 19})$$

Node  $i = Nr, j = Nr - 1$

$$\frac{\partial R_{Nr}^{1n}}{\partial p_{Nr}} = 0 \quad (\text{C. 20})$$

Node  $i = Nr, j = Nr$

$$\frac{\partial R_{Nr}^{1n}}{\partial p_{Nr}} = \left( - \frac{k_0 \varphi_{Nr}^{n+1^3}}{(1 - \varphi_{Nr}^{n+1})^2 \eta_k [(1 - c_{Nr}^{n+1}) \rho_f + c_{Nr}^{n+1} \rho_s]} \frac{1}{\Delta r_{Nr}} \right) \frac{c_e - c_{Nr}^{n+1}}{\Delta r_{Nr}} \quad (\text{C. 21})$$

**Derivative**  $\frac{\partial R_i^{2n}}{\partial \varphi_i}$ :

Node  $i = 1, j = 1$

$$\begin{aligned} \frac{\partial R_1^{2n}}{\partial \varphi_1} = & \frac{1}{\Delta t} + \lambda \left( c_1^{n+1} - \frac{c_1^{n+1^2}}{c_{cr1}} \right) \left( \frac{k_0 \varphi_1^{n+1^3}}{(1 - \varphi_1^{n+1})^2 \eta_k [(1 - c_1^{n+1}) \rho_f + c_1^{n+1} \rho_s]} \frac{p_2^{n+1} - p_1^{n+1}}{\Delta r_1} \right) - \\ & \lambda (1 - \varphi_1^{n+1}) \left( c_1^{n+1} - \frac{c_1^{n+1^2}}{c_{cr1}} \right) \left( \frac{(\varphi_1^{n+1} - 3) \varphi_1^{n+1^2}}{(\varphi_1^{n+1} - 1)^3} \right) \left( \frac{k_0}{\eta_k [(1 - c_1^{n+1}) \rho_f + c_1^{n+1} \rho_s]} \frac{p_2^{n+1} - p_1^{n+1}}{\Delta r_1} \right) \end{aligned} \quad (\text{C. 22})$$

Node  $i = 1, j = 2$

$$\frac{\partial R_1^{2n}}{\partial \varphi_2} = 0 \quad (\text{C. 23})$$

Node  $i = 2, \dots, Nr - 1, j = i - 1$

$$\frac{\partial R_i^{2^n}}{\partial \varphi_{i-1}} = 0 \quad (\text{C. 24})$$

Node  $i = 2, \dots, Nr - 1, j = i$

$$\begin{aligned} & \frac{p_2^{n+1} - 2p_1^{n+1} + p_{wf}}{\Delta r_1^2} + \frac{p_2^{n+1} - p_{wf}}{2\Delta r_1} \left[ \frac{1}{r_1} + \left( \frac{3 - \varphi_1^{n+1}}{\varphi_1^{n+1}(1 - \varphi_1^{n+1})} \right) \frac{\varphi_2^{n+1} - 1}{2\Delta r_1} + \right. \\ & \left. \left( \frac{\rho_f - \rho_s}{(1 - c_1^{n+1})\rho_f + c_1^{n+1}\rho_s} \right) \frac{c_2^{n+1} - 1}{2\Delta r_1} \right] = 0 \end{aligned} \quad (\text{C. 25})$$

$$\begin{aligned} \frac{\partial R_i^{2^n}}{\partial \varphi_i} &= \frac{1}{\Delta t} + \lambda \left( c_i^{n+1} - \frac{c_i^{n+1^2}}{c_{cri}} \right) \left( \frac{k_0 \varphi_i^{n+1^3}}{(1 - \varphi_i^{n+1})^2 \eta_k [(1 - c_i^{n+1})\rho_f + c_i^{n+1}\rho_s]} \frac{p_{i+1}^{n+1} - p_i^{n+1}}{\Delta r_i} \right) - \\ & \lambda (1 - \varphi_i^{n+1}) \left( c_i^{n+1} - \frac{c_i^{n+1^2}}{c_{cri}} \right) \left( \frac{(\varphi_i^{n+1} - 3)\varphi_i^{n+1^2}}{(\varphi_i^{n+1} - 1)^3} \right) \left( \frac{k_0}{\eta_k [(1 - c_i^{n+1})\rho_f + c_i^{n+1}\rho_s]} \frac{p_{i+1}^{n+1} - p_i^{n+1}}{\Delta r_i} \right) \end{aligned}$$

Node  $i = 2, \dots, Nr - 1, j = i + 1$

$$\frac{\partial R_i^{2^n}}{\partial \varphi_{i+1}} = 0 \quad (\text{C. 26})$$

Node  $i = Nr, j = Nr - 1$

$$\frac{\partial R_{Nr}^{2^n}}{\partial \varphi_{Nr-1}} = 0 \quad (\text{C. 27})$$

Node  $i = Nr, j = Nr$

$$\begin{aligned} \frac{\partial R_{Nr}^{2^n}}{\partial \varphi_{Nr}} &= \frac{1}{\Delta t} + \lambda \left( c_{Nr}^{n+1} - \frac{c_{Nr}^{n+1^2}}{c_{cNr}} \right) \left( \frac{k_0 \varphi_{Nr}^{n+1^3}}{(1 - \varphi_{Nr}^{n+1})^2 \eta_k [(1 - c_{Nr}^{n+1})\rho_f + c_{Nr}^{n+1}\rho_s]} \frac{p_e - p_{Nr}^{n+1}}{\Delta r_{Nr}} \right) - \\ & \lambda (1 - \varphi_{Nr}^{n+1}) \left( c_{Nr}^{n+1} - \frac{c_{Nr}^{n+1^2}}{c_{cNr}} \right) \left( \frac{(\varphi_{Nr}^{n+1} - 3)\varphi_{Nr}^{n+1^2}}{(\varphi_{Nr}^{n+1} - 1)^3} \right) \left( \frac{k_0}{\eta_k [(1 - c_{Nr}^{n+1})\rho_f + c_{Nr}^{n+1}\rho_s]} \frac{p_e - p_{Nr}^{n+1}}{\Delta r_{Nr}} \right) \end{aligned} \quad (\text{C. 28})$$

**Derivative**  $\frac{\partial R_i^{2^n}}{\partial c_i}$

Node  $i = 1, j = 1$

$$\begin{aligned} \frac{\partial R_1^{2^n}}{\partial c_1} &= -\lambda (1 - \varphi_1^{n+1}) \left( 1 - \frac{2c_1^{n+1}}{c_{cr1}} \right) \left( \frac{k_0 \varphi_1^{n+1^3}}{(1 - \varphi_1^{n+1})^2 \eta_k [(1 - c_1^{n+1})\rho_f + c_1^{n+1}\rho_s]} \frac{p_2^{n+1} - p_1^{n+1}}{\Delta r_1} \right) - \\ & \lambda (1 - \varphi_1^{n+1}) \left( c_1^{n+1} - \frac{c_1^{n+1^2}}{c_{cr1}} \right) \left( \frac{\rho_f - \rho_s}{((\rho_s - \rho_f)c_1^{n+1} + \rho_f)^2} \right) \left( \frac{k_0 \varphi_1^{n+1^3}}{\eta_k (1 - \varphi_1^{n+1})} \frac{p_2^{n+1} - p_1^{n+1}}{\Delta r_1} \right) \end{aligned} \quad (\text{C. 29})$$

Node  $i = 1, j = 2$

$$\frac{\partial R_1^{2^n}}{\partial c_2} = 0 \quad (\text{C. 30})$$

Node  $i = 2, \dots, Nr - 1, j = i - 1$

$$\frac{\partial R_1^{2n}}{\partial c_{i-1}} = 0 \quad (\text{C. 31})$$

Node  $i = 2, \dots, Nr - 1, j = i$

$$\begin{aligned} \frac{\partial R_1^{2n}}{\partial c_i} = & -\lambda(1 - \varphi_i^{n+1}) \left(1 - \frac{2c_i^{n+1}}{c_{cri}}\right) \left(\frac{k_0 \varphi_i^{n+1^3}}{(1 - \varphi_i^{n+1})^2 \eta_k [(1 - c_i^{n+1}) \rho_f + c_i^{n+1} \rho_s]} \frac{p_{i+1}^{n+1} - p_i^{n+1}}{\Delta r_i}\right) - \\ & \lambda(1 - \varphi_i^{n+1}) \left(c_i^{n+1} - \frac{c_i^{n+1^2}}{c_{cri}}\right) \left(\frac{\rho_f - \rho_s}{((\rho_s - \rho_f) c_i^{n+1} + \rho_f)^2}\right) \left(\frac{k_0 \varphi_i^{n+1^3}}{\eta_k (1 - \varphi_i^{n+1})} \frac{p_{i+1}^{n+1} - p_i^{n+1}}{\Delta r_i}\right) \end{aligned} \quad (\text{C. 32})$$

Node  $i = 2, \dots, Nr - 1, j = i + 1$

$$\frac{\partial R_1^{2n}}{\partial c_{i+1}} = 0 \quad (\text{C. 33})$$

Node  $i = Nr, j = Nr - 1$

$$\frac{\partial R_{Nr}^{2n}}{\partial c_{Nr}} = 0 \quad (\text{C. 34})$$

Node  $i = Nr, j = Nr$

$$\begin{aligned} \frac{\partial R_{Nr}^{2n}}{\partial c_{Nr}} = & -\lambda(1 - \varphi_{Nr}^{n+1}) \left(1 - \frac{2c_{Nr}^{n+1}}{c_{crNr}}\right) \left(\frac{k_0 \varphi_{Nr}^{n+1^3}}{(1 - \varphi_{Nr}^{n+1})^2 \eta_k [(1 - c_{Nr}^{n+1}) \rho_f + c_{Nr}^{n+1} \rho_s]} \frac{p_e - p_{Nr}^{n+1}}{\Delta r_{Nr}}\right) - \\ & \lambda(1 - \varphi_{Nr}^{n+1}) \left(c_{Nr}^{n+1} - \frac{c_{Nr}^{n+1^2}}{c_{crNr}}\right) \left(\frac{\rho_f - \rho_s}{((\rho_s - \rho_f) c_{Nr}^{n+1} + \rho_f)^2}\right) \left(\frac{k_0 \varphi_{Nr}^{n+1^3}}{\eta_k (1 - \varphi_{Nr}^{n+1})} \frac{p_e - p_{Nr}^{n+1}}{\Delta r_{Nr}}\right) \end{aligned} \quad (\text{C. 35})$$

**Derivative**  $\frac{\partial R_i^{2n}}{\partial p_i}$

Node  $i = 1, j = 1$

$$\begin{aligned} \frac{\partial R_1^{2n}}{\partial p_1} = & \lambda(1 - \varphi_1^{n+1}) (c_1^{n+1} \\ & - \frac{c_1^{n+1^2}}{c_{cr1}}) \left(\frac{k_0 \varphi_1^{n+1^3}}{(1 - \varphi_1^{n+1})^2 \eta_k [(1 - c_1^{n+1}) \rho_f + c_1^{n+1} \rho_s]} \frac{1}{\Delta r_1}\right) \end{aligned} \quad (\text{C. 36})$$

Node  $i = 1, j = 2$

$$\begin{aligned} \frac{\partial R_1^{2n}}{\partial p_2} = & -\lambda(1 - \varphi_1^{n+1}) (c_1^{n+1} \\ & - \frac{c_1^{n+1^2}}{c_{cr1}}) \left(\frac{k_0 \varphi_1^{n+1^3}}{(1 - \varphi_1^{n+1})^2 \eta_k [(1 - c_1^{n+1}) \rho_f + c_1^{n+1} \rho_s]} \frac{1}{\Delta r_1}\right) \end{aligned} \quad (\text{C. 37})$$

Node  $i = 2, \dots, Nr - 1, j = i - 1$

$$\frac{\partial R_i^{2n}}{\partial p_{i-1}} = 0 \quad (\text{C. 38})$$

Node  $i = 2, \dots, Nr - 1, j = i$

$$\frac{\partial R_i^{2^n}}{\partial p_i} = \lambda(1 - \varphi_i^{n+1})(c_i^{n+1} - \frac{c_i^{n+1^2}}{c_{cr_i}}) \left( \frac{k_0 \varphi_i^{n+1^3}}{(1 - \varphi_i^{n+1})^2 \eta_k [(1 - c_i^{n+1}) \rho_f + c_i^{n+1} \rho_s]} \frac{1}{\Delta r_i} \right) \quad (C. 39)$$

Node  $i = 2, \dots, Nr - 1, j = i + 1$

$$\frac{\partial R_i^{2^n}}{\partial p_{i+1}} = -\lambda(1 - \varphi_i^{n+1})(c_i^{n+1} - \frac{c_i^{n+1^2}}{c_{cr_i}}) \left( \frac{k_0 \varphi_i^{n+1^3}}{(1 - \varphi_i^{n+1})^2 \eta_k [(1 - c_i^{n+1}) \rho_f + c_i^{n+1} \rho_s]} \frac{1}{\Delta r_i} \right) \quad (C. 40)$$

Node  $i = Nr, j = Nr - 1$

$$\frac{\partial R_{Nr}^{2^n}}{\partial p_{Nr-1}} = 0 \quad (C. 41)$$

Node  $i = Nr, j = Nr$

$$\frac{\partial R_{Nr}^{2^n}}{\partial p_{Nr}} = \lambda(1 - \varphi_{Nr}^{n+1})(c_{Nr}^{n+1} - \frac{c_{Nr}^{n+1^2}}{c_{cr_{Nr}}}) \left( \frac{k_0 \varphi_{Nr}^{n+1^3}}{(1 - \varphi_{Nr}^{n+1})^2 \eta_k [(1 - c_{Nr}^{n+1}) \rho_f + c_{Nr}^{n+1} \rho_s]} \frac{1}{\Delta r_{Nr}} \right) \quad (C. 42)$$

**Derivative**  $\frac{\partial R_i^{3^n}}{\partial \varphi_i}$

Node  $i = 1, j = 1$

$$\frac{\partial R_1^{3^n}}{\partial \varphi_1} = -\frac{p_2^{n+1} - p_{wf}^{n+1}}{2\Delta r_i} \left[ \left( \frac{\varphi_1^{n+1^2} - 6\varphi_1^{n+1} + 3}{(1 - \varphi_1^{n+1})^2 \varphi_1^{n+1^2}} \right) \frac{\varphi_2^{n+1} - \varphi_0^{n+1}}{2\Delta r_i} \right] \quad (C. 43)$$

Node  $i = 1, j = 2$

$$\frac{\partial R_1^{3^n}}{\partial \varphi_2} = -\frac{p_2^{n+1} - p_{wf}^{n+1}}{2\Delta r_i} \left[ \left( \frac{3 - \varphi_1^{n+1}}{\varphi_1^{n+1} (1 - \varphi_1^{n+1})} \right) \frac{1}{2\Delta r_i} \right] \quad (C. 44)$$

Node  $i = 2, \dots, Nr - 1, j = i - 1$

$$\frac{\partial R_i^{3^n}}{\partial \varphi_{i-1}} = -\frac{p_2^{n+1} - p_{wf}^{n+1}}{2\Delta r_i} \left[ \left( \frac{\varphi_1^{n+1^2} - 6\varphi_1^{n+1} + 3}{(1 - \varphi_1^{n+1})^2 \varphi_1^{n+1^2}} \right) \frac{1}{2\Delta r_i} \right] \quad (C. 45)$$

Node  $i = 2, \dots, Nr - 1, j = i$

$$\frac{\partial R_i^{3^n}}{\partial \varphi_i} = -\frac{p_{i+1}^{n+1} - p_{i-1}^{n+1}}{2\Delta r_i} \left[ \left( \frac{\varphi_i^{n+1} - 6\varphi_i^{n+1} + 3}{(1 - \varphi_i^{n+1})^2 \varphi_i^{n+1}} \right) \frac{\varphi_{i+1}^{n+1} - \varphi_{i-1}^{n+1}}{2\Delta r_i} \right] \quad (\text{C. 46})$$

Node  $i = 2, \dots, Nr - 1, j = i + 1$

$$\frac{\partial R_i^{3^n}}{\partial \varphi_{i+1}} = -\frac{p_{i+1}^{n+1} - p_{i-1}^{n+1}}{2\Delta r_i} \left[ \left( \frac{3 - \varphi_i^{n+1}}{\varphi_i^{n+1}(1 - \varphi_i^{n+1})} \right) \frac{1}{2\Delta r_i} \right] \quad (\text{C. 47})$$

Node  $i = Nr, j = Nr - 1$

$$\frac{\partial R_{Nr}^{3^n}}{\partial \varphi_{Nr-1}} = -\frac{p_e - p_{Nr-1}^{n+1}}{2\Delta r_{Nr}} \left[ \left( \frac{\varphi_{Nr}^{n+1} - 6\varphi_{Nr}^{n+1} + 3}{(1 - \varphi_{Nr}^{n+1})^2 \varphi_{Nr}^{n+1}} \right) \frac{1}{2\Delta r_{Nr}} \right] \quad (\text{C. 48})$$

Node  $i = Nr, j = Nr$

$$\frac{\partial R_{Nr}^{3^n}}{\partial \varphi_{Nr}} = -\frac{p_e - p_{Nr}^{n+1}}{2\Delta r_{Nr}} \left[ \left( \frac{\varphi_{Nr}^{n+1} - 6\varphi_{Nr}^{n+1} + 3}{(1 - \varphi_{Nr}^{n+1})^2 \varphi_{Nr}^{n+1}} \right) \frac{\varphi_e - \varphi_{Nr-1}^{n+1}}{2\Delta r_{Nr}} \right] \quad (\text{C. 49})$$

**Derivative**  $\frac{\partial R_i^{3^n}}{\partial c_i}$

Node  $i = 1, j = 1$

$$\frac{\partial R_1^{3^n}}{\partial c_1} = -\frac{p_2^{n+1} - p_{wf}}{2\Delta r_1} \left[ \left( \frac{(\rho_s - \rho_f)^2}{((\rho_s - \rho_f)c_1^{n+1} + \rho_f)^2} \right) \frac{c_2^{n+1} - c_0^{n+1}}{2\Delta r_i} \right] \quad (\text{C. 50})$$

Node  $i = 1, j = 2$

$$\frac{\partial R_1^{3^n}}{\partial c_2} = -\frac{p_2^{n+1} - p_e}{2\Delta r_1} \left[ \left( \frac{\rho_s - \rho_f}{(1 - c_1^{n+1})\rho_f + c_1^{n+1}\rho_s} \right) \frac{1}{2\Delta r_1} \right] \quad (\text{C. 51})$$

Node  $i = 2, \dots, Nr - 1, j = i - 1$

$$\frac{\partial R_1^{3^n}}{\partial c_{i-1}} = -\frac{p_{i+1}^{n+1} - p_{i-1}^{n+1}}{2\Delta r_i} \left[ \left( \frac{\rho_s - \rho_f}{(1 - c_i^{n+1})\rho_f + c_i^{n+1}\rho_s} \right) \frac{1}{2\Delta r_i} \right] \quad (\text{C. 52})$$

Node  $i = 2, \dots, Nr - 1, j = i$

$$\frac{\partial R_i^{3^n}}{\partial c_i} = -\frac{p_{i+1}^{n+1} - p_{i-1}^{n+1}}{2\Delta r_i} \left[ \left( \frac{(\rho_s - \rho_f)^2}{((\rho_s - \rho_f)c_i^{n+1} + \rho_f)^2} \right) \frac{c_{i+1}^{n+1} - c_{i-1}^{n+1}}{2\Delta r_i} \right] \quad (\text{C. 53})$$

Node  $i = 2, \dots, Nr - 1, j = i + 1$

$$\frac{\partial R_i^{3^n}}{\partial c_{i-1}} = -\frac{p_{i+1}^{n+1} - p_{i-1}^{n+1}}{2\Delta r_i} \left[ \left( \frac{\rho_s - \rho_f}{(1 - c_i^{n+1})\rho_f + c_i^{n+1}\rho_s} \right) \frac{1}{2\Delta r_i} \right] \quad (\text{C. 54})$$

Node  $i = Nr, j = Nr - 1$

$$\frac{\partial R_{Nr}^{3^n}}{\partial c_{Nr-1}} = -\frac{p_e - p_{Nr-1}^{n+1}}{2\Delta r_{Nr}} \left[ \left( \frac{\rho_s - \rho_f}{(1 - c_{Nr}^{n+1})\rho_f + c_{Nr}^{n+1}\rho_s} \right) \frac{1}{2\Delta r_{Nr}} \right] \quad (\text{C. 55})$$

Node  $i = Nr, j = Nr$

$$\frac{\partial R_{Nr}^{3n}}{\partial c_{Nr}} = -\frac{p_e - p_{Nr}^{n+1}}{2\Delta r_{Nr}} \left[ \left( \frac{(\rho_s - \rho_f)^2}{((\rho_s - \rho_f)c_{Nr}^{n+1} + \rho_f)^2} \right) \frac{c_e - c_{Nr-1}^{n+1}}{2\Delta r_{Nr}} \right] \quad (C. 56)$$

**Derivative**  $\frac{\partial R_i^{3n}}{\partial p_i}$

$$\frac{p_{i+1}^{n+1} - 2p_i^{n+1} + p_{i-1}^{n+1}}{\Delta r_i^2} + \frac{p_{i+1}^{n+1} - p_{i-1}^{n+1}}{2\Delta r_i} \left[ \frac{1}{r_i} + \left( \frac{3 - \varphi_i^{n+1}}{\varphi_i^{n+1}(1 - \varphi_i^{n+1})} \right) \frac{\varphi_{i+1}^{n+1} - \varphi_{i-1}^{n+1}}{2\Delta r_i} + \left( \frac{\rho_f - \rho_s}{(1 - c_i^{n+1})\rho_f + c_i^{n+1}\rho_s} \right) \frac{c_{i-1}^{n+1} - c_{i-1}^{n+1}}{2\Delta r_i} \right] \quad (C. 57)$$

Node  $i = 1, j = 1$

$$\frac{\partial R_1^{3n}}{\partial p_1} = \frac{-2}{\Delta r_1^2} \quad (C. 58)$$

Node  $i = 1, j = 2$

$$\frac{\partial R_1^{3n}}{\partial p_1} = \frac{1}{\Delta r_1^2} + \frac{1}{2\Delta r_1} \left[ \frac{1}{r_1} + \left( \frac{3 - \varphi_1^{n+1}}{\varphi_1^{n+1}(1 - \varphi_1^{n+1})} \right) \frac{\varphi_2^{n+1} - \varphi_0^{n+1}}{2\Delta r_1} + \left( \frac{\rho_f - \rho_s}{(1 - c_1^{n+1})\rho_f + c_1^{n+1}\rho_s} \right) \frac{c_2^{n+1} - c_0^{n+1}}{2\Delta r_1} \right] \quad (C. 59)$$

Node  $i = 2, \dots, Nr - 1, j = i - 1$

$$\frac{\partial R_i^{3n}}{\partial p_{i-1}} = \frac{1}{\Delta r_i^2} + \frac{1}{2\Delta r_i} \left[ \frac{1}{r_i} + \left( \frac{3 - \varphi_i^{n+1}}{\varphi_i^{n+1}(1 - \varphi_i^{n+1})} \right) \frac{\varphi_{i+1}^{n+1} - \varphi_{i-1}^{n+1}}{2\Delta r_i} + \left( \frac{\rho_f - \rho_s}{(1 - c_i^{n+1})\rho_f + c_i^{n+1}\rho_s} \right) \frac{c_{i+1}^{n+1} - c_{i-1}^{n+1}}{2\Delta r_i} \right] \quad (C. 60)$$

Node  $i = 2, \dots, Nr - 1, j = i$

$$\frac{\partial R_i^{3n}}{\partial p_i} = \frac{-2}{\Delta r_i^2} \quad (C. 61)$$

Node  $i = 2, \dots, Nr - 1, j = i + 1$

$$\frac{\partial R_i^{3n}}{\partial p_{i+1}} = \frac{1}{\Delta r_i^2} + \frac{1}{2\Delta r_i} \left[ \frac{1}{r_i} + \left( \frac{3 - \varphi_i^{n+1}}{\varphi_i^{n+1}(1 - \varphi_i^{n+1})} \right) \frac{\varphi_{i+1}^{n+1} - \varphi_{i-1}^{n+1}}{2\Delta r_i} + \left( \frac{\rho_f - \rho_s}{(1 - c_i^{n+1})\rho_f + c_i^{n+1}\rho_s} \right) \frac{c_{i+1}^{n+1} - c_{i-1}^{n+1}}{2\Delta r_i} \right] \quad (C. 62)$$

Node  $i = Nr, j = Nr - 1$

$$\frac{\partial R_{Nr}^{3n}}{\partial p_{Nr-1}} = \frac{1}{\Delta r_{Nr}^2} + \frac{1}{2\Delta r_{Nr}} \left[ \frac{1}{r_{Nr}} + \left( \frac{3 - \varphi_{Nr}^{n+1}}{\varphi_{Nr}^{n+1}(1 - \varphi_{Nr}^{n+1})} \right) \frac{\varphi_e - \varphi_{Nr-1}^{n+1}}{2\Delta r_{Nr}} + \left( \frac{\rho_f - \rho_s}{(1 - c_{Nr}^{n+1})\rho_f + c_{Nr}^{n+1}\rho_s} \right) \frac{c_e - c_{Nr-1}^{n+1}}{2\Delta r_{Nr}} \right] \quad (C. 63)$$

Node  $i = Nr, j = Nr$

$$\frac{\partial R_{Nr}^{3^n}}{\partial p_{Nr}} = \frac{-2}{\Delta r_{Nr}^2} \tag{C. 64}$$

# Appendix D

## Geomechanical Boundary Conditions

Using the boundary Eqs. 4.2.14 and 4.2.15:

$$\left. \frac{\partial u}{\partial r} \right|_{r=r_w} = -\frac{v}{1-v} \frac{u(r_w)}{r_w} - g_3(r_w, t) [\varphi(r_w, t) p_{wf} - p_{wf}] \quad (\text{D. 1})$$

$$\left. \frac{\partial u}{\partial r} \right|_{r=r_e} = -\frac{v}{1-v} \frac{u(r_e)}{r_e} + g_3(r_e, t) [\varphi(r_e, t) p_e - \sigma_e] \quad (\text{D. 2})$$

If they are spatially (centered) and temporally D.0.1 discretized:

$$\frac{u_2^{k+1} - u_0^{k+1}}{2\Delta r_1} = \frac{v}{1-v} \frac{u_1^{k+1}}{r_1} - g_{3r_w} [\varphi_1 p_1 - p_1] \quad (\text{D. 3})$$

Solving for  $u_0^{n+1}$  from equation D.0.3:

$$u_0^{n+1} = u_2^{n+1} + 2\Delta r_1 \left( \frac{v}{1-v} \frac{u_1^{k+1}}{r_1} + g_{31} [\varphi_1 p_1 - p_1] \right) \quad (\text{D. 4})$$

Now, if it is spatially and temporally discretized D.0.2, the following is obtained:

$$\frac{u_{Nr+1}^{k+1} - u_{Nr-1}^{k+1}}{2\Delta r_{Nr}} = \frac{v}{1-v} \frac{u(r_{Nr})}{r_{Nr}} + g_3(r_{Nr}, t) [\varphi(r_{Nr}, t) p_{Nr} - \sigma_{Nr}] \quad (\text{D. 5})$$

Solving for  $u_{Nr}$  from equation D.0.5:

$$u_{Nr+1}^{k+1} = u_{Nr-1}^{k+1} + 2\Delta r_{Nr} \left( -\frac{v}{1-v} \frac{u(r_{Nr})}{r_{Nr}} + g_3(r_{Nr}, t) [\varphi(r_{Nr}, t) p_e - \sigma_e] \right) \quad (\text{D. 6})$$

# Appendix E

## Effective Well Stress Criterion Discretization

Once the displacement vector ( $u$ ) that the rock is experiencing is obtained, it is possible to determine the geomechanical behavior as the reservoir produces fluid and formation solids. The discretization of the geomechanical behavior is straightforward, as it only requires spatial discretization. Since a symmetric deformation analysis in an axial deformation plane is considered, Eqs. 3.7.1 and 3.7.2 are calculated and discretized:

For the nodes  $i = 2, \dots, Nr - 1$

$$\varepsilon_{ri} = \frac{u_{i+1} - u_{i-1}}{2\Delta r_i} \quad (\text{E. 1})$$

$$\varepsilon_{\theta i} = \frac{u_i}{r_i} \quad (\text{E. 2})$$

For the boundaries:

$i = 1$

$$\varepsilon_{ri} = -\frac{\nu}{1-\nu} \frac{u_1}{1} - g_{3rw}[\varphi_1 p_1 - p_1] \quad (\text{E. 3})$$

$$\varepsilon_{\theta 1} = \frac{u_1}{r_1} \quad (\text{E. 4})$$

$i = Nr$

$$\varepsilon_{rNr} = -\frac{\nu}{1-\nu} \frac{u(r_{Nr})}{r_{Nr}} + g_3(r_{Nr}, t)[\varphi(r_{Nr}, t)p_{Nr} - \sigma_{Nr}] \quad (\text{E. 5})$$

With the vectors from Eqs. E.0.1 - E.0.5, Eqs. E.0.6 and E.0.7 are determined, which in turn are discretized, yielding the following:

For the Nodes  $i = 1, \dots, Nr$

$$\sigma_{ri} = \frac{\bar{E}(1-\varphi_i)}{(1+\nu)(1-2\nu)} [(1-\nu)\varepsilon_{ri} + \nu\varepsilon_{\theta i}] \quad (\text{E. 6})$$

$$\sigma_{\theta i} = \frac{\bar{E}(1-\varphi_i)}{(1+\nu)(1-2\nu)} [(1-\nu)\varepsilon_{\theta i} + \nu\varepsilon_{ri}] \quad (\text{E. 7})$$

With Eqs. E.0.6 and E.0.7, it is possible to obtain the parameters  $\tau_m$  and  $\sigma_m$  to generate Figs. 4.14a and 4.14b.

# References

- Ahr, W. M. 2008. *Geology of Carbonate Reservoirs: The Identification, Description, and Characterization of Hydrocarbon Reservoirs in Carbonate Rocks*. Hoboken, New Jersey, USA: Wiley & Sons.
- AL-Aamri, M., Mahajan, S. M., Sujith, N. et al. 2020. Practical Approach for Solid Production Prediction and Completion Strategy Decisions in Horizontal Well - A Case study from Cretaceous Carbonate Reservoir - North Oman. Paper presented at the International Petroleum Technology Conference, Dhahran, Kingdom of Saudi Arabia, January 13-15. IPTC-20130-Abstract. <https://doi.org/10.2523/IPTC-20130-Abstract>
- Asadi, M. S., Khaksar, A., Nguyen, H. Q. et al. 2017. Solids Production Prediction and Management in a High Porosity Carbonate Reservoir - A Case Study from Offshore Vietnam. Paper presented at the SPE/IATMI Asia Pacific Oil & Gas Conference and Exhibition, Jakarta, Indonesia, October 17-19. SPE-186273-MS. <https://doi.org/10.2118/186273-MS>
- Chilingarian, G. V., Mazzullo, S. J., Rieke, H. H. et al. 1992. *Carbonate Reservoir Characterization: A Geologic-Engineering Analysis, Part I*. Amsterdam, The Netherlands: Developments in Petroleum Science, Elsevier.
- Fjaer, R. H., Holt, R. M., Horsrud, P. et al. 2008. *Petroleum Related Rock Mechanics*, second edition. Amsterdam, The Netherlands: Developments in Petroleum Science, Elsevier.
- Garaicochea P., F., and Samiego V., F. 1988. *Temas Selectos sobre la Caracterización y Explotación de Yacimientos Carbonatados*. Mexico, D. F.: Colegio de Ingenieros Petroleros de México.
- Jaeger, J. C., Cook, N. G. W., and Zimmerman, R. W. 2007. *Fundamentals of Rock Mechanics*, fourth edition. Malden, Massachusetts, USA: Blackwell Publishing.
- Lucia, F. J. 2007. *Carbonate Reservoir Characterization: An Integrated Approach*, second edition. Berlin, Germany: Springer.
- Ng, K., and Santamarina, J. C. 2023. Mechanical and Hydraulic Properties of Carbonate Rock: The Critical Role of Porosity. *Journal of Rock Mechanics and Geotechnical Engineering* **15** (4): 814-825. <https://doi.org/10.1016/j.irmge.2022.07.017>
- Plumb, R. A. 1994. Influence of Composition and Texture on the Failure Properties of Clastic Rocks. Paper presented at the Rock Mechanics in Petroleum Engineering, Delft, The Netherlands, August 29-31. SPE-28022-MS. <https://doi.org/10.2118/28022-MS>

- Saadatnia, N., Sharghi, Y., Moghadasi, J. et al. 2023. Coupled Hydro-Mechanical Simulation in the Carbonate Reservoir of a Giant Field in Southwest Iran. *Journal of Petroleum Exploration and Production Technology* **14** (1): 59-83. <https://doi.org/10.1007/s13202-023-01695-2>
- Stavropoulou, M., Papanastasiou, P., and Vardoulakis, I. 1998. Coupled Wellbore Erosion and Stability Analysis. *International Journal for Numerical and Analytical Methods in Geomechanics* **22** (9): 749-769. [https://doi.org/10.1002/\(SICI\)1096-9853\(199809\)22:9<749::AID-NAG944>3.0.CO;2-K](https://doi.org/10.1002/(SICI)1096-9853(199809)22:9<749::AID-NAG944>3.0.CO;2-K)
- Téllez Arellano, A. G. 2021. *Modelo de Flujo-Geomecánico para la Predicción del Colapso de la Formación*. BS, Universidad Nacional Autónoma de México, Facultad de Ingeniería, Ciudad Universitaria, CdMx.
- Vardoulakis, I., Stavropoulou, M., and Papanastasiou, P. 1996. Hydro-Mechanical Aspects of the Sand Production Problem. *Transport in Porous Media* **22** (2): 225-244. <https://doi.org/10.1007/BF01143517>
- Zhou, B., Dong, C., Huang, F. et al. 2024. Experimental Study and Prediction Method of Solid Destabilization and Production in Deep Carbonate Reservoir During Mining. *Journal of Rock Mechanics and Geotechnical Engineering* **17** (2): 1085-1101. <https://doi.org/10.1016/j.jrmge.2024.05.023>
- Zoback, M. D. 2007. *Reservoir Geomechanics*. Cambridge, United Kingdom: Cambridge University Press.